Title

Two-Color Ionization Injection

ISBN

9798276019598

Author

Fan-Chiang, Liona

Publication Date

2025-12-06

Peer reviewed|Thesis/dissertation

Two-Color Ionization Injection

By

Liona Fan-Chiang

A dissertation submitted in partial satisfaction of the

requirements for the degree of

Doctor of Philosophy

in

Applied Science and Technology

in the

Graduate Division

of the

University of California, Berkeley

Committee in charge:

Professor Karl van Bibber, Co-Chair
Adjunct Professor Carl Schroeder, Co-Chair
Professor Jonathan Wurtele
Professor David Attwood

Fall 2025

Two-Color Ionization Injection

Abstract

Two-Color Ionization Injection

by

Liona Fan-Chiang

Doctor of Philosophy in Applied Science and Technology

University of California, Berkeley

Professor Karl van Bibber, Co-Chair

Adjunct Professor Carl Schroeder, Co-Chair

This thesis presents progress on a demonstration experiment of two-color ionization injection (TCII) in laser driven plasma accelerators (LPAs). The method has been theorized to potentially produce ultra-low, tens of nm rad, emittance beams, but has yet to be demonstrated in the laboratory. Were LPAs to reliably produce ultra-low emittance beams, they would become compact sources for a number of applications that require high brightness beams enabled by low emittance.

Circularly polarized drive pulses were used for the first time to turn off ionization injection and prepare a dark-current-free wake for further injection. A regime was found in which wakes generated by circularly polarized pulses were proven to be of equivalent amplitude as those generated by linearly polarized pulses, but unlike the linearly polarized case, ionized electrons were not injected into the trapped region of the wake.

High intensity, broadband, ultrashort third harmonic pulses were generated for ionization injection of electrons into a preformed wakefield accelerator for the first time. A low ponderomotive potential but high electric field injector was formed by harmonic conversion of 800 nm fundamental wavelength to 267 nm. Harmonic conversion efficiency as a function of intensity, bandwidth, and crystal thicknesses were measured. A UV pulse diagnostic was built to resolve pulse length and higher order nonlinearities.

Planar laser-induced fluorescence (PLIF) was used to customize LPA targets for the first time. PLIF, combined with fluid simulations, were used to iteratively design gas density profiles for desired features. Manufactured nozzles were subsequently qualified via PLIF.

Finally, methods of spatial and temporal coupling of the third harmonic injector into the preformed wake are presented and show achievement of femtosecond and micrometer precision required for controlled injection of low emittance beams.

Dedication

This thesis is dedicated to all those at BELLA Center, past and present, who took me in, trained and nurtured me as a scientist, and provided an inclusive environment that was fun, supportive, collaborative, truthful, curious, fast and rigorous. To my committee members who have guided me throughout my graduate education. To David Attwood who was the first to shrug off grades and ask me what I wanted in life. To my family who have loved me without questioning what weird things I do with my life. To Shawn Difranco who taught me life skills and patiently supported me in my studies. To Mervin Fansler who has been my academic, philosophical and emotional beacon for the long haul. Thank you.

Contents

List of Figures

List of Tables

Acknowledgments

This work was supported by the U.S. Department of Energy (DOE), Office of Science, Offices of High Energy Physics, under Contract No. DE-AC02-05CH11231and by the National Science Foundation (NSF) under grant DGE 1752814.

This research used the open-source particle-in-cell code WarpX `https://github.com/BLAST-WarpX/warpx`. Primary WarpX contributors are with LBNL, LLNL, CEA-LIDYL, SLAC, DESY, CERN, Helion Energy, and TAE Technologies. We acknowledge all WarpX contributors.

Chapter 1

Introduction

Laser driven plasma accelerators (LPAs) are compact sources of accelerated electrons and ions, and therefore sources of muons, x-rays and gamma rays [1, 2, 3, 4, 5, 6, 7, 8]. Successful demonstration of the ability of LPAs to reliably deliver accelerated particles, and associated light, has attracted users and collaborators from basic science, industry, healthcare, and defense [9, 10, 11, 12, 13, 14, 15, 16, 17]. Expect users and use cases to burgeon as these particle and light sources become cheaper and locally accessible.

Historically, accelerated particles and their derivatives are produced by radio frequency (RF) driven accelerators with kilometer scale footprints built of metal and concrete. Lower limits on footprint are determined by upper limits in electric field gradients that can be sustained by any metallic structure before the structure begins to be torn apart electrically. Advantages of plasma based accelerators begin at this limit. Starting with a plasma, which by definition is an electrically broken down substance, a laser or electron bunch drives resonant plasma structures that can sustain $\sim$100 GV/m electric field gradients, three orders of magnitude greater than that capable by metallic accelerators, and can therefore be used to accelerate charged particles to GeV energies in the meter scale. Currently, research-grade laser driven wakefield accelerators, including the laser that is the bulk of the facility, occupy the space of a large classroom.

In addition, since laser driven wakefield accelerators use short pulse lasers, $\sim$100 femtoseconds (fs), the accelerated electron bunches they produce are equally short. Moreover, the availability of short pulse lasers and inherently synchronized particle beams in LPA target chambers make them unique environments for science. Applications such as time resolved chemical reactions [18, 11], cell development [15], and pump probe shock formation and imaging [17], make the field of plasma based wakefield accelerated particles an important asset to the national and international science portfolio.

Following the demonstration of percent level energy spread beams produced from LPAs [19, 20, 21] great interest was shown in using LPAs as compact electron beam sources for driving valuable x-ray free electron lasers (XFELs) to produce X-rays in intense, coherent, femtosecond bursts that enable the dynamics of chemical reactions, materials and biomolecular systems to be studied with unprecedented spatial and temporal resolution [22, 23, 24].

The world's first XFEL, the Linac Coherence Light Source (LCLS) came on line in 2009, driven by a radio frequency (RF) accelerator at SLAC [25, 26]. LCLS is the only such device in the United States and to date only six exist in the world [27]. Use of these valuable tools is expensive and oversubscribed. Availability of cheap, compact XFELs would immediately engage accumulating demand.

Since the conception of a "collective accelerator" in 1979 [1] LPAs have demonstrated production of beams with an impressive range of parameters: from 1 pico-coulomb (pC) to a few nano-coulombs (nC) in charge [28], from 1 mega-electron-volt (MeV) to 10 giga-electron-volts (GeV) class in maximum energy [29, 30], 100% to sub-1% in energy spread [31], and 100 μm rad to a few hundred nm rad in normalized emittance [32]. A large portion of research today aims to gain full control over this parameter space to make on-demand beams per user requirements.

A significant breakthrough came in the past five years, during which several facilities have demonstrated gain from free electron lasers (FELs) driven by electrons beams which were accelerated by laser-driven wakefield accelerators [33, 34, 16]. Importantly, this year, 1000-fold gain was generated with hours of stable operation [16]. Among these, the lowest wavelength generated was 27 nm [33]. In order for LPAs to contribute to XFELs (0.01 nm - 10 nm) they must increase beam brightness,

$$B_{6D} = I_b/\sigma_E \epsilon_x \epsilon_y \ .$$

Here I_b is the beam current, σ_E is the energy spread, and ϵ_x and ϵ_y are the transverse emittances. LPAs naturally produce short, high peak current beams that have the potential to be of high brightness. A major challenge to LPA research is to produce sub-0.1% level energy spread and tens of nm emittance. Both require triggered beam injection methods.

An estimate for the required emittance for an FEL is given by the Pelligrini coherence criterion

$$\epsilon_n < \gamma \lambda_r / 4\pi \ ,$$

which guarantees that radiation from individual electrons overlap and add coherently to create the lasing mode [35]. Here ϵ_n is the normalized emittance, λ_r is the center radiation wavelength, and γ is the relativistic Lorentz factor $\gamma = (1 - v^2/c^2)^{-1/2}$. For example, for a 1.5 GeV beam to create $\lambda_r = 10$ nm radiation, $\epsilon_n < 230$ nm.

The subject of this thesis is progress on a method to produce hundreds to tens of nanometer emittance beams from a LPA called two-color ionization injection (TCII). TCII [36, 37, 38] proposes to isolate electron beam formation from wakefield generation by employing a second trailing pulse. The method leverages the wavelength dependence of the ponderomotive potential to shape a trailing pulse that can ionize with high intensity, yet inject with low transverse momentum. Simulations have shown the possibility of producing beams with tens of nm normalized emittance [38].

The remainder of this chapter summarizes concepts of laser-driven wakefield accelerators that are relevant to the understanding of the body of this work. The method by which electrons are introduced into the accelerator, injection, will be the subject of Chapter 2.

The theoretical foundation of two-color ionization injection, including trapping conditions and contributions to emittance, sets the requirements for driver and injector laser properties that lead to the production of low emittance beams, and will provide guidance for a proof-of-principle experiment. Experimental and simulation results from preparations for a proof of principal experiment on a 100 TW Ti:sapphire laser system span Chapters 3-6. Chapter 3 begins with the design and testing of a circularly polarized driver to prepare a high amplitude wake for further ionization injection. Results show that using a circularly polarized drive is an effective and straightforward way to turn off ionization injection during wake formation, providing a dark-current-free accelerator, while still driving a large amplitude wake. The crux of the two-color ionization injection method that gives injected electrons low transverse emittance is the use of a high frequency injector pulse. For the demonstration experiment, preparation of the injector laser involved generating a high intensity ultraviolet laser which is synchronized to the drive. This was accomplished by converting one of two beamlines into its third harmonic. Development, component testing and high power harmonic generation results are presented in Chapter 4. Aside from the lasers, the only other variable that allows control of the laser-plasma interaction is the plasma source, which usually derives from neutral gas. For this reason, much consideration was given in specifying and characterizing the neutral gas plumes. Results of simulations and measurements of the gas target used for this study will be presented in Chapter 5. Methods for focusing and coupling the injector laser into the preformed wake are covered in Chapter 6, including requirements on diagnostics. A summary and outlook concludes the thesis.

1.1 Laser Wakefield Acceleration

The transient nature of plasma accelerators, which allows them to support high field gradients, also makes them challenging to control and reproduce. Permanent metallic structures are replaced by plasma structures that are recreated at each shot and exist for only a few picoseconds at a time. The accelerator is formed by a nonlinear interaction of a high power laser pulse, itself a cascade of nonlinear processes often pushed to their limits, with a plasma. The plasma responds with oscillatory motion, creating density variation along with its own fields. Density variation in turn, influences laser propagation, in all forming a self-evolving laser-plasma interaction. The plasma wave, created by the laser, follows in the wake of the laser near the speed of light, while sustaining large field gradients. Electrons that land inside of this wave can become trapped and ride this accelerator. Under certain conditions, while riding this accelerator, the trapped beam must also contend with the laser that is intense and evolving. In addition, without taking into account the potentially violent method of coaxing electrons into a trapped phase, the existence of the trapped electrons impacts the fields of the accelerator, that in turn impacts acceleration of the beams.

Laser driven wakefield accelerators use ultra-short, focused laser pulses to drive waves in plasmas. Were the laser to be large, continuous and collimated, delivering a plane wave, charged particles would respond with oscillatory motion along the polarization direction of the laser at the laser frequency, but would result in zero average motion. Under the influence of a finite pulse, however, charges do not experience the same field during an oscillatory period, and therefore their cycle-averaged displacement is non-zero. The result is that charges are ponderomotively expelled from regions of higher intensity to regions of lower. The ponderomotive force can be expressed as

$$F_{pond} = -\frac{e^2}{4m_e\omega^2}\nabla E_s^2(r) \ ,$$

where e and m_e are the electron charge and mass, and $E_s(r)$ is a slowly varying envelope of the laser electric field E_L. The ponderomotive force is in the direction of decreasing gradient of the electric field envelope. It is useful to state the ponderomotive force in terms of the transverse momentum imparted on the particle by the electromagnetic field

$$F_{pond} = -\frac{mc^2}{2}\nabla a_0^2(r) \ ,$$

where a_0 is the amplitude of the normalized vector potential $a = eA/mc$. In the broad pulse limit, $w_0 \ll \lambda_0$, where w_0 is the focal spot size and λ_0 is the laser vacuum wavelength, the conservation of canonical momentum gives

$$\frac{p_\perp}{mc} = \frac{eA}{mc} \to a = \frac{\gamma_\perp v_\perp}{c} \ ,$$

where $\gamma_\perp$ is the transverse Lorentz factor. It is clearer to see from this that a is the normalized transverse momentum imparted on the particle by the laser field. In addition $a \geq 1$ gives the domain in which relativistic effects must be taken into account.

In terms of the intensity and laser wavelength, $I = \frac{1}{2}\epsilon_0 c E_L^2$ and $\lambda_L = 2\pi c/\omega_L$,

$$a_0 \approx 0.85\lambda_L[\mu\text{m}]\sqrt{I[10^{18}\text{W/cm}^2]} \ .$$

At short time scales, ~100 femtoseconds (fs), electrons, nearly 2000 times lighter than protons, dominate dynamics. After being displaced by the electric field of a laser pulse, the electrons, drawn by the restoring force from the ions they left behind, begin simple harmonic motion about their initial position with characteristic electron oscillation frequency that is only a function of the charge density n_e

$$\omega_p = \sqrt{\frac{e^2 n_e}{\epsilon_0 m_e}} \ ,$$

where ω_p is the electron plasma frequency, n_e is the electron number density, and ϵ_0 is the vacuum permittivity. The corresponding electron plasma wavelength, $\lambda_p = 2\pi v_p/\omega_p$, as plasma wave phase velocity approaches the speed of light, $v_p \to c$, is

$$\lambda_p[\mu\text{m}] = \frac{3.33 \times 10^{10}}{\sqrt{n_0[\text{cm}^{-3}]}} \ .$$

At a charge density of $n_e = 3 \times 10^{18}$ cm^{-3}, $\lambda_p = 19$ μm. The wave is driven most efficiently for a laser with a pulse length $\tau_L \approx c\lambda_p/2$, which corresponds to a pulse length of $\tau_L = 33$ fs for $n_e = 3 \times 10^{18}$ cm^{-3}. The above plasma frequency can be derived from the cold fluid equations that assume that thermal motion of both ions and electrons is small compared to the fluid motion, and that ions are stationary, $v_i = 0$. This is a valid approximation for LPAs which operate at a temperature of order $T_{eV} = 10$ eV, corresponding to an electron thermal velocity that is much smaller than the electron velocity, $v_{th} = \sqrt{3T_{eV}/m_e} \ll v_e$. We assume that electrons are initially at rest and homogeneous such that density perturbation $\delta n_i = 0$. The result of the approximations is the set of continuity, momentum and Maxwell's equations:

$$\begin{aligned} &\text{Continuity} \quad && \frac{\partial n_e}{\partial t} + \nabla \cdot (n_e v_e) = 0 \\ &\text{Momentum} \quad && \frac{\partial p_e}{\partial t} + (v_e \cdot \nabla) p_e = -e(E + v_e \times B) \\ &\text{Poisson} \quad && \nabla \cdot E = \frac{e}{\epsilon_0}(n_i - n_e) \end{aligned}$$

Under this set of assumptions, analytic solutions exist, and many intuitive relations can be easily gathered from them. From these equations, a first order approximation of the maximum electric field that the wave can sustain, can be obtained. Taking the case where the electrons begin to catch up with the wake phase velocity, $v_p \to c$, and the density perturbation becomes comparable to the plasma density, and assuming an oscillatory solution of the form $\delta n = \delta n_0 \sin(k_p z - \omega_p t)$, the non-relativistic wavebreaking field is

$$E_0[\text{V/m}] \longrightarrow \frac{m_e \omega_p c}{e} = \frac{m_e c}{e}\sqrt{\frac{e^2 n_0}{\epsilon_0 m_e}} = 96\sqrt{n_0[\text{cm}^{-3}]} \; .$$

For electron densities $n_e \approx 10^{18}$ cm^{-3}, $E \approx 100$ GV/m. Conceptually if the wake electrons begin to outrun the wake, the wave begins to crash like waves near the beach. In reality as the plasma velocity approaches the speed of light, they become relativistic and the limit for maximum electric field becomes [2]

$$E_{WB} = \sqrt{2(\gamma_p - 1)} E_0$$

where $\gamma_p = (1 - \beta_p^2)^{-1/2}$, $\beta_p = v_p/c$.

Once the plasma wave exists, the density variation impacts the way the laser propagates through it. Under the same cold fluid approximations, light travels in a plasma according to

$$\text{Momentum} \quad \frac{\partial p_e}{\partial t} + (v_e \cdot \nabla) p_e = -e(E + v_e \times B)$$

$$\text{Maxwell} \quad \nabla \times B = -\mu_0 e n_e v_e + \frac{1}{c^2} \partial_t E$$

$$\nabla \times E = -\partial_t B$$

To first order, these equations give the dispersion relation

$$\omega_0^2 = \omega_p^2/\gamma + c^2 k^2$$

From the dispersion relation, the phase velocity and group velocity of the laser propagating in the plasma can be derived. The phase velocity is

$$v_\phi = \frac{\omega_0}{k} = \frac{\sqrt{\omega_p^2/\gamma + c^2 k^2}}{k} \ ,$$

and the group velocity,

$$v_g = \frac{d\omega_0}{dk} = \frac{c^2 k}{\sqrt{\omega_p^2/\gamma + c^2 k^2}}$$

In a plasma the phase velocity of light is super-luminal. For light, $v_g v_\phi = c^2$, thus $\eta = c/v_\phi = v_g/c$ and $v_g = \eta c = v_{\phi p}$ where v_g is the group velocity of the laser pulse, and η is the index of refraction, which is given by

$$\eta = \frac{c}{v_\phi} = \frac{ck}{\sqrt{\omega_p^2/\gamma + c^2 k^2}} = \frac{v_g}{c} = \sqrt{1 - \frac{\omega_p^2/\gamma}{\omega_0^2}} \ .$$

From here it can be seen that for $\omega_0^2 < \omega_p^2/\gamma$ the index of refraction is imaginary, setting an upper bound to the charge density that is transparent to light at a particular wavelength. The critical density, or cut-off density, as $\omega_p \rightarrow \frac{2\pi c}{\lambda_0}$ is given by

$$n_c[cm^{-3}] = \frac{1.1 \times 10^{21}}{\lambda_0[\mu\text{m}]} \ ,$$

assuming a nonrelativistic plasma $\gamma \simeq 1$. The critical density is $n_c = 1.74 \times 10^{21}$ cm^{-3} for $\lambda = 800$ nm light. When $n_e < n_c$ the plasma is termed underdense. Electrons cannot respond fast enough to the light and the plasma is transparent. When overdense $\omega_p > \omega_0$ the characteristic time scale of the electron is fast enough to adapt to the incoming wave and to reflect the radiation.

For a Gaussian shaped focus with intensity profile,

$$I = I_0 \exp(2r^2/w_0^2) \ ,$$

the size of the beam varies with distance from focus

$$w(z) = w_0\sqrt{1 + z^2/z_r^2} \ ,$$

where $z_R = \pi w_0^2/\lambda$ is the Rayleigh range over which intensity stays within a factor of 2 of that of focus.

As a function of radius

$$\eta = \sqrt{1 - \frac{\omega_p^2}{\omega_0^2}\frac{n(r)}{\gamma(r)n_0}} \ .$$

Non-uniform transverse densities or intensity profiles will focus or defocus the laser pulse by bending the phase fronts due to the difference in phase velocity as a function of radius. The relativistic Lorentz factor that appears in the index of refraction is due to the fact that ω_p is mass dependent. As the electrons oscillate, their velocities on-axis are greater than that off-axis. As a result, as motion becomes relativistic, lensing can counteract laser diffraction and cause relativistic self-focusing [39, 40]. This occurs near a critical laser power

$$P_{crit}[GW] \approx 17\left(\frac{\omega_0}{\omega_p}\right)^2 \ .$$

The critical power is density dependent so that at higher densities, self-focusing occurs at lower laser power.

The plasma oscillation is a charge density wave with periodic regions of more and less negative charge and a nearly immobile positive background restoring force. Therefore, it is a source of large longitudinal and radial electric fields. The longitudinal fields accelerate and decelerate charged particles within the wakefield. Fig. 1.1 shows plots of the normalized laser intensity a^2 of a Gaussian shaped drive pulse, the resulting normalized longitudinal electric field produced by the wake E_z/E_0, and the corresponding normalized electric potential $\phi = e\Phi/mc^2$.

In one dimension, using a linearly polarized Gaussian shaped drive pulse of optimal pulse duration, the longitudinal electric field generated by the wake is

$$E_z(z,t) = \sqrt{\frac{\pi}{2e}}\frac{a_0^2/2}{\sqrt{1+a_0^2/2}}E_0\cos\left(k_p\zeta\right) \ ,$$

where $\zeta = z - ct$.

In two dimensions, using an intensity profile of the form

$$I(z,r,t) = I_0 e^{-2r^2/w_0^2} e^{(t-z/c)^2/\tau_L^2} \ ,$$

the radial wake can be derived

$$E = -\nabla\Phi \rightarrow \frac{\partial E_z}{\partial r} = \frac{\partial^2\Phi}{\partial z\partial r} = \frac{\partial E_r}{\partial z} \ ,$$

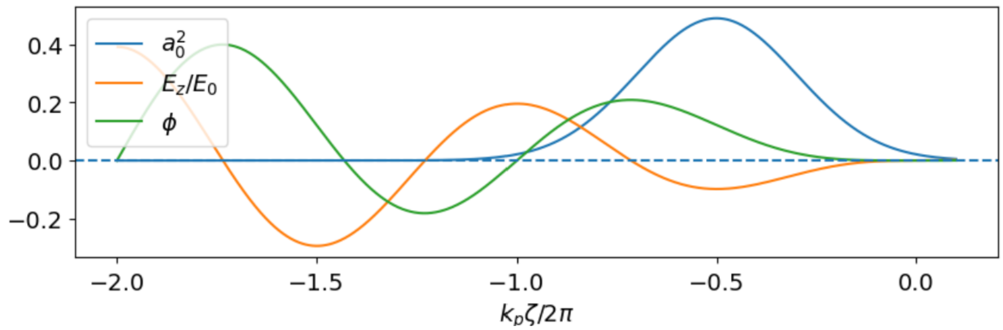

Figure 1.1: Normalized laser intensity a^2, normalized electric potential of the wake $\phi = e\Phi/mc^2$, and normalized accelerating field of the plasma wave E_z/E_0 for the case of $a_0 = 0.7$, using a Gaussian shaped laser pulse with pulse length $\tau_L = \lambda_p/2$, with background plasma density $n_e = 4 \times 10^{18}$ cm^{-3}.

so that for

$$E_z \propto -\exp\left(\frac{-2r^2}{r_s^2}\right)\cos\left(k_p\zeta\right) \ ,$$

the radial electric field is

$$E_r \propto \frac{4r}{k_p r_s^2}\exp\left(\frac{-2r^2}{r_s^2}\right)\sin\left(k_p\zeta\right) \ .$$

The longitudinal and radial electric fields of the plasma wave are out of phase, and, therefore, only a $\lambda_p/4$ region within each period is both longitudinally accelerating, $E_z < 0$, and radially focusing, $E_r > 0$, $-2\pi < k_p\zeta < -3\pi/2$ for the example above. The force due to radial electric field on a trapped electron is zero on-axis and increases with electron position off-axis. This radial force causes electrons injected off-axis to oscillate about the axis contributing to residual transverse momentum of accelerated beams.

The distance over which electrons can accelerate, and therefore the final electron energy, is determined by the characteristic scale lengths of the laser-plasma interaction unless mitigated. A focused laser pulse will diffract, and near focus the focal intensity is maintained for approximately $2z_R$ for a Gaussian pulse profile pulse. For example, for a $w_0 = 20$ μm focus of a $\lambda = 800$ nm wavelength laser, $2z_R = 3.2$ mm. This length can be extended by taking advantage of self-focusing but the front of the pulse will still diffract as it ionizes to form the plasma. Diffraction of the front of the pulse can be mitigated by the use of preformed plasma channels [41, 42].

Another limit to acceleration length is the fact that accelerated electrons can outrun the wake. As the electron accelerates, it begins to progress in its position relative to the wake that is traveling near the group velocity of the laser and has an accelerating region on the scale of $\lambda_p/2$. Eventually the accelerated particle will reach a decelerating phase. This is referred to as dephasing. For a particle traveling at $\sim c$, the length of time for the particle to traverse the accelerating region is $t_{\lambda_p/2} = (\lambda_p/2)/(c - v_g)$, so that the length that the beam travels before dephasing is $L_{\lambda_p/2} = ct_{\lambda_p/2}$. Using

$$v_g = \frac{d\omega}{dk} = c\sqrt{1 - \frac{\omega_p^2}{\omega^2}} \ ,$$

and

$$\gamma_g = \left(1 - \frac{v_g^2}{c^2}\right)^{-1/2} = \frac{\omega}{\omega_p} \ ,$$

then

$$L_{\lambda_p/2} = \frac{\lambda_p^3}{\lambda^2} \ .$$

In terms of density and wavelength,

$$L_{\lambda_p/2}[cm] = \lambda_p^3/\lambda^2 \approx \frac{3.7}{n_0[10^{18}cm^{-3}]^{3/2}\lambda[\mu m]^2} \ .$$

Lowering density is desirable for increasing acceleration length and particle beam energy. When $a_0 \gg 1$ [43],

$$L_{\lambda_p/2} \approx a_0 \frac{\lambda_p^3}{\lambda^2} \ .$$

A gradual density up-ramp can in principle compensate dephasing as the plasma wavelength λ_p decreases, and keep the beam in an accelerating phase [44, 45, 46, 47].

Finally, if no other mechanism impedes, transfer of the laser energy to wake formation will eventually lead to insufficient laser intensity to sustain the laser-plasma interaction. Laser pump depletion sets the upper limit on acceleration length to [2, 43]

$$L_{dep} = \frac{\lambda_p^3}{\lambda^2} \times \begin{cases} 2/a_0^2 & \text{for } a_0^2 \ll 1 \\ (\sqrt{2}/\pi)a_0 & \text{for } a_0^2 \gg 1 \end{cases}$$

The mechanisms by which electron plasma waves are generated by a short pulse laser, as well as how that wave can affect the laser and electrons within the electric field of the wave, have been summarized here. However, electrons that participate in generating the longitudinal and radial fields discussed oscillate, experiencing accelerating and decelerating fields. In order to reach high energies, electrons must be injected and travel near synchronously with the phase velocity of the plasma wake. Not yet discussed is how electrons enter, are injected into, the wakefield to be accelerated. Mechanisms by which electrons are injected, as well as the theory behind two-color ionization injection are the subjects of Chapter 2.

Chapter 2

Two-Color Ionization Injection

Two separate populations of electrons must participate in laser driven wakefield acceleration. The majority have low energy and bob back and forth with the laser electric field but cumulatively form a wave, with large electric field gradients, whose phase velocity is the speed of light. Sometimes called background or wake electrons, these make up the accelerator and determine plasma properties such as n_e and thus v_p and ω_p. The second population are those that fall inside of this wave at proper wave phase, and surf its pummeling electric field to relativistic speeds.

When, where, and how many electrons appear in the wave greatly affects final beam properties - charge, energy, energy spread, emittance - of the final accelerated beam. For this reason, methods for precise control of injection wake phase, position, duration, extent, and initial and final momentum of injected electrons, continue to be pioneered.

The first experiments with laser driven wakefield acceleration pulled surfers directly from the background, self injecting, by use of laser intensities large enough to drive the wake to wave breaking [1, 48, 49, 50, 51]. Though highly nonlinear, evolving, difficult to control and reproduce, a resonant regime was found where quasi-monoenergetic beams were generated [19, 20, 21].

While rapid progress in controlling self-injection for desired beam properties continues, parallel research in other injection methods have been proposed and tested that hope to lower density and laser requirements, while improving control over injection space, time, momentum and wake phase.

In order for electrons to surf the electric field of the wake, wake electrons must gain a velocity greater than that of a wake that is traveling near the speed of light, and end up in the accelerating portion within its wake field. To aid this process, the wake can be momentarily slowed down. Tailored plasma density profiles have been used to locally slow the wake phase velocity, relaxing trapping conditions, thereby capturing wake electrons in its accelerating phase to be accelerated [52, 53, 54, 55, 56, 57]. The lowest measured LPA generated beam emittance, 0.2 π mm mrad [32], was achieved using density downramp injection.

Rather than slowing the wake, wake electrons can be selectively sped up. For instance, electrons can be selectively accelerated or dephased [58] by another laser. An example is colliding pulse injection, in which a second laser, of the same wavelength, collides with the wake driver and generates a standing wave that locally heats background electrons. Experiments have produced electron beams with 1% energy spread using this method [59, 60, 61, 62, 63].

Alternately, instead of employing wake electrons, electrons can be created within the accelerating field of the wake. This can be done by aid of a target containing a high Z gas, where the two populations are formed by the low and high ionization threshold electrons of the atom. This method, called ionization injection, first generates the wake from electrons with lower ionization threshold. Then, with either the more intense portion of the laser pulse, or with a separate pulse, ionizes higher ionization threshold electrons locally in the proper phase of the wake to be accelerated [58, 64, 65, 66, 67, 68, 69, 70, 71].

In this chapter, the theoretical foundations of an ionization injection technique, called two-color ionization injection, which could produce ultra-low emittance electron beams [36, 37, 38] will be summarized. This method uses a separate collinear trailing laser pulse, at a shorter wavelength than that which created the wake, to controllably ionize and inject electrons into the preformed wake. The method allows independent optimization of wake creation and injection. The first beam is used to drive a wake with high amplitude. Another follows that ionizes and injects electrons nearly at rest, with low transverse momentum, in the optimal phase of the wake. Minimum trapping conditions, which set necessary properties of the wake driver, and factors that contribute to emittance, which determine properties of the injector laser, will be outlined.

2.1 Trapping Conditions for Ionization Injection

Wake driver parameters are set by minimum requirements for the ability to generate a plasma wave sustaining fields that trap and accelerate. In a one dimensional cold fluid model, under the assumption that the wake driver is non-evolving, trapping can be described by the Hamiltonian [72, 2]

$$H(u,\psi) = \gamma - \gamma\beta\beta_p - \phi(\psi) = (\gamma_\perp^2 + u^2)^{1/2} - \beta_p u - \phi(\psi)\ ,$$

where $\gamma = \sqrt{\gamma_\perp^2 + u^2}$ is the Lorentz factor of a test electron, β is the longitudinal particle velocity normalized to c, $u = \gamma\beta$ is the normalized longitudinal momentum, β_p is the normalized phase velocity of the wave, and is $\beta_p \approx 1 - \omega_p^2/2\omega_0^2$ when $\omega_p^2 >> \omega_0^2$, $\phi = e\Phi/m_e c^2$ is the electrostatic potential of the plasma wave normalized to the electron rest energy, and $\psi = k_p\xi = k_p(x - \beta_p t)$ is the plasma wave phase. $\gamma_\perp = \sqrt{1+u_\perp^2}$ is the transverse Lorentz factor where $u_\perp$ is the normalized transverse electron momentum.

Here, it is assumed that the ions are stationary, valid for interaction times much less than that for ion motion, i.e. $\tau_L \ll 1/\omega_{pi}$, where τ_L is the pulse length of the laser, and ω_{pi} is the plasma frequency of ions, which are more massive than the electrons, such that $\omega_{pe}^2/\omega_{pi}^2 = M_i/m_e \gg 1$. It is also assumed that the quiver velocity of electrons is much greater than the thermal velocity $v_\perp \simeq eE_L/m_e\omega_L \gg v_{th} = \sqrt{k_B T/m_e}$.

Solving for u, normalized particle longitudinal momentum as a function of the Hamiltonian, which is a constant of motion along an electron orbit, is

$$u = \beta_p \gamma_p^2 (H_0 + \phi) \pm \gamma_p \sqrt{\gamma_p^2 (H_0 + \phi)^2 - \gamma_\perp^2} \ ,$$

where H_0 is the initial energy of the particle.

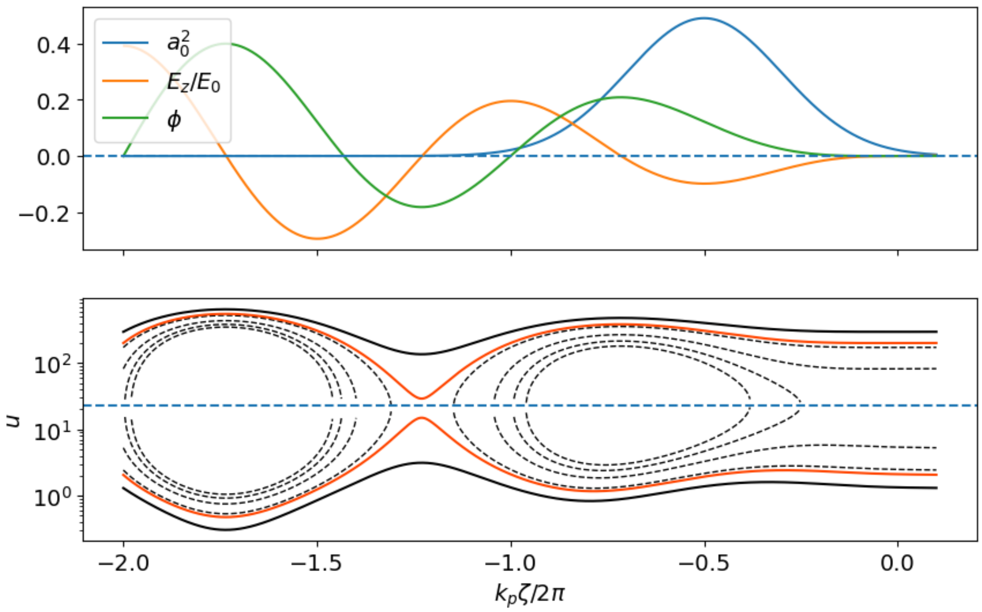

Figure 2.1: a^2, ϕ and E_z/E_0 for the case of $a_0 = 0.7$, and pulse length $\tau_L = \lambda_p/2$, with background plasma density $n_e = 4 \times 10^{18}$ cm^{-3} (top), the corresponding phase phase space with several values of H_0 (bottom). Trapped orbits are in dashed lines and untrapped orbits in solid black. The dashed blue line is the fluid velocity $u = \beta_p \gamma_p$ and the red line is the separatrix trajectory corresponding to H_s.

The particle is trapped if it orbits, i.e., if u has an imaginary component and thus describes oscillatory motion, giving the condition $\gamma_\perp \geq \gamma_p(H + \phi)$. The minimum value $\gamma_\perp(\psi_{min}) = \gamma_p(H_s + \phi(\psi_{min}))$ gives the separatrix Hamiltonian, which separates trapped and untrapped orbits. The separatrix Hamiltonian,

$$H_s = \gamma_\perp(\psi_{min})/\gamma_p - \phi_{min} \ ,$$

is where the electron has the same velocity as the plasma wave $H(\gamma_s, \psi) = H(\gamma_p, \psi_{min})$. Here, ψ_{min} is where $\phi(\psi_{min}) = \phi_{min}$. In Fig 2.1, u is plotted for several values of H using a linearly polarized Gaussian pulse with $a_0 = 0.7$, pulse length $\tau_L = \lambda_p/2$, and background plasma density $n_e = 4 \times 10^{18}$ cm^{-3}. When $H < H_s$, the particles traverse trapped orbits (dotted lines), whereas when $H > H_s$ particles slip past the wake and participate in fluid motion. The orbit that separates trapped and untrapped trajectories is shown in red, corresponding to H_s. The corresponding a^2, ϕ and E_z/E_0 for the same case is shown above the phase space diagram.

The Hamiltonian of an electron ionized at rest is [71]

$$H_i = \gamma_\perp - \phi(\psi_i) = 1 - \phi(\psi_i) \ ,$$

where ψ_i is the wake phase at which the injected electron is ionized.

The electron is trapped if $H_i < H_s$, or

$$1 - \phi(\psi_i) \leq \gamma_\perp(\psi_{min})/\gamma_p - \phi_{min} \ .$$

In one dimension, or for a broad pulse, where the spot size is much larger than the wavelength, $w_0 \gg \lambda_0$, the conservation of canonical momentum states

$$\delta(u_\perp - a_\perp) = 0 \ ,$$

where $a_\perp = eA/mc^2$ is the normalized vector potential. This relation is exact in 1D. Thus, for an electron ionized at rest, $u_\perp(\psi_i) = 0$, at wake phase ψ_i, $u_\perp(\psi) = a_\perp(\psi) - a_\perp(\psi_i)$.

Once the electron leaves the laser field, $a_\perp(\psi) = 0$, $\gamma_\perp = \sqrt{1 + u_\perp} = \sqrt{1 + a_\perp(\psi_i)}$, and the trapping condition relating the minimum potential of the wake phase to the phase where the initial ionization occurs within the wake is given by

$$1 + \phi(\psi_{min}) - \phi(\psi_i) \leq \sqrt{1 + a_\perp^2(\psi_i)}/\gamma_p \ ,$$

which includes the residual transverse momentum, $\gamma_\perp = \sqrt{1 + a_\perp^2(\psi_i)}$, imparted on the electron born inside of the injection laser pulse.

The resulting wakefield can be obtained by solving the nonlinear plasma wave equation [72]

$$\frac{\partial^2 \phi}{\partial \psi^2} = \gamma_p^2 \beta \left(1 - \frac{1 + a^2}{\gamma_p^2 (1 + \phi)^2}\right)^{-1/2} - \gamma_p^2 \ ,$$

from which maximum and minimum field amplitudes behind the laser driver can be expressed as

$$\phi_{min,max} = \hat{E}_{max}/2 \pm \beta_p \sqrt{(1 + \hat{E}_{max}^2/2)^2 - 1} \ ,$$

where $\hat{E}_{max} = E_{max}/E_0$ and $E_0 = m_e c \omega_p / e$. If the electron is born at rest at the phase of maximum potential, $\phi(\psi_i) = \phi_{max}$, then $\phi_{min} - \phi_{max} = 2\beta_p \sqrt{(1 + \hat{E}_{max}^2/2)^2 - 1}$, and the minimum trapping condition becomes

$$-(\phi_{min} - \phi_{max}) = -2\beta_p \sqrt{(1 + \hat{E}_{max}^2/2)^2 - 1} \geq 1 - \sqrt{1 + a_\perp^2(\psi_i)}/\gamma_p \ ,$$

where the left side is the maximum energy the electron can gain from the wake after ionization, and needs to be larger than the threshold value determined by ϕ_{min} and γ_p.

Since the electron is ionized near the peak of laser electric field, where $a_\perp(\psi_i) \ll 1$, $\gamma_\perp \approx 1$, the condition reduces to

$$\phi_{min} - \phi_{max} = 2\beta_p\sqrt{(1+\hat{E}^2_{max}/2)^2 - 1} \geq 1 - 1/\gamma_p \ .$$

In general, for an electron born at an arbitrary phase ψ_i, the trapping condition is

$$\phi(\psi_i) - \phi_{min} \geq 1 - 1/\gamma_p \ .$$

For $\gamma_p \gg 1$ and $\beta_p \to 1$, as common for acceleration in underdense plasma, the trapping condition reduces to

$$2\sqrt{(1+\hat{E}^2_{max}/2)^2 - 1} \geq 1 \ .$$

Solving for $\hat{E}_{max}$ gives an approximation of a minimum trapping field requirement at optimal ionization phase $\phi(\psi_i) = \phi_{max}$ [73]

$$\frac{E_{max}}{E_0} \geq \sqrt{\sqrt{5} - 2} \approx 0.49 \ .$$

As an approximation, for a linearly polarized optimized Gaussian drive pulse in the 1D limit the maximum electric field amplitude is $E_{max}/E_0 = (\pi/2e)^{1/2}(a_0^2/2)(1 + a_0^2/2)^{-1/2}$, which gives $a_0 > 1.3$, and for circularly polarized, $E_{max}/E_0 = (\pi/2e)^{1/2}(a_0^2)(1 + a_0^2)^{-1/2}$, giving $a_0 > 0.94$.

For single pulse ionization injection, electrons are typically not ionized at the optimal phase. As detailed by Chen et al. 2006 [64], in ionization injection using a single pulse, electrons are ionized at the peak of the drive pulse where $\phi_(\psi_i) = \phi(\psi_{peak})$, and the trapping condition is

$$\phi(\psi_{peak}) - \phi_{min} \geq 1 - 1/\gamma_p \ .$$

Electrons, ionized in the decelerating phase of the wake, slip back until they reach the accelerating phase, at ϕ_{min}. The wake field must have sufficient amplitude to subsequently accelerate them to $v > v_p$ if the electrons are to be trapped and requires $a_0 > 1.7$ for electrons ionized at the peak to be trapped.

The trapping condition sets requirements on wake amplitude, and, therefore, drive laser and plasma density properties. The plasma wave amplitude must be large enough that an electron born within it will be trapped and accelerated by the wake. We have shown the minimum requirements in the one dimension cold fluid limit for trapping an electron born at rest within the optimal phase of the wake. Next we discuss factors which determine electron beam thermal emittance. These factors set conditions on the properties of the laser that ionizes electrons within the trapping phase of the wake as well as conditions on gas selection.

2.2 Emittance of Ionization Injection

Beam root-mean-square normalized emittance quantifies the variance in transverse position and momentum of electrons in the beam. The quantity is defined in units of meter-rad,

$$\epsilon_{xn} = \sqrt{< x^2 >< u_x^2 > - < xu_x >^2} \ .$$

Here,

$$\sigma_x^2 =< x^2 >= \int\int x^2 f(x,p_x) dx dp_x$$

is the variance or rms spread in position x, and $f(x,p_x)$ is the particle distribution function as a function of space and momentum.

$$\sigma_{p_x}^2 =< u_x^2 >= \int\int u_x^2 f(x,p_x) dx dp_x$$

is the variance in normalized momentum, $u_x = p_x/mc$, and

$$\sigma_{xp_x} =< xu_x >= \int\int xu_x f(x,p_x) dx dp_x$$

is a correlation term. The rms normalized emittance is conserved during acceleration with linear focusing forces.

The estimate of minimum trapping condition in the previous section used the approximation that the injected electron be ionized at rest at an optimal wake phase. Laser pulses, however, have finite spatial and temporal extents and their ionization volume is finite, therefore electrons emerge with variation in position, momentum and injected wake phase. The initial emittance of the electron beam, gained upon ionization, is its thermal emittance and is determined by, and thus sets conditions on, injection laser properties.

Schroeder et al. 2014 [38] detailed factors that determine emittance of ionization injected electron beams and showed that normalized thermal emittance in the injection laser polarization direction can be approximated as

$$\epsilon_x \approx \frac{a_i w_i \Delta^2}{\sqrt{2}} = \frac{3\pi}{\sqrt{2}} \frac{r_e}{\alpha^4} \left(\frac{U_H}{U_I}\right)^{3/2} \frac{w_i a_i^2}{\lambda_i} \ ,$$

for normalized laser field amplitude $\Delta^2 \ll 1$, and for variance in injection laser field phase in which the electrons were ionized $\sigma_\psi \approx \Delta \ll 1$, i.e. ionization occurs near peak laser electric field. Here,

$$\Delta = \left(\frac{3}{2}\frac{E_p}{E_a}\right)^{1/2} \left(\frac{U_H}{U_I}\right)^{1/2} \ ,$$

and assumes tunneling ionization to be the dominant ionization mechanism, which is valid for Keldysh parameter $\gamma_k = \sqrt{U_I/2U_p} < 1$, where $U_p = m_e c^2 a_i^2/4$ is the electron oscillation energy, and U_I is the ionization potential of the electron. Electrons are assumed to be ionized from rest. Here E_p is the peak electric field, and $E_a = e/r_B$ the atomic field, where $r_B = r_e/\alpha^2$ is the Bohr radius, $r_e = e^2/m_e c^2$ is the classical electron radius, and $\alpha = e^2/\hbar c$ is the fine structure constant. $U_H = m_e c^2 \alpha^2/2 = 13.6\ eV$ is the ionization potential of hydrogen.

This result includes variance due to ionization off laser field peak, off envelope peak, and off laser propagation direction axis. Initial momentum gain is due to ionization at various phases of the laser pulse. If ionized at the peak of the laser field oscillations, $a_\perp = 0$. Otherwise, a finite amount of transverse momentum along the laser polarization direction is gained by the electron from interacting with the laser field and remains when the laser passes. Electrons ionized off-axis lead to position spread proportional to the laser spot size w_i. In addition, off-axis injection further contributes to momentum spread by beam interaction with the injection laser's ponderomotive force.

In terms of intensity, $a_i = 0.85\ \lambda_i[\mu m]\sqrt{I_i[10^{18}W/cm^2]}$, normalized thermal emittance is

$$\epsilon_x \approx 4.5 \times U_I[eV]^{-3/2} w_i[\mu m]\ \lambda_i\ [\mu m]\ I_i\ [10^{18}W/cm^2]\ ,$$

which is a function of electron ionization potential, and ionization laser beam radius, intensity and wavelength. Thus, emittance can be minimized by using an injection laser whose intensity is just above ionization threshold, is tightly focusing, and is of short wavelength. Decreasing laser focus radius, however, significantly reduces final charge,

$$Q \approx \pi w_i^2 l_i f_i e n_g\ ,$$

where n_g is the gas density, $f = n/n_g$ is the ionization fraction, and l is the ionization length, which, unless self-focused and guided, or guided by a preformed plasma channel, is limited by diffraction, $l \approx z_R = \pi w_i^2/\lambda$, or by the extent of the high Z gas.

After ionization, and exiting the injection laser field, off-axis electrons experience transverse focusing / defocusing forces from the wake. For a symmetric wake, electrons born on the longitudinal axis experience equal and opposite transverse forces, but those born off-axis begin to oscillate about the axis at a frequency $\omega_\beta = \omega_p \kappa/\sqrt{\gamma}$, where κ is the focusing constant that is $1/\sqrt{2}$ for the bubble or blowout regime [74]. Unless the beam is matched to the wake focusing forces, such that $k_\beta \sigma_\perp = \sigma_{p_\perp}$, and $r_\beta = \sqrt{\sigma_\perp^2 + \sigma_{p_\perp}^2/k_\beta^2} = \sqrt{2}\sigma_\perp \approx w_i \Delta$, the resulting phase mixing will lead to emittance growth that saturates at

$$\epsilon_\perp = k_\beta < r_\beta^2 > /2\ .$$

For small variation in ionization phase, assuming ionization occurs at the peaks of the electric field,

$$\sigma_{px} \simeq a_i \Delta\ ,$$

while the rms spread in transverse position of ionized electrons in the limit $\Delta \ll 1$ is,

$$\sigma_x = w_i \Delta/\sqrt{2}\ .$$

This gives

$$\epsilon_x = k_\beta < r_\beta^2 > /2 = k_\beta/2(\sigma_\perp^2 + \sigma_{p_\perp}^2/k_{\beta 0}^2) = k_\beta/2(w_i^2\Delta^2/2 + a_i^2\Delta^2/k_{\beta 0}^2) \ ,$$

and finally

$$\epsilon_x = k_{\beta 0}\omega_i^2 \left[1 + \frac{2a^2}{(k_{\beta 0}\omega_i)^2}\right] \frac{a_i}{\lambda_i} \left(\frac{3\pi r_e}{4\alpha^4}\right) \left(\frac{U_H}{U_i}\right)^{3/2} \ .$$

Out of the axis of the laser polarization, however, where the ionized electron does not experience the residual transverse momentum from the ionizing laser, the emittance is,

$$\epsilon_y = k_{\beta 0}\omega_i^2 \frac{a_i}{\lambda_i} (\frac{3\pi r_e}{4\alpha^4})(\frac{U_H}{U_i})^{3/2} \ .$$

Note that higher 6D brightness is achieved with a linearly polarized injection laser compared to a circularly polarized injection pulse, since brightness

$$B_{6D} = I_b/\sigma_E \epsilon_x \epsilon_y \ ,$$

depends on both ϵ_x and ϵ_y, where I_b is the beam current and σ_E is the energy spread.

2.3 Progress Toward Ultralow Emittance with Two-Color Ionization Injection

Ionization injection was first suggested by Umstaedter et al. in 1996 [58], where a controlled injection configuration was proposed, in which, after an initial laser pulse drives a wake that is below wave breaking, a trailing pulse, orthogonal to the first, locally dephases wake electrons into a trapping phase. The paper concludes with the foresight that the same configuration could be used for ionization and injection of deeply bound inner shell electrons of a high Z gas that have an appearance intensity for tunneling ionization below that of the injection pulse but above that of the pump pulse. Ionization injection, as well as the orthogonal trailing pulse configuration was elaborated and published by Chen et al. in 2006[64].

The first experimental demonstrations of ionization injection drove the wake and ionized accelerated particles using one pulse. Simple and elegant, with proper high Z gas selection, a single pulse can ionize and drive a wake consisting of low ionization threshold electrons using the front of the pulse, then, with the peak of the pulse, ionize inner shell electrons inside of the wake in a trapping phase. Oz et al. 2007 [75] produced 7.6 GeV from ionization injection in a 28.5 GeV electron beam driven plasma wave using a lithium vapor column doped with helium atoms.

Shortly following, Rowlands-Rees et al. 2008 [76] found evidence of ionization injection during investigations of plasma channel guided laser wakefield acceleration using sapphire capillaries that produced 128 ± 15 MeV electron beams. Evidence suggested that ionization of aluminum and oxygen particles from the capillary walls contributed to the accelerated electron population and led to the suggestion that localized addition of gases not fully ionized by the initial plasma channel forming discharge could be used to control the injection position of accelerated electrons.

In 2010 three groups independently reported experimental studies of single pulse ionization injection in laser driven wakefields using gas mixtures [68, 66, 65]. Accelerated electron beams emerged with large energy spectra. Although relative energy spread can be decreased by further accelerating beams in a second stage [67, 69], ultimately control of beam properties requires localization of injection.

Localization can be achieved by limiting either the region in which ionization can happen, and/or the region in which trapping conditions are satisfied. Limiting the ionization region using a single pulse has been achieved with targets in which only a small extent of the gas contains a high Z gas [67, 69, 77, 3]. Laser evolution, such as self-focusing [78], mismatched guiding [79, 80], as well as wake evolution, and beam loading have been used to truncate trapping conditions [81, 82] and thus localize injection, however nonlinear evolution is difficult to control.

In order to further tune the process, techniques to localize injection using two pulses, such as orthogonal ionization injection [58, 83, 64], collinear injection with smaller f# injector laser [84, 85, 86], colliding pulse [59, 87, 88], and beatwave injection [89, 90, 91, 92], were quickly adapted to ionization injection.

Beginning in 2012, a series of papers were published investigating the use of two trailing pulses with different wavelengths for ionization injection into a preformed wake in order to produce ultra-low emittance electron beams. By trailing the injection pulse, the injection process is isolated from properties of the drive beam. Once isolated the drive and injector can be independently optimized for high trapping potential wake generation and ionization injection of low emittance beams.

Trapping requires sufficient ponderomotive potential to generate large amplitude waves. In addition, after trapping, acceleration to high energies requires long acceleration lengths and low densities. Thus a drive might be designed to have long z_R, matched to wake focusing forces, and/or be guided, in addition to delivering high a_0, achieved either by high intensity or long wavelengths. Ionization with low emittance begins with low a_i and localization in space and time relative to the plasma wavelength. Low a_i reduces the electromagnetic field felt by the electron when it is born. In addition, significant ponderomotive potential contribution, $a_i \geq 1$, from the injector can strongly perturb the preformed wake. However, while maintaining low ponderomotive potential, the injector laser must be intense enough to ionize bound inner shell electrons. Since $a_i = 0.85\ \lambda_i[\mu\mathrm{m}]\sqrt{I_i[10^{18}\mathrm{W/cm}^2]}$ is a function of both intensity and wavelength, the injector can be of higher intensity than the drive, provided it is of much shorter wavelength.

Hidding et al. 2012 [70] first introduced the concept that they called the “Trojan Horse”. In this analysis, a wake driven by an electron beam in hydrogen, followed by a laser that ionizes and injects helium electrons with very low residual momentum, is proposed. It is mentioned that although both wake and injection could be generated by laser pulses, the beam driven wake has many advantages. For example, field ionization by the beam driver is small, reducing requirements on the injector. Since a laser drives a wake via ponderomotive force, laser intensities of $\sim 10^{18}$ W/cm^2 are required. Normalized emittance on the order of nm rad are possible [93]. Initial experiments were performed at SLAC in 2017 [94, 95].

Yu et al. 2013 [96, 36] published an all-optical two-color ionization injection scheme. All-optical configurations offer compactness, and, thus, are of great interest to potential users. Yu et al. proposed using a gas target containing a short region of krypton gas for localized ionization injection, followed by a post acceleration region with a low Z gas. A 5 μm wavelength pulse is used to excite the wake, followed by a 400 nm wavelength injection pulse that ionizes inner shell electrons in the trapping phase of the wake. PIC simulations show normalized transverse momentum $\epsilon \approx 0.03$ mm mrad, an order of magnitude less than for single pulse ionization injection [71].

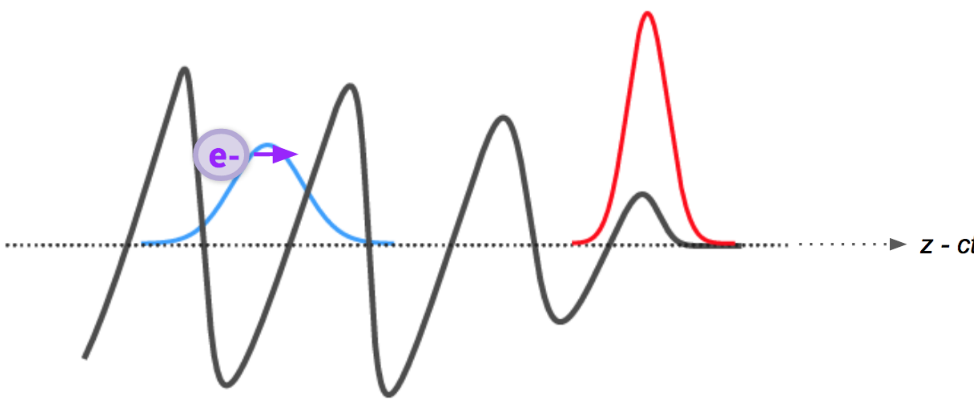

Figure 2.2: Schematic of two-color ionization injection showing a drive pulse (red) that generates the wakefield, the resulting density perturbation (grey), the trailing injector pulse (blue) and injected electron beam (purple).

Fig. 2.2 shows a schematic of two-color ionization injection. A single circularly polarized wake driver, shown in red, excites a wake. The drive pulse is then followed by a short wavelength injector laser with higher intensity but lower a_0 than that of the drive, shown in blue. The injector laser is timed to ionize at the optimal phase in the wake and does not overlap with the drive so that ionized electrons are born only in the field of the injector laser.

Xu et al. 2014 [37] investigated, with PIC simulations, both collinear and colliding pulse geometries for two-color ionization injection using 10 μm and 400 nm laser pulses as well as the effects of phase mixing [74], and showed that $\sim$10 fs electron beams, with $\sim$4 pC of charge, and $\sim$50 nm rad normalized emittance, could be generated, an order of magnitude smaller than that resulting from using a single wavelength.

Two-color three pulse colliding pulse injection techniques were also proposed, where, behind the drive, two beams transverse to the drive collide, and locally ionize electrons with residual momentum in the longitudinal direction [88, 60, 77]. Besides added experimental complexity in utilizing three beams, although ponderomotive force on the injected electrons is longitudinal, injection off-axis in the beatwave volume contributes to final transverse momentum leading to 0.1 mm mrad level emittance beams, similar to that produced by previously explored two pulse schemes.

Although not necessarily undesirable, large ponderomotive force drives can be accompanied by nonlinear effects, leading to pulse and wake evolution. Moreover, a high field drive demands an even higher field ionization injector. Thus techniques to lower a_0 of the drive while maintaining the ability of the drive laser to generate high amplitude waves are critical.

Schroeder et al. 2014 [38] published a thorough study of thermal emittance of ionization injected beams. In this study, a two-color ionization injection setup was studied, in which the drive pulse was circularly polarized and matched to the plasma density. Resonant excitation, using circularly polarized pulses, beatwave excitation [91], or multi-pulse drives [97, 98], can be used to lower drive a_0, and thus a_i requirements while driving large amplitude wakes.

Beginning in 2017, Tomassini et al. [97] began publishing a series of studies of two-color ionization injection using a resonant multi-pulse drive laser to lower both drive and injector requirements, and electron beam emittance, which they called resonant multi-pulse ionization injection, ReMPII. Detailed simulations studied the case of a multi-pulse drive at 800 nm wavelength followed by an injector pulse at the second harmonic at 400 nm wavelength. Simulations showed as low as 80 μm mrad normalized emittance beams with 0.65% energy spread can be obtained with a 100 TW-class Ti:Sapphire laser system.

The use of trailing pulses with two different colors to control injection in LPAs was tested by Li et al. 2019 [99], where an initial pulse at λ_0 = 800 nm with a_0=1.74 was followed by λ_i = 400 nm with a_i=1.81. Results showed increased energy and charge when the two pulses coincided, but since the ponderomotive potential of both drive and injector were well above relativistic, results were comparable to single pulse ionization injection [100].

Ionization injection with trailing pulses with the same laser frequency but different f-number, proposed by [84], was experimentally demonstrated recently by von der Leyen et al. 2023 [86]. F-number f/40 was used for the drive and f/3.8 for the injector, both with wavelength λ = 800 nm. Ponderomotive potentials were measured to be a_0 = 0.75, and a_i = 2.46. Results showed injection and acceleration occurred only with delay within 12 μm, consistent with laser triggered injection in $\lambda_p = 16$ μm. Again, due to the large transverse momentum imparted by the ionization injector, simulations gave normalized rms emittance $\epsilon_{n,rms}$= 3.7 μm, orders of magnitude greater than required for high brightness applications.

To date, collinear all-optical two-color ionization injection has yet to be demonstrated in the laboratory. In the next four chapters, progress toward a demonstration experiment of collinear two-color ionization injection using two beams of a Ti:Sapphire based laser system will be presented.

Chapter 3

Progress Toward Proof of Principle Experiment: Wake Driver

Two step ionization injection schemes open a parameter space in which injection and acceleration can be decoupled, potentially facilitating generation of ultra-low emittance beams. The wake driver, ahead of the injection point and no longer responsible for ionization of accelerated electrons, need only to be optimized for generating a high amplitude wake that can accelerate to high energies without self-injecting or fully ionizing the gas. The trailing injector can be separately optimized for generation of low emittance beams. Injector intensity must be sufficient to ionize inner shell electrons and yet impart low ponderomotive force on the electron and the existing wake. Both injector requirements can simultaneously be satisfied by increasing the injector laser frequency relative to that of the drive.

This chapter is the first in four that detail the design and component testing of a two-color ionization injection proof-of-principle experiment on the hundred terawatt Thomson (HTT) system at the BELLA Center at Lawrence Berkeley National Laboratory (LBNL). The system is a Ti:sapphire based laser system with center wavelength $\lambda_0 = 800$ nm that is divided into two primary beams, with energies 3 J and 1 J before compression, and a 1 mJ probe line.

The section begins with optimization of the wake driver and requirements for gas selection. The gas species from which the two populations of electrons, those that form the wake and those that accelerate, are drawn, must contain bound electrons after wake formation, and yet have electronic levels easily ionized by the ionization injector. In order to aid large amplitude wake formation with low E, and thus ensure bound electrons remain, a method of forced resonant excitation by use of circular polarized drive pulses was investigated.

For an ionization injector the third harmonic of 800 nm was chosen. Focused to a quarter of the diameter of the drive, the injector achieves high intensity for ionization while maintaining a third of the a_0 for the same intensity at the fundamental frequency. The higher frequency has the added advantage of having a smaller diffraction limited focal size than for the fundamental in a given focal geometry, aiding intensity requirements and diminishing emittance $\epsilon \propto w_0^2$ by limiting ionization area. Results of high intensity short pulse harmonic generation are reported in Chapter 4. Target design and qualification are discussed in Chapter 5. Finally, Chapter 6 summarizes methods of overlap of the injector with the preformed wake and results of experimental implementation of these methods.

3.1 Gas Selection

Trapping conditions set the necessary wake amplitude for a given ionization injection phase. As shown in the preceding chapter, the minimum required wake amplitude is for an electron injected at the wake phase with maximum potential and can be generated with $a_0 \approx 1$ using a single circularly polarized pulse. This injection phase requirement is highly restrictive to single pulse ionization injection but is easily achievable using an independently timed trailing ionization injecting laser pulse.

While the lower limit for a_0 for the drive laser is set by trapping conditions, the upper limit is set by deleterious nonlinear effects, and conditions for ionization of injected electrons at low emittance. Ionization injection takes advantage of high-Z gases so that lower ionization threshold electrons can be used for wake generation while higher ones can be left for further ionization injection. It is often advantageous to use gases that have a distinct separation in ionization thresholds between two populations of electrons. For example, in nitrogen, an ionization potential threshold gap exists between its L and K shells. The potential gap gives the driver laser freedom to accomplish wake formation while ensuring that bound electrons remain for injection. It also provides robustness to drive intensity fluctuation and evolution.

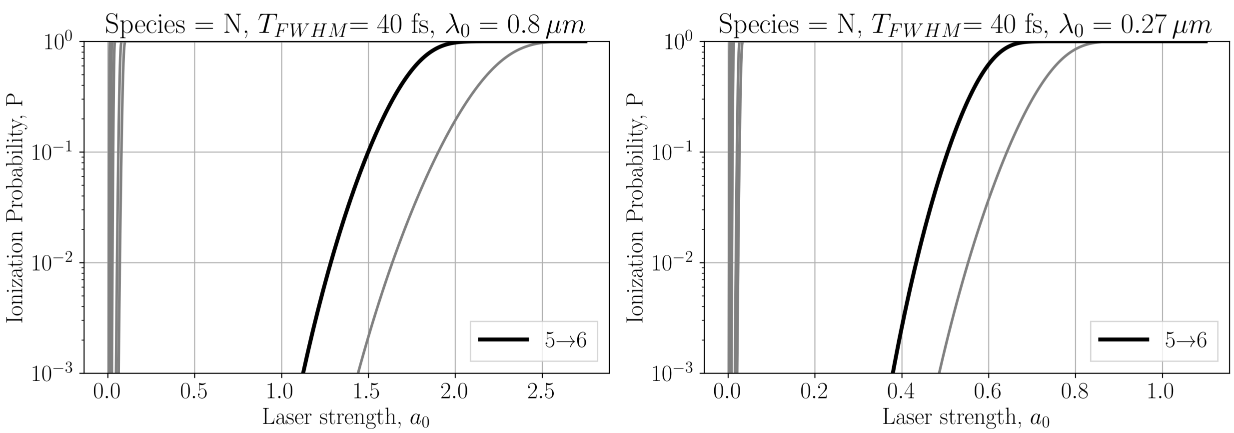

Figure 3.1: Tunneling ionization probability as a function of a_0 for nitrogen for $\lambda = 800$ nm (left) and $\lambda = 267$ nm (right).

Fig. 3.1 shows the tunneling ionization probability for nitrogen as an example of a commonly used gas for ionization injection. A single laser pulse could be designed to ionize the first 5 states with the front of the pulse, creating the accelerating wake, then ionize states

6 and 7 locally at the peak of the pulse [71]. In order to ionize the first five electrons from nitrogen, the laser intensity need only exceed 1.5×10^{15} W/cm^2 (54.4 eV), but in order to ionize the next electron, it must surpass 1.9×10^{19} W/cm^2 (522 eV). For reference, a laser strength parameter of $a_0 = 1$ for a $\lambda = 800$ nm wavelength laser corresponds to 4.3×10^{18} W/cm^2. Since the L shell levels are easily ionized, they are ionized by the foot of the drive laser pulse, such that the remainder of the pulse sees a uniform plasma density and does not experience defocusing from ionization.

The ionization threshold of the inner shell electrons, on the other hand, determine the minimum intensity required of the ionization injection laser. Were that laser to have a wavelength of 800 nm, a laser strength parameter of $a_i \approx 1.4$ would be required, and at this amplitude the electron born within it would acquire a large residual transverse momentum. One way of decreasing a_i experienced by the injected electrons is to decrease the wavelength of the injecting laser. As seen in Fig.3.1, when the wavelength of the injecting laser is a third of that of the drive, the normalized vector potential required to ionize is reduced to $a_i > 0.4$. Decreasing the wavelength further would further decrease residual transverse momentum gained by these electrons.

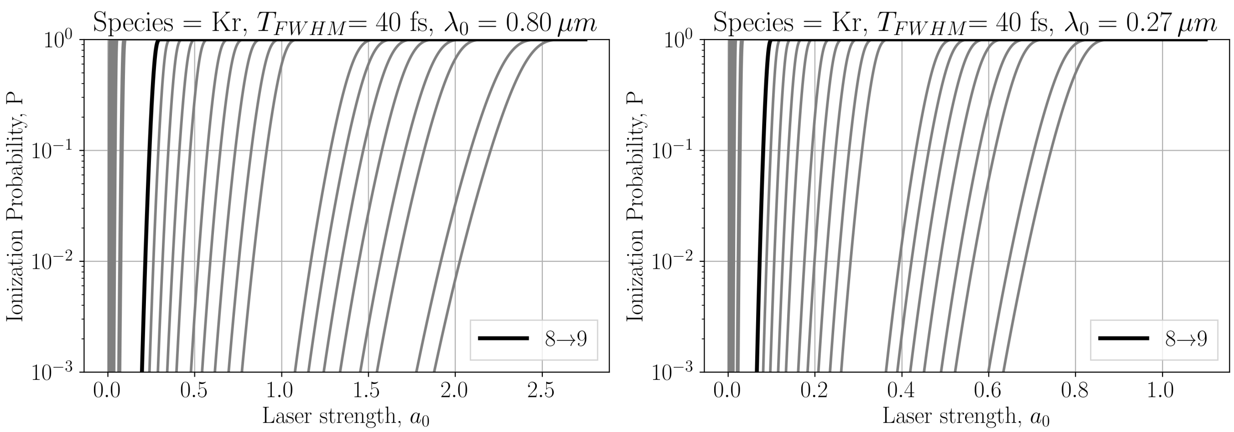

Figure 3.2: Tunneling ionization probability as a function of a_0 for krypton for $\lambda = 800$ nm (left) and $\lambda = 267$ nm (right).

Requirements for the injector pulse can be decreased by reducing the a_0 of the drive laser necessary to drive a wake with sufficient amplitude to trap. From Fig. 3.1 it can be seen that the minimum required $a_0 \sim 1$ for a linearly polarized pulse is near the ionization threshold of the inner shell electrons of nitrogen such that nonlinear effects, such as self-focusing, can easily increase laser intensity to above the ionization threshold of inner shell electrons. Resonant excitation by multiple pulses with the equivalent total energy of a single pulse, or changing the drive pulse from linear to circular polarization, or both, can be an effective way to reduce drive a_0 while maintaining drive effectiveness in generating a sufficient wake. Were a_0, and thus the intensity, of the drive pulse to be reduced, a gas such as krypton, with a gap at Kr7+ (125.8 eV) and Kr8+ (233 eV) could be used, reducing energy requirements for the injector pulse as well as thermal emittance. The ionization probability for the krypton atom is shown in Fig. 3.2.

In this next section, experimental results of wake generation using a circularly polarized drive laser will be discussed, which show that ample amplitude wakes can be driven that are dark-current-free and leave inner shell electrons bound for controlled injection by a properly phased trailing injection laser.

3.2 Circularly Polarized Drive

Experiments comparing wake generation with linearly (LP) and circularly polarized (CP) drive pulses were performed to assess compatibility of a CP drive for dark-current-free high amplitude wake generation in a nitrogen-doped helium plasma.

Multi-pulse drives have been explored for high amplitude wake generation while maintaining low intensity per pulse. In the context of a wake driver for ionization injection, a multi-pulse wake driver can be used to generate wake amplitudes sufficient to trap and accelerate, while maintaining low intensity to leave high-ionization-threshold electrons bound for further independent controlled injection.

For square pulses in the linear regime, neglecting ion motion, wakes can be resonantly driven by multiple pulses, as a driven harmonic oscillator, with plasma wake amplitude,

$$E_{max}/E_0 = Na_0^2$$

where N is the number of pulses. Resonant excitation is most efficient when the pulse length is approximately $L = \lambda_p/2$ and pulse separation is approximately $(2l+1)\lambda_p/2$, where l is an integer. In the nonlinear regime, however, since the plasma wavelength increases for each succeeding waves behind the laser pulse, both pulse length and pulse separation need to be individually optimized to achieve resonant excitation [101]. The challenge is multiplied with increasingly long pulse trains [102, 103, 104].

A circularly polarized drive can be used to circumvent requirements for individual pulse optimization in the nonlinear regime while generating equivalent wake amplitudes to the two pulse, $N = 2$, case.

For a circularly polarized electric field,

$$E_{CP} = (E_L \cos kz\ \hat{i} + E_L \sin kz\ \hat{j})/\sqrt{2} = (E_x\hat{i} + E_y\hat{j})\sqrt{2}\ .$$

Therefore, $a_{0CP}^2 \sim E_{CP}^2 = E_x^2/2 + E_y^2/2$, $a_T^2 = 2a_{0LP}^2/2 = a_{0LP}^2$, where a_T is the total effective normalized laser potential. The generated wake amplitude is theoretically equivalent to that generated by a linearly polarized drive, but each polarization direction is less intense. In addition, although the ponderomotive force imparted by a CP drive is equivalent to a drive divided into two pulses, since the two polarizations are coincident, they do not need to be separately optimized for pulse evolution in succeeding waves.

Experiments were performed with a laser with 1 J of energy on target in a 33 fs FWHM pulse length and 20 μm spot size in plasma densities in the range of $2 - 8 \times 10^{18}$ cm^{-3}. The target was formed by a supersonic gas jet, forming 3 mm of accelerator propagation distance, with 0.5% nitrogen in helium gas. It is common to use a low Z gas that is doped with a small amount of high Z gas to decrease ionization defocusing. Ionization defocusing from the drive laser entering, ionizing and experiencing a significant ionization gradient, can greatly reduce achievable intensities in a high-Z gas [105]. Helium, with ionization potential of 54.4 eV for He^{2+}, is fully ionized at the head of the drive pulse, reducing ionization defocusing effects.

The drive laser was transformed from linear to circular polarization via a zero-order air-spaced quartz quarter-wave plate for $\lambda = 800$ nm inserted after pulse compression and just before the drive focusing optic. Although more sensitive to potential deleterious effects of nonlinear propagation through media, the optic could not be placed before compression due to polarization sensitive compressor grating reflectance. This placement, however, requires the wave plate be as large as the most expanded portion of the beamline. In addition to increased costs, the structural integrity of a large diameter optic sets a lower limit on optic thickness to ~ 1 mm.

A quartz quarter-wave plate was selected because quartz crystal is transparent across a broad spectrum and can be made up to around 90 mm wide. Sapphire can also be used, although at considerably higher cost. Mica can be obtained easily in large apertures at true zero order and was used at CoRELs PW system for circular polarization [29]. When using such thin mica, however, anti-reflective coating is difficult to apply and, due to absorption and reflection, 12-14% loss occurs compared to around 2% energy loss with properly coated quartz.

Post interaction laser spectra were measured to monitor ionization effects (blue shifting) as well as wake generation (red shifting). Plasma density was monitored by wavefront detection of a separate 1 mJ laser propagating transversely to the drive through the interaction point. Electron beam profile was measured by interaction with a scintillating screen, while charge spectrum was measured via a 3 Tesla magnetic spectrometer.

Redshift of the post interaction optical spectrum can be used to indicate wake amplitude. The pulse that drives the wake subsequently experiences the density gradient of the wake. Near the front of the wake the electron density is high compared to the plasma density experienced by the rear of the pulse. Thus, the local phase velocity of the rear of the pulse, $\beta_p = v_p/c \simeq 1 + \omega_p^2(\zeta)/2\omega^2$, is less than that of the front. Assuming a plasma wave with $v_p = v_g$, such that $\delta k_p^2(\zeta) = k_{p0}^2 \delta n(\zeta)/n_0$, where $\delta n(\zeta) = \delta n_0 \sin k_p \zeta$, the frequency shift can be estimated as

$$\frac{\Delta\omega}{\omega_0} = -\pi \frac{\omega_p^2}{\omega_0^2} \frac{\delta n_0}{n_0} \frac{v_g \tau}{\lambda_p} \cos k_p \zeta \ ,$$

where ω_0 is the original frequency [106, 2].

Fig. 3.3 shows charge and optical spectral redshift as a function of electron plasma density for linearly and circularly polarized drive lasers. It can be seen that charge is injected and

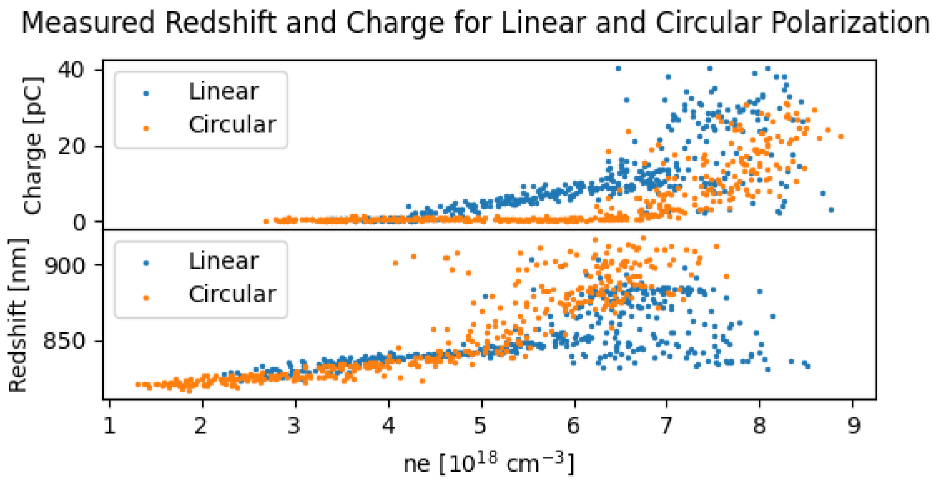

Figure 3.3: Measured charge (top) and optical spectral redshift (bottom) for linearly and circularly polarized drives as a function of plasma density.

accelerated for $n_e > 4 \times 10^{18}$ cm^{-3} when using a linearly polarized drive, whereas charge injection requires higher densities, $n_e > 6 \times 10^{18}$ cm^{-3}, when using a circularly polarized drive. Comparison of the post interaction optical redshift, however, indicates that generated wake amplitudes are nearly identical. In both cases, as density increases, self-focusing begins to take effect, increasing laser intensity, and the phase velocity of the wake decreases, lowering the trapping threshold.

Comparison measurements made with pure and nitrogen-doped helium confirmed that the injection mechanism was indeed ionization injection. Fig. 3.4 shows that removing the high Z dopant resulted in no injection but equivalent redshift.

Simulations were performed with the WarpX PIC code, an open source code with advanced algorithms for plasma acceleration [107]. RZ geometry was used in the boosted frame with field ionization from neutral gas and partially pre-ionized plasmas.

Fig. 3.5 shows two slices of time, $t = 0$ and $t = 1$ ps, shortly after injection. Characteristic of single pulse ionization injection, K shell elections are ionized near the peak of the drive pulse and slip back. Those that gain velocities $v_z > v_p$ become trapped and accelerated.

Fig. 3.6 shows that while the the initial laser strength parameter is $a_0 = 0.7$, self focusing and pulse compression increase it to $a_0 = 2.4$ in the linearly polarized case and $a_0 = 1.7$ in the circularly polarized case for the highest densities. For both cases, charge is injected for $a_0 > 1.6$ as estimated in the previous section for single pulse ionization injection. Wake amplitude of the two cases are nearly identical until significant charge is injected as in the linearly polarized case, leading to beam loading and suppression of wake amplitude.

Note also in Fig. 3.6 that in the linearly polarized case, injection and trapping requirements are reached twice, shown by the two peaks in injected charge over time. This

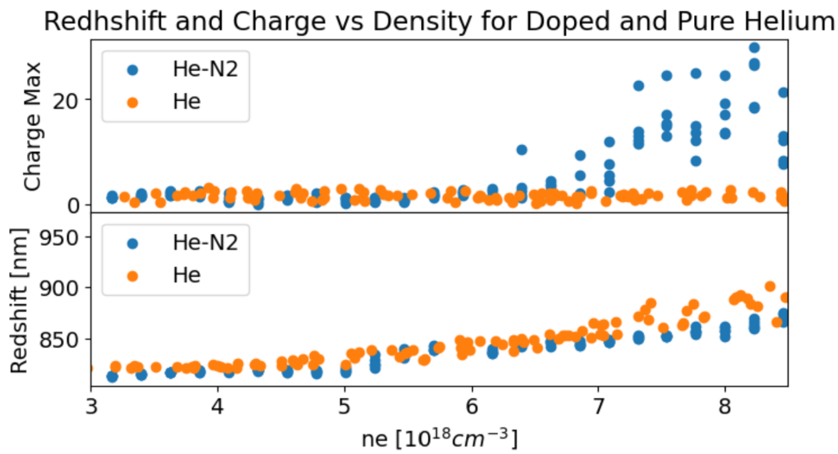

Figure 3.4: Measured electron beam charge (top) and post interaction optical spectral redshift (bottom) plotted for linearly polarized pulse using pure helium vs nitrogen-doped helium.

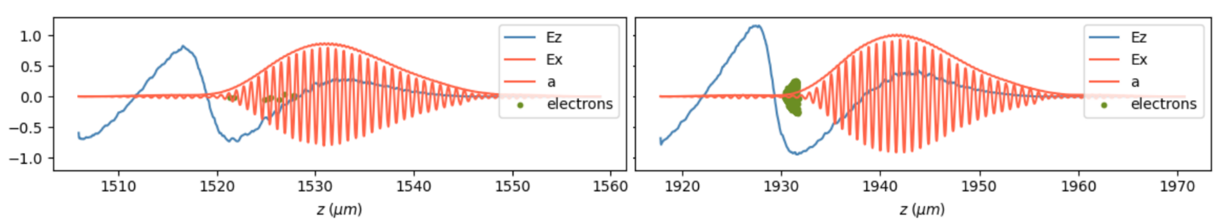

Figure 3.5: Simulation slices showing normalized values of E_z, E_x, a_0 and electrons shortly after injection for initial $a_0 = 0.7$, linearly polarized, with background plasma density $n_0 = 5 \times 10^{18}$ cm^{-3}. Once laser field reaches that required to ionize the second shell of nitrogen, electrons are ionized at the peak of the laser field and slip back (left). After 1 ps, electrons that have gained enough longitudinal momentum become trapped and accelerated in the accelerating and focusing portion of the wake (right).

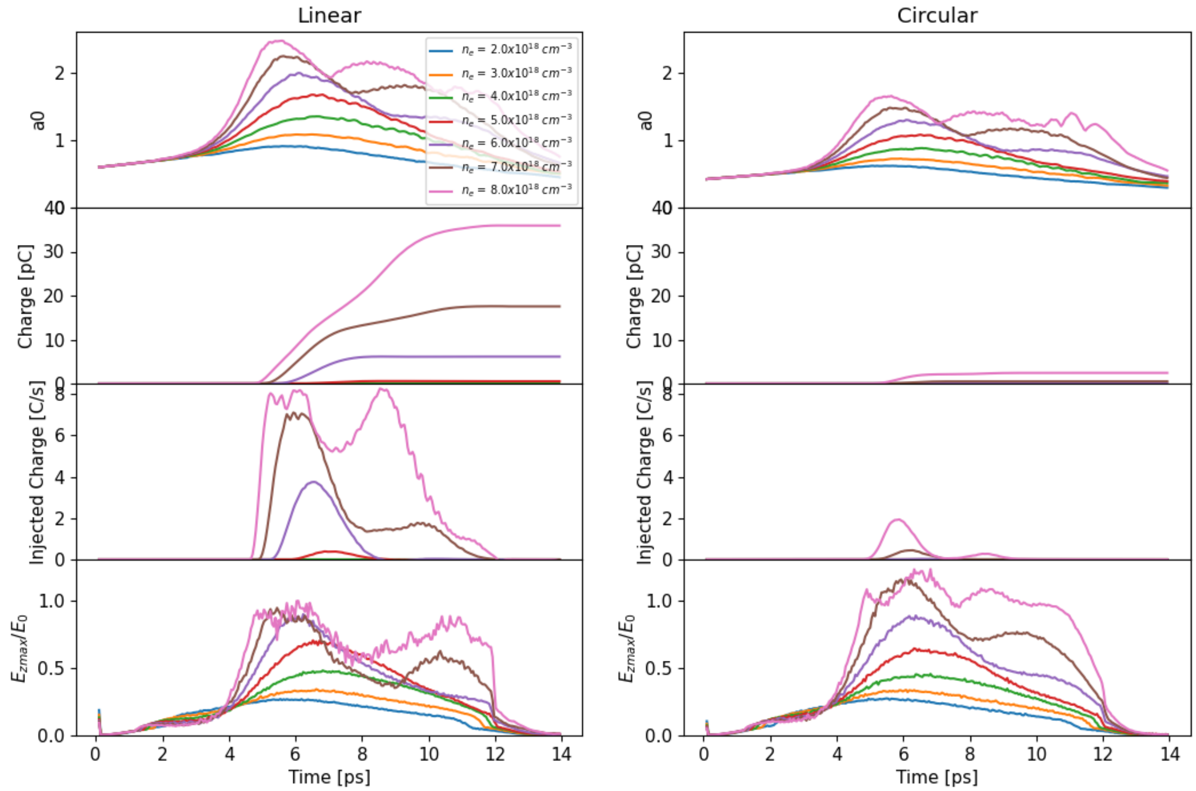

Figure 3.6: a_0, charge and maximum wake amplitude normalized to the linear wakebreaking field E_{zmax}/E_0 using circularly and linearly polarized drive lasers of equal energy a various densities as a function of time. The left column shows results for wake generation with a linearly polarized pulse with $a_0 = 0.7$ while the right column shows results from wake generation with a circularly polarized drive, modeled with two coincident perpendicularly polarized pulses, each with $a_0 = 0.7/\sqrt{2}$.

is corroborated by the measured electron beam energy spectra as shown in Fig. 3.7, which shows an electron population with 0-50 MeV energy in addition to the higher energy electron population.

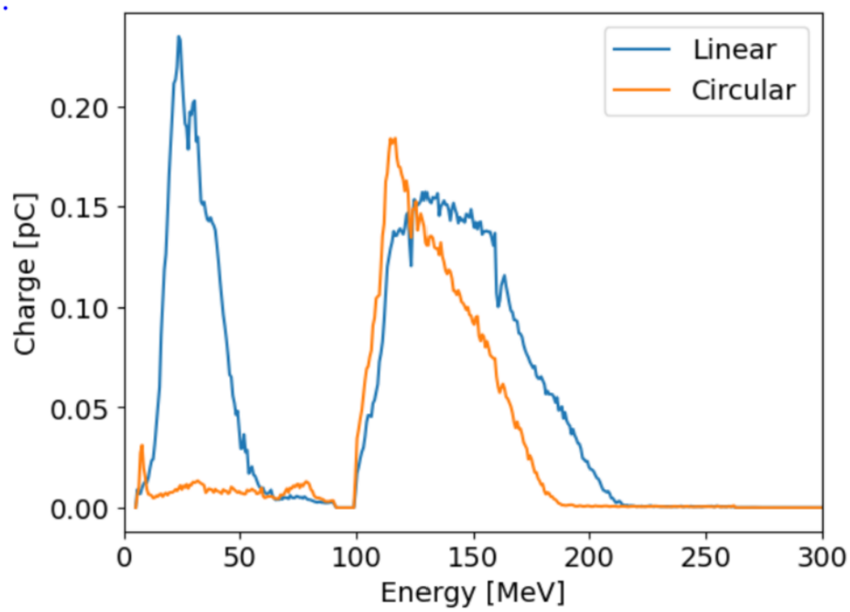

Figure 3.7: Electron beam energy spectra measured by magnetic spectrometer after acceleration by linearly and circularly polarized drive pulses. Ionization and trapping conditions were met twice when using linearly polarized drive laser pulses leading to two energy peaks.

Results show that changing the polarization of the drive laser from linear to circular is an effective and simple method to generate wakefields with high amplitude, while leaving inner shell electrons of the high-Z gas, in this study nitrogen, bound for further ionization injection. For example, a region between $n_e = 4 \times 10^{10}$ cm^{-3} and $n_e = 6 \times 10^{10}$ cm^{-3} is dark-current-free but generates a wake which can trap and accelerate.

Circular polarization has been explored in the recent years in single pulse laser wakefield acceleration to increase beam charge [108, 109], electron beam energy [108, 110], and as a circularly polarized injector in the bubble regime to generate higher energy beams [86]. The current study is the first experimental demonstration of the use of a circular polarized drive laser to prepare a dark-current-free wake for two-step ionization injection.

Chapter 4

Progress Toward Proof of Principle Experiment: Ionization Injector

The ionization injector laser requirements are set by factors that determine the beam emittance. As discussed in chapter 2, in terms of intensity, using $a_i = 0.85\,\lambda_i[\mu m]\sqrt{I_i[10^{18}W/cm^2]}$, the thermal emittance in the laser polarization direction is

$$\epsilon_x[\text{m rad}] \approx 4.5 \times U_I[eV]^{-3/2} w_i[\mu m]\ \lambda_i\ [\mu m]\ I_i\ [10^{18}W/cm^2]\ .$$

The initial beam emittance is reduced by lowering injection laser intensity, focal size and wavelength. The required injector intensity can be kept low by a combination of drive laser conditioning and gas selection. Focal size is determined by available geometry, laser beam quality, and desired charge. Short wavelength lasers that are ultrashort and high intensity, especially into UV wavelengths, however, do not exist commercially. Thus, the production of a UV laser for ionization injection forms the greater part of this study and is the subject of this chapter.

4.1 Third Harmonic Generation of High Intensity Ultrashort Lasers

While a separate laser with shorter wavelength than that of the drive can be utilized for ionization injection, synchronization at the femtosecond and micron level on target is greatly simplified if the injector shares the seed of the drive laser. This study uses a laser system that branches into two main beams before independent amplification and compression. The ionization injector is formed by converting the wavelength of one of these beams via harmonic generation.

An experimental demonstration of self-injection enhanced by a trailing second harmonic pulse was performed in 2019 by Li et al. [99], which used a_0=1.74 at λ_0 = 800 nm for the wake driver followed by a_i=1.81 at λ_i = 400 nm. Li et al. showed that, although trace amounts of a high Z gas was used, due to the large ponderomotive potential of both pulses, the dominant mechanism for injection was self-injection.

In order to demonstrate the concept of two-color ionization injection as a controlled injection injection technique that could be used to produce low emittance beams, we chose to convert the injector laser into its third harmonic, $\lambda = 267$ nm, from a $\lambda = 800$ nm laser system. Although even shorter wavelengths would benefit the demonstration, the fourth harmonic, at $\lambda = 200$ nm, for example, approaches resonant frequencies of many commonly used optical materials, where they strongly absorb, and therefore are no longer transparent.

To maximize harmonic generation efficiency, a cascaded sum-frequency generation process was used to generate the third harmonic of the fundamental wavelength, $\lambda = 800$ nm. Since both of these steps depend on second order nonlinear susceptibilities, overall conversion efficiency into the third harmonic is higher than direct third harmonic generation that relies on the third order nonlinear susceptibility [111, 112, 113, 114].

Direct third harmonic generation has demonstrated up to 3.5% conversion efficiency [115], while second harmonic generation followed by sum-frequency generation can achieve 10-20% efficiency with the parameters used in this study, and up to 80% with longer pulses [116]. A schematic of this process is shown in Fig. 4.1. Details of design, implementation, and experimental results will be discussed. Parametric scans of component parameters were performed on scaled-down, modular setups and used to benchmark a split-step harmonic generation code, which together were used to aid in design of components for high power harmonic generation.

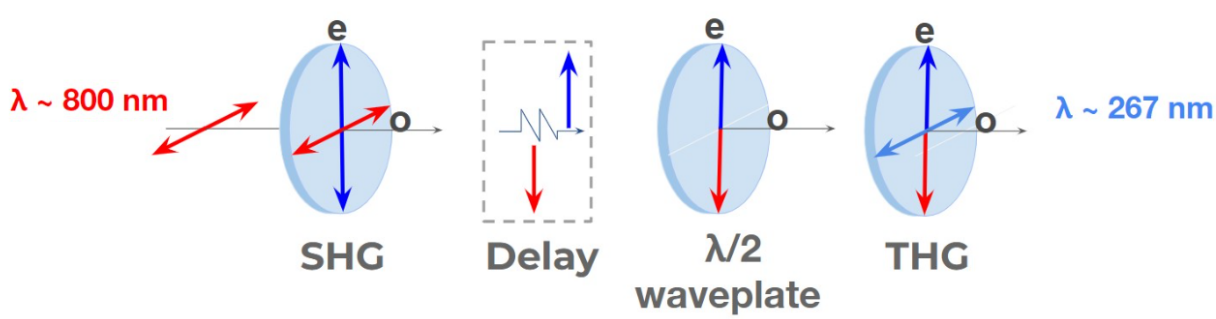

Figure 4.1: Schematic of third harmonic generation (THG). The fundamental frequency is sent into a crystal cut to generate the second harmonic (SHG) after which the two beams are temporally and spatially overlapped with a half-wave plate and a delay line before reaching the crystal cut for third harmonic generation.

This chapter begins with second harmonic generation (SHG), followed by polarization difference and group velocity dispersion compensation, and finally discusses results of sum-frequency generation (SFG) of the first and second harmonic to form the third harmonic. Throughout the chapter, the final sum-frequency generation step is referred to as third harmonic generation (THG), and the crystal which mediates this step the THG crystal. Bandwidth, and pulse length dependence, as well as the effect of nonlinear effects such as self-phase modulation, are discussed.

4.1.1 Second Harmonic Generation

Equations that describe the evolution of light as it propagates through nonlinear optical media can be approximated by taking series solutions to the nonlinear wave equation. For no free charge, $\rho = 0$, or currents, $J = 0$, and assuming the the material is non-magnetic such that $B = \mu_0 H$, but allowing non-linear response to the electric field, Maxwell's equations reduce to

$$\nabla \cdot D = 0 \qquad \nabla \times E = -\mu_0 \frac{\partial H}{\partial t}$$
$$\nabla \cdot B = 0 \qquad \nabla \times H = \frac{\partial D}{\partial t}$$

Combining these equations yields the wave equation,

$$\nabla^2 E = \frac{1}{\epsilon_0 c^2} \frac{\partial^2 D}{\partial t^2} \ .$$

The nonlinear response to applied electric fields is contained within the electric flux density

$$D = \epsilon_0 E + P \ .$$

The polarization density, P, which relates electric dipole response to applied electric field, can be approximated by a series weighed by susceptibilities $\chi^{(n)}$

$$\begin{aligned} P(t) &= \epsilon_0[\chi^{(1)} E + \chi^{(2)} E^2 + \chi^{(3)} E^3 + \cdots + \chi^{(n)} E^n] \\ &= P^{(1)} + P^{(2)} + P^{(3)} + \cdots \\ &= P^{(1)} + P^{NL} \end{aligned}$$

Thus, splitting linear and nonlinear components, $D = \epsilon_0 E + P^{(1)} + P^{NL} = D^{(1)} + P^{NL}$, where $D^{(1)} = \epsilon_0 E + P^{(1)} = \epsilon_0 \epsilon^{(1)} E$, and $\epsilon^{(1)} = 1 + \chi^{(1)} = n^2$, gives the wave equation

$$\nabla^2 E - \frac{\epsilon^{(1)}}{c^2} \frac{\partial^2}{\partial t^2} E = -\frac{1}{\epsilon_0 c^2} \frac{\partial^2 P^{NL}}{\partial t^2} \ ,$$

which takes the form of a driven wave equation, where the nonlinear polarization component acts as a source term that arises from electric field induced changes in material response.

For second harmonic generation, for an input complex electric field

$$\begin{aligned} E(t) &= E(r) e^{-i\omega t} + E^*(r) e^{i\omega t} \\ P^{(2)} &= \epsilon_0 \chi^{(2)} (2|E|^2 + E^2 e^{-2i\omega t} + E^{*2} e^{2i\omega t}) = DC + P(2\omega) + c.c. \end{aligned}$$

We represent the applied fields as plane waves with slowly varying amplitude A_j

$$E_j = \frac{A_j}{2} e^{-i(k_j z - \omega_j t)} + c.c. \ ,$$

where $k_j = \omega_j n_j / c$, and j cycles through each frequency component involved. Substituting this into the wave equation, and applying the slowly varying amplitude approximation,

$$\left| \frac{d^2 A}{dz^2} \right| \ll \left| k \frac{dA}{dz} \right| \ ,$$

gives a set of coupled equations

$$\frac{\partial A_k}{\partial z} = \frac{2\pi i k_3}{\epsilon_k} \chi^{(2)}(-\omega_k; \omega_i, \omega_j) A_i A_j e^{-i(k_i + k_j - k_k)z} \ .$$

If the pump is undepleted and the system is lossless, in terms of the intensity, or magnitude of the time averaged Poynting vector, $I = 2n_i \epsilon_0 c |A|^2$, intensity for SHG is

$$I_2 = \frac{32\pi^3 \omega_2^2}{c^3} (\chi^{(2)})^2 \frac{I_1^2}{n_1^2 n_2} L^2 \mathrm{sinc}^2 \left(\frac{\Delta k L}{2} \right) \ ,$$

where I_1 and I_2 are the intensities of the first and second harmonic respectively, and $\Delta k = k_1 + k_2 - k_3 = 0$ is the phase matching condition and is a statement of momentum conservation that must hold for harmonic generation to occur. For SHG, $k_1 = k_2$. n_1 and n_2 are the indices of refraction at each wavelength, and L is the propagation distance

Only non-centrosymmetric media can support $\chi^{(2)}$ processes. A common and simple method of phase matching is to use birefringent crystals that are cut such that the index of refraction for the input field polarization and wavelength is the same as that of the output wavelength at its polarization.

Energy conservation states

$$\omega_3 = \omega_1 + \omega_2 \ ,$$

where $\omega_1 = \omega_2 = \omega$ and $\omega_3 = 2\omega$ for SHG. Together with the phase matching condition, the index of refraction is

$$n = \frac{c}{v_\phi} = \frac{ck}{\omega} \rightarrow k = \frac{n\omega}{c}$$

$$2k_1 = k_3 \rightarrow 2\frac{n_1 \omega}{c} = \frac{n_3 2\omega}{c} \rightarrow n_1(\omega) = n_3(2\omega) \ .$$

Birefringent materials such as barium borate (BBO) and potassium dideuterium phosphate (KDP) have polarization dependent refractive indices. The index of refraction with respect to incident light polarization angle is given by their index ellipsoids

$$\frac{1}{n_e^2(\theta)} = \frac{\cos^2\theta}{n_o^2(\lambda)} + \frac{\sin^2\theta}{n_e^2(\lambda)} \ ,$$

where n_o and n_e are the major and minor axes of the index ellipsoid. By selecting the appropriate cutting angle, θ, of the crystal, the birefringence of the material can compensate for dispersion, and the phase matching condition can be satisfied,

$$n_e(2\omega, \theta) = n_o(\omega) \ .$$

For BBO the index of refraction of the two axes n_0 and n_e can be approximately expressed by the Sellmeier dispersion relation [117],

$$n_o^2(\lambda) = 2.7359 + 0.01878/(\lambda^2 - 0.01822) - 0.01354l\lambda^2$$
$$n_e^2(\lambda) = 2.3753 + 0.01224/(\lambda^2 - 0.01667) - 0.01516\lambda^2 \ .$$

For second harmonic generation in BBO from $\lambda = 800$ nm, $\theta = 29.2°$, while for generation of $\lambda = 267$ nm by sum-frequency of $\lambda = 800$ nm and $\lambda = 400$ nm light, $\theta = 44.3°$. Similarly, for KDP [118],

$$n_o^2(\lambda) = 2.259276 + 0.01008956/(\lambda^2–0.012942625) + 13.00522\lambda^2/(\lambda^2–400)$$
$$n_e^2(\lambda) = 2.132668 + 0.008637494/(\lambda^2–0.012281043) + 3.2279924\lambda^2/(\lambda^2–400) \ ,$$

with $\theta = 44.9°$ for SHG, and $\theta = 67.5°$ for SFG for third harmonic generation. Both BBO and KDP are negative uniaxial crystals, meaning $n_e < n_o$, therefore the fundamental is chosen to propagate along the ordinary axis.

Phase matching can be achieved with two different polarization configurations referred to as Type I and Type II phase matching. For Type I phase matching, both incident rays are of the same polarization, while for Type II they are perpendicular to each other. Type I phase matching was chosen for SHG because the two incident photons are from the same beam. Type I phase matching was also chosen for sum-frequency generation to form the third harmonic because the resulting light exits with polarization perpendicular to the two incoming, making it easier to phase match via birefringence.

KDP crystals were chosen for this application due to its availability in large sizes. Scaled tests reported here include use of 25 mm and 75 mm diameter crystals for both SHG and SFG, however future high power configurations for ionization injection will require even larger apertures to reduce fluence and damage. BBO, which has high nonlinear index, $\chi^{(2)} = 4.6$ pm/V for BBO compared to $\chi^{(2)} = 0.78$ pm/V for KDP, is most commonly used for harmonic generation from 800 nm wavelength, but is only grown to 10-20 mm [119, 120]. Research into growing and using large lithium triborate (LBO with $\chi^{(2)} = 1.96$ pm/V) crystals for SHG from $\lambda = 800$ nm is ongoing and promising [121], although LBO does not have a configuration that satisfies THG phase matching conditions.

Optimal crystal thickness is determined by initial intensity and bandwidth. Fig. 4.2 shows a simulation of second harmonic generation through a KDP crystal. It can be seen that for initial pulse intensity of $I = 600$ GW/cm^2 and transform limited pulse length $\tau = 45$ fs ($\Delta\lambda$ =21 nm bandwidth), SHG efficiency plateaus shortly after distance L = 0.65 mm. This distance decreases with greater initial intensity. Two effects limit conversion

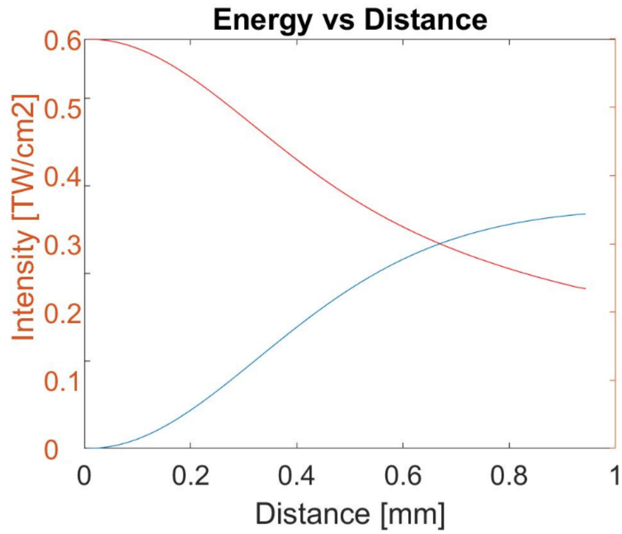

Figure 4.2: Simulated intensities of the first (red) and second (blue) harmonic as a $\lambda = 800$ nm beam with initial intensity 600 GW/cm^2 propagates through a 1 mm thick KDP crystal cut for SHG.

efficiency: (1) depletion, in which the fundamental is being depleted and conversion back to the fundamental frequency has equal probability, and (2) coherence, in which, since only one frequency is perfectly phase matched, the finite bandwidth of ultrashort pulses experience material dispersion and coherence is lost when the phase between unmatched frequency components slip by half a wavelength. A more detailed discussion of the impact of finite bandwidth will be found in section 4.1.4.

Fig. 4.3 shows measurements of SHG efficiency using a setup with 25 mm aperture optics and an input beam with diameter D = 6.7 mm diameter and pulse length $\tau = 45$ fs FWHM. The input intensity range was chosen to match intensities expected in a larger 100 TW system. Shot-to-shot input energy was monitored by calibrated camera images of leakage through a mirror just before harmonic generation. The energy of the fundamental frequency before SHG was measured with an energy meter placed just after the leakage mirror and correlated to camera readings for a wide range of energies before each set of measurements. The input pulse profile was monitored by a frequency resolved optical gating (FROG) device, discussed in more detail in Section 4.2. Resulting second harmonic energy followed the characteristic parabolic relationship $I_2 \propto I_1^2$ when the pump is undepleted. SHG efficiencies of up to 40% were recorded, matching previous studies [122].

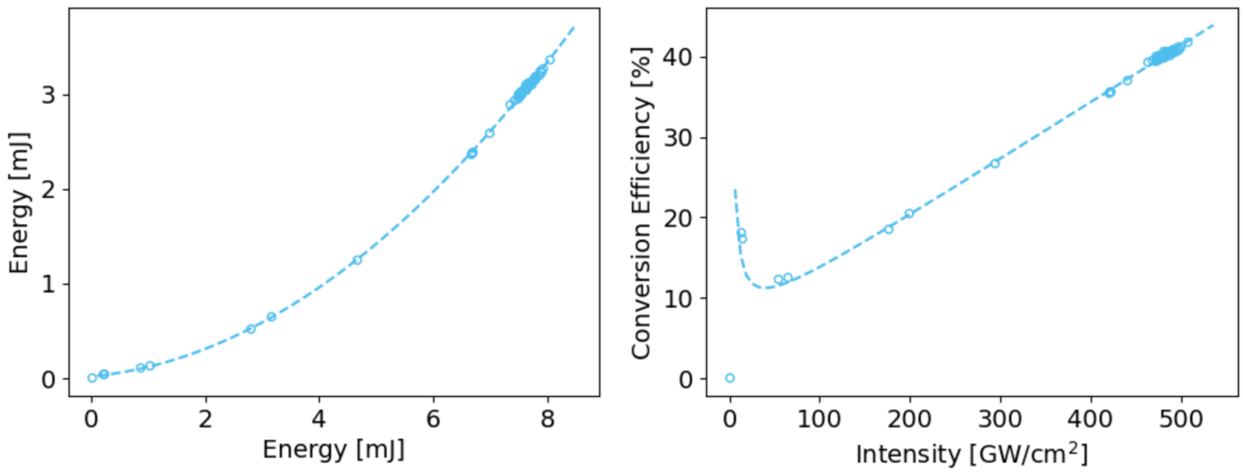

Figure 4.3: Experimentally measured energy (left) and harmonic conversion efficiency (right) of second harmonic generation using a 45 fs pulse length, 6.7 mm diameter input beam over a range of energies. The x-axis shows energy of the fundamental frequency before second harmonic generation. Values near zero when calculating efficiency suffer from low signal-to-noise and are therefore unreliable. Dashed lines are simulated values given measured pulse temporal and spatial profiles neglecting SPM.

4.1.2 Polarization Compensation

The second harmonic is generated at a polarization perpendicular to that of the fundamental. For Type I phase matching in the THG crystal, one or both of the resulting polarizations must be adjusted. This is easily accomplished by means of a half-wave plate.

The specifications of the half-wave plate are determined by its placement in a high intensity beam and in vacuum. A true zero-order half-wave plate would be required to be 69.2 μm thick for quartz, which is challenging to manufacture and handle, thus it is common to generate zero-order wave plates with two plates which combined generate a half-wave delay. Quartz is commonly used for wave plates. Sapphire crystal wave plates can also be found off-the-shelf in large apertures, though at significantly higher cost.

Since the wave plate will be placed in vacuum, conventional adhesives are not applicable, and even low out-gassing adhesives can sometimes introduce deformations in the thin material. Thus the two plates are ideally mounted with a gap that is vented so as not to trap air.

Quartz crystal is a positive uniaxial crystal, $n_e > n_o$. Its corresponding dispersion equation that gives approximate wavelength dependent index of refraction is

$$n^2 = A + \frac{B\lambda^2}{\lambda^2 - C^2} + \frac{D\lambda^2}{\lambda^2 - F} ,$$

and

$$\frac{dn}{d\lambda} = \frac{1}{n}\left[\frac{B\lambda}{\lambda^2 - C} + \frac{D\lambda}{\lambda^2 - F} - \frac{B\lambda^2}{(\lambda^2 - C)^2} - \frac{D\lambda^2}{(\lambda^2 - F)^2}\right] .$$

Table 4.1 gives the coefficients for quartz.

	Ordinary Axis	Extraordinary Axis
A	1.2860414	1.28851804
B	1.0704408	1.09509924
C	0.0100586	0.01021019
D	1.10202242	1.15662475
F	100	100

Table 4.1: Coefficients of the dispersion equation for the ordinary and extraordinary axes of the refractive index of quartz crystals [123].

Polarization rotation by use of transmissive optics are convenient, compact and easy to align compared to polarization rotation by reflective optics. However, in short-pulse applications, their use can introduce contributions to unwanted intensity dependent nonlinear effects such as self-phase modulation. In addition, for harmonic generation, group velocity dispersion in the crystal will result in lengthening of pulses as well as temporal separation between the fundamental and second harmonic before they reach the SFG stage.

The group velocity of each wavelength in terms of the index of refraction is

$$v_g = v_p(1 + \frac{\lambda}{n}\frac{dn}{d\lambda}) ,$$

For example, after traversing 1 mm of quartz crystal, 222 fs of delay between $\lambda = 800$ nm and $\lambda = 400$ nm is introduced. Since the two colors both have $\sim$ 40 fs pulse durations, the two colors would emerge temporally separated upon entering the third harmonic crystal unless this temporal separation is pre-compensated. This study explored two methods of group velocity dispersion compensation.

4.1.3 Group Velocity Dispersion Compensation

The first and second harmonic have different group velocities due to material dispersion. First order dispersion can be compensated for by appropriate crystal orientation, however after passing through further dispersive elements, such as a half-wave plate, the differing group velocities lead to the fundamental outrunning the second harmonic such that the two colors no longer overlap for sum-frequency generation in the third harmonic crystal. Two methods of group velocity dispersion compensation were compared - compensation via a negative dispersion uniaxial optic and compensation in vacuum via path length separation and recombination of the two harmonics [124, 125].

Negative Dispersive Element

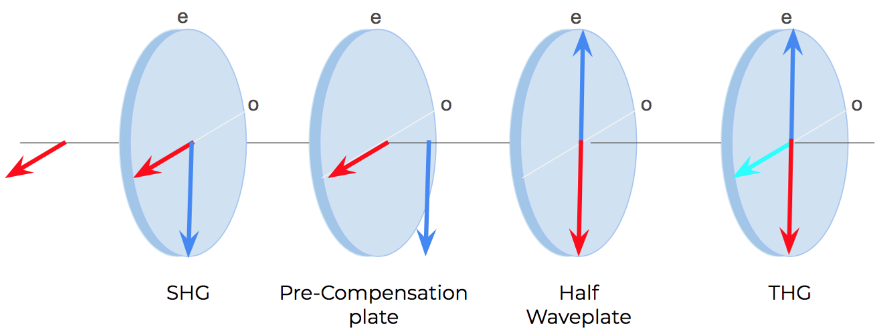

Figure 4.4: Schematic of in-line group velocity walk-off compensation that uses a negative uniaxial crystal as a pre-compensation plate that can be tilted for adjustable delay between the fundamental and second harmonic.

Fig 4.4 shows a configuration that is simple, easy to align and, for small beam sizes, off-the-shelf. The wave plate introduces a half wave delay for $\lambda = 800$ nm and a full wave for $\lambda = 400$ nm so that the two polarizations are overlapped before entering the third harmonic generation crystal. In this configuration, temporal overlap is achieved by using a thick transmissive negative uniaxial crystal ($n_e < n_0$), to pre-compensate the positive dispersion introduced by the wave plate. Unlike the crystal used for harmonic generation, this crystal is cut along its maximum birefringence, $\theta = 90°$. BBO, which has large birefringence is commonly used for this purpose. Another option is calcite, which has larger birefringence, but the damage threshold is lower than for BBO.

For this configuration, compensating for group velocity delay before polarization overlap allows for utilization of the polarization difference between two harmonics. The compensation plate is oriented so that the optical axis is along the polarization of the fundamental. The second harmonic oriented along the extraordinary axis experiences a lower refractive index than the fundamental. By tilting the compensation plate to introduce more path length, the time delay can be adjusted. Both path length and index of refraction change with angle of incidence.

Delay Line

A more conventional method for controlling group velocity delay between the two harmonics is to separate the fundamental and second harmonic using dichroics, and, using reflective optics, introduce a path length difference in vacuum that temporally overlaps the two in the third harmonic crystal. A schematic is shown in Fig. 4.5. Polarization adjustment is achieved by inserting a wave plate in the arm containing only the fundamental. The fundamental transmits through the dichroics as well as the wave plate for two reasons. The first reason is because reflection and transmission of the dichroics is achieved by appropriate coating that creates constructive interference for the reflected beam for one of the wavelengths. Since the two colors are harmonics of each other, it is difficult to satisfy a constructive interference condition for the longer wavelength without also satisfying the condition for the shorter. Thus, it is easier and more efficient to reflect the shorter wavelength. The second reason to preferentially send the fundamental through transmissive optics is that wavefront distortion from self-phase modulation is wavelength dependent and is greater for shorter wavelengths.

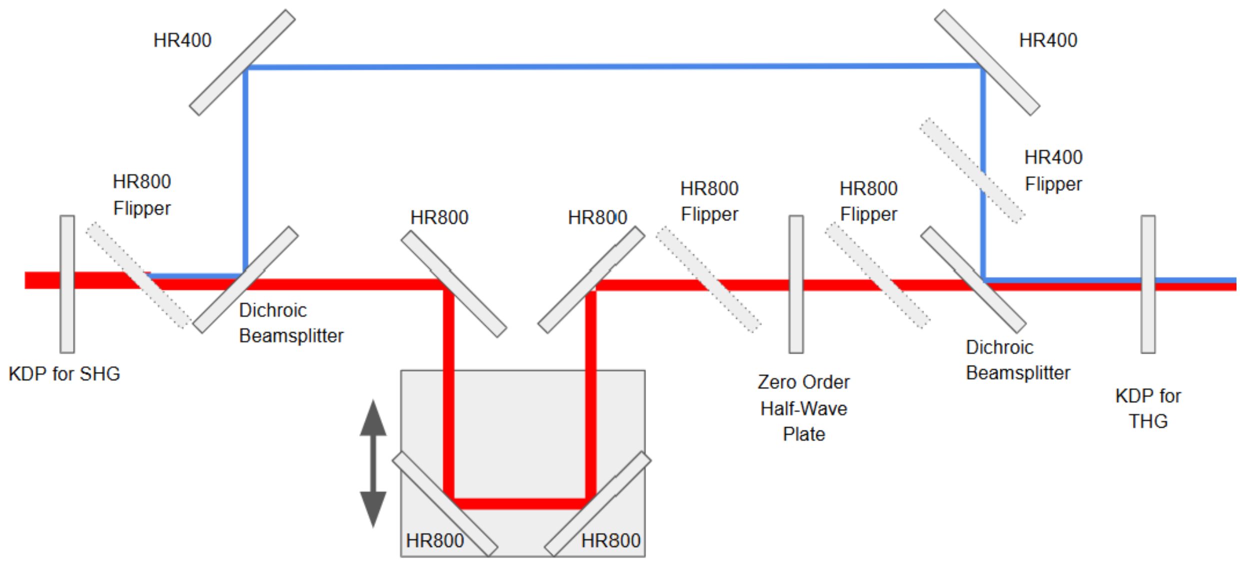

Figure 4.5: Schematic of third harmonic generation (THG) using a delay line. The second harmonic is separated from the fundamental using a dichroic mirror, after which the two path lengths can be separately adjusted to pre-compensate walk-off from group velocity dispersion of the two colors in the transmissive optics.

Scaled down experiments using both delay plate and delay line configurations were performed for comparison. α-BBO, with six times greater nonlinear index than KDP was chosen for the pre-compensation plate to test the effect of introducing the minimum material thickness. Were this inline option viable, large aperture KDP would be required to be six times thicker than that of the α-BBO tested. The delay line layout includes mostly reflective optics, however, the first and second harmonic are separated and recombined with dichroics, both of which the fundamental must traverse. Dichroics in both scaled down and full scale experiments were chosen to be 4 mm thick in order to minimize path length in the optics while considering machinability at large apertures.

The resulting third harmonic conversion efficiencies are plotted in Fig. 4.6. The transmissive solution, which employed a compensation plate, resulted in asymptotic growth in efficiency with intensity, while the reflective solution resulted in efficiencies that closely matched results simulated with no self-phase modulation to higher intensities. In addition, energy variation is greater than SHG due to the nonlinear dependence of THG on intensity fluctuations of both the first and second harmonic and of SPM. Greater energy fluctuation above 400 GW/cm^2 in Fig. 4.6 were due to energy meter limits. At a fluence of 18.2 mJ/cm^2, with 40 fs pulse length, 15.6% conversion efficiency to the third harmonic was obtained using the reflective solution.

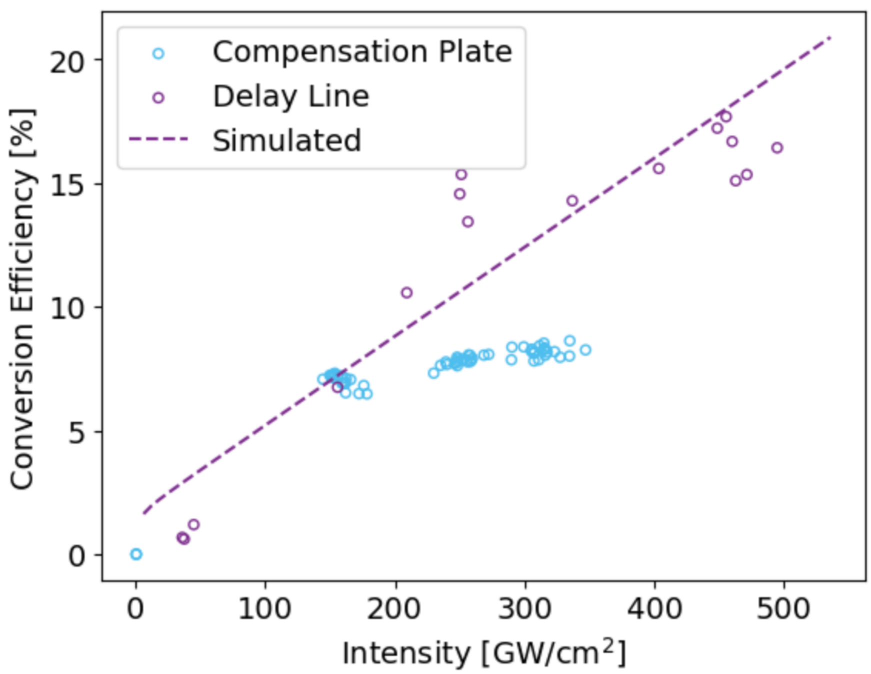

Figure 4.6: Third harmonic conversion efficiency using two methods to compensate for group velocity walk-off between the first and second harmonic, a negative uniaxial crystal (blue) and a delay line (purple). The x-axis shows the intensity of the fundamental frequency before SHG, derived from measured energies and pulse length. The dotted line shows simulated expected values that neglect SPM.

Measurements of spectra found that divergence of the two plots occurred at the onset of self-phase modulation (SPM) as seen in Fig. 4.7. Severe modulation of the spectrum resulted in bandwidth increase as energy collected in side lobes, leading to decrease in maximum intensity and decrease in harmonic generation efficiency compared to that simulated.

SPM derives from a third order nonlinearity and becomes relevant when intensities reach $\sim 10^{15}$ W/cm^2 and above. For electric field $E(t) = E_0 \cos \omega t$, third order polarization density is

$$P^{(3)}(t) = \frac{1}{4}\epsilon_0 \chi^{(3)} E_0^3 \cos 3\omega + \frac{3}{4}\epsilon_0 \chi^{(3)} E_0^3 \cos \omega \ .$$

The first term is third harmonic generation. The second term, at the input frequency, contributes to the nonlinear refractive index

$$n = n_0 + n_2 I \ ,$$

with

$$n_2 = \frac{3}{2n_0^2\epsilon_0 c}\chi^{(3)} \ .$$

For fused silica, $n_2 = 3.5 \times 10^{-20}$ $\mathrm{m^2/W}$ at $\lambda = 800$ nm, where $\chi^{(3)} = 2.5 \times 10^{-22}$ $\mathrm{m^2/V^2}$. The nonlinear index of refraction introduces an intensity dependent phase and thus frequency composition,

$$\omega(t) = \frac{d\phi}{dt} = \frac{d}{dt}(\omega_0 t - k_0 n z) = \omega_0 - k_0\frac{dn}{dt}z = \omega_0 - k_0 n_2 z\frac{dI}{dt} \ .$$

For a Gaussian temporal pulse shape,

$$I = I_0 \exp\frac{-t^2}{\tau_0^2} \ ,$$

The frequency is

$$\omega(t) = \omega_0 + 2zk_0n_2\frac{2t}{\tau_0^2}I = \omega_0 + 2zk_0n_2\frac{2t}{\tau_0^2}I_0\exp\frac{-t^2}{\tau_0^2} \ .$$

From this relation it can be seen that, symmetric about ω_0, higher frequencies increase and lower ones decrease, and that, since the shift is proportional to intensity, the result of this effect is redistribution of energy away from high intensity regions of the spectrum. The side lobes in the spectrum in Fig. 4.7 are characteristic of the onset of SPM.

In summary, although highly compact designs can be purchased off-the-shelf that use a negative uniaxial crystal to pre-compensate for group velocity walk-off [126], these designs could not be applied to high intensity THG. Two reasons made this option unsuitable for high intensity sources. The first is that, as mentioned above, BBO crystals, which have high nonlinear index, are not available in large sizes. More important, however, is that at high intensities, self-phase modulation is a limiting factor to harmonic conversion efficiency.

4.1.4 Third Harmonic Generation

Generation of the third harmonic is accomplished by sum-frequency of the fundamental and second harmonic.

$$3\omega = \omega + 2\omega \ .$$

For an electric field,

$$E(t) = E_1 e^{-i\omega_1 t} + E_2 e^{i\omega_2 t} + cc \ ,$$

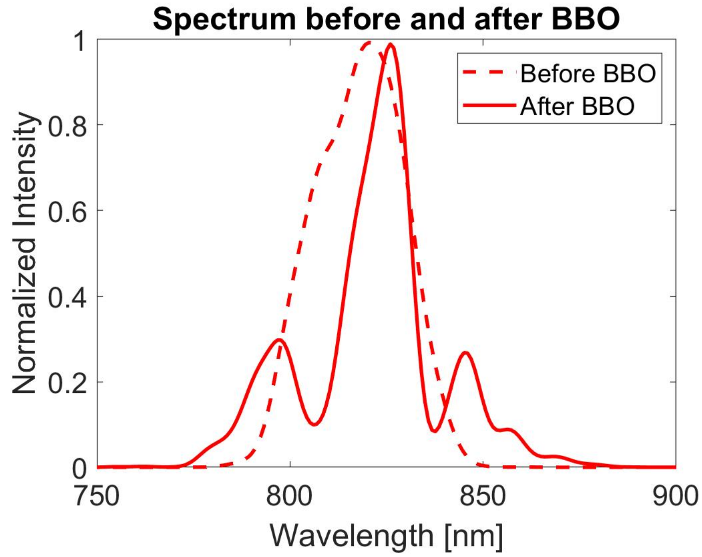

Figure 4.7: Spectra of the fundamental before and after group velocity delay compensation via delay plate. The dotted line shows the spectrum of the original pulse. The solid line shows the additional modulation after propagation through a 2.5 mm thick BBO crystal cut to introduce maximum negative group velocity dispersion.

the second order portion of the nonlinear polarization density is

$$\begin{aligned} P^{(2)} =& \epsilon_0 \chi^{(2)} [E_1^2 e^{-2i\omega_1 t} + E_1^2 e^{-2i\omega_2 t} \\ & + 2(E_1 E_2 e^{-i(\omega_1+\omega_2)t} + E_1 E_2^* e^{-i(\omega_1-\omega_2)t}) \\ & + |E_1|^2 + |E_2|^2] + cc \\ & = SHG + SFG + DFG + DC \end{aligned}$$

where SHG stands for second harmonic generation, SFG for sum-frequency generation, DFG for difference-frequency generation, and DC is an optical rectification component. The process that dominates depends on the input intensity and phase matching, which, for example, can be accomplished by proper selection of birefringent crystal.

For sum-frequency generation,

$$I_3 = \frac{2\omega_3^2}{\epsilon_0 c^2} (\chi^{(2)})^2 \frac{I_1 I_2}{n_1 n_2 n_3} L^2 \mathrm{sinc}^2(\frac{\Delta k L}{2}) \ .$$

Fig. 4.8 shows the intensity of the first, second, and third harmonics as they proceed through the third harmonic crystal. If the first harmonic is timed to precede the second harmonic pulse by half a pulse width as they enter the crystal, maximum third harmonic generation occurs at a propagation distance of $L \sim 0.5$ mm. This determines when the third

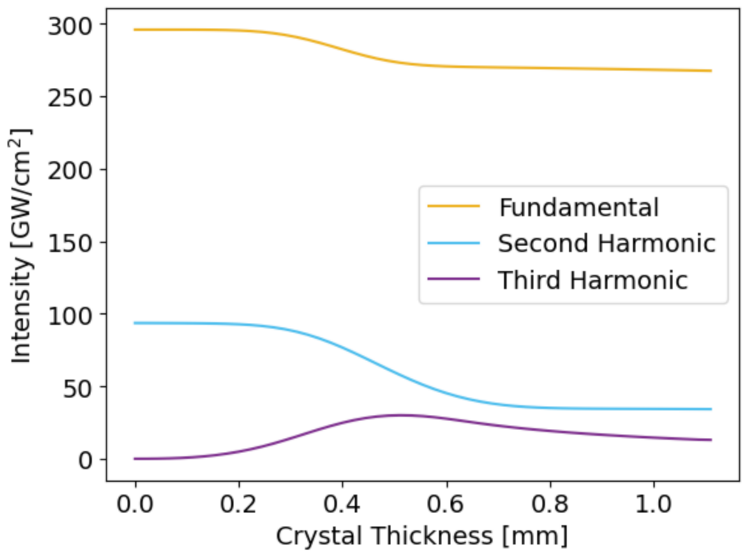

Figure 4.8: Simulation of intensity of the first, second, and third harmonic during propagation through the third harmonic crystal.

harmonic should be extracted from the crystal and therefore the optimal crystal thickness. However, since the path lengths of the first and second harmonic are adjustable, the two harmonics can be made to overlap near the exit of the crystal for optimal third harmonic extraction.

Fig. 4.9 shows a snapshot of a simulation of harmonic generation in the third harmonic generation crystal. The first and second harmonic are not simultaneously phase matched and sweep past each other at differing velocities during their propagation through the crystal. Third harmonic generation, thereby, results from a convolution of the two, resulting in a longer pulse length than either of the first or second.

Harmonic generation at a range of energies, pulse lengths, temporal chirps and crystal thicknesses was explored on a scaled down setup using 25 mm aperture optics and results compared with simulation. Energy converted to second and third harmonic for optimized conditions presented in Fig. 4.3 and Fig. 4.10 show harmonic generation with a 6.7 mm diameter, 45 fs, 810 nm wavelength centered beam. Group velocity delay was compensated via delay line. SHG crystal thickness was 0.64 mm and THG crystal thickness was 0.44 mm. The horizontal axis shows input energy (left) and corresponding intensity (right), and the vertical axis shows the resulting second and third harmonic energy (left) and conversion efficiency (right). Spatial and temporal profile as well as energy of the fundamental were monitored shot-to-shot via low energy leakage through mirrors directing the beam into the second harmonic crystal. Spatial profile was measured on a CCD camera that was energy calibrated before each experiment, and temporal profiles were measured by a GRENOUILLE. Dotted lines show simulation results given measured input spatial and temporal profiles.

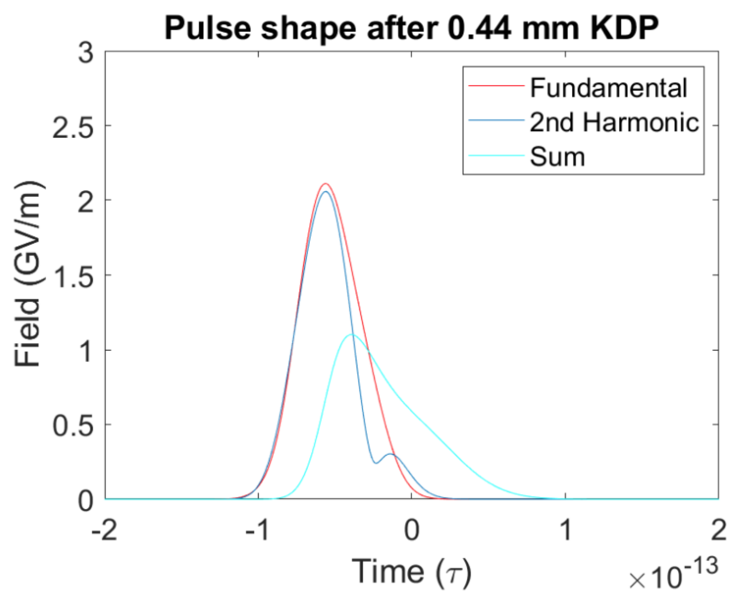

Figure 4.9: Simulated pulse profiles of the first, second, and third harmonic. The first and second harmonic sweep past each other in the third harmonic crystal. As a result, the third harmonic pulse forms as a convolution of the first and second harmonic and therefore emerges with a longer pulse width than the two input pulses.

A one-dimensional nonlinear optics propagation code that stepwise solves the nonlinear Schrödinger equation using the split-step algorithm [127, 128, 129] was written and used to explore expected efficiencies given a variety of parameters. The code was extended to take predetermined functions as well as calibrated camera images and electric field arrays retrieved by FROG measurements as input.

An experimental setup for third harmonic generation at the 100 TW scale was built and tested in preparation for two-color ionization injection. A schematic is shown in Fig. 4.11. Four inch diameter mirrors and three inch diameter harmonic generation crystals were used to accommodate a D = 22 mm FWHM laser beam. Fundamental frequency energy was varied from 1 mJ to 250 mJ. Dichroic mirrors were 4 mm thick, matching that of the 1 inch diameter setup. Harmonic generation crystals were increased to 1 mm thickness for machinability at large aperture at the cost of lower SHG efficiency. Fig. 4.12 shows energy conversion efficiency at high power using τ =33 fs pulses. Maximum third harmonic energy conversion efficiency was 9%. Although much more energy was converted to the third harmonic than in the 15 TW system, conversion efficiency was lower. Three primary effects limited efficiency. The first is that of SPM, the onset of which results in asymptotic conversion efficiency that was seen in considering group velocity dispersion compensation via a thick negative dispersive plate. The second is pulse lengthening of the fundamental due to dispersion in the dichroics

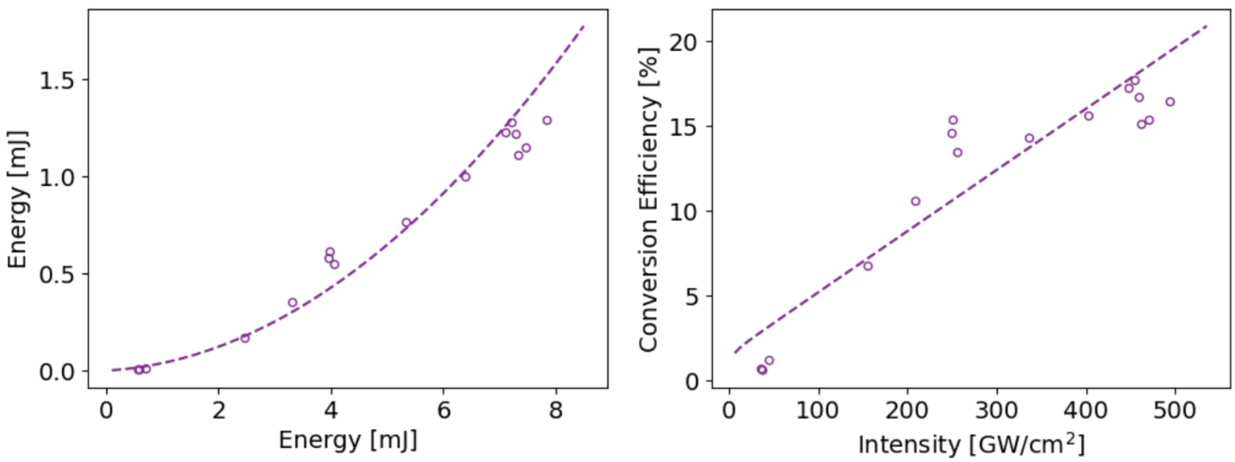

Figure 4.10: Measured energy (left) and harmonic conversion efficiency (right) of third harmonic generation using a 45 fs pulse length, 6.7 mm diameter beam with group velocity delay compensated by the delay line. The x-axis shows energy of the fundamental before SHG. Dashed lines are simulated values given measured shot-to-shot spatial profiles and pre-measured pulse profile.

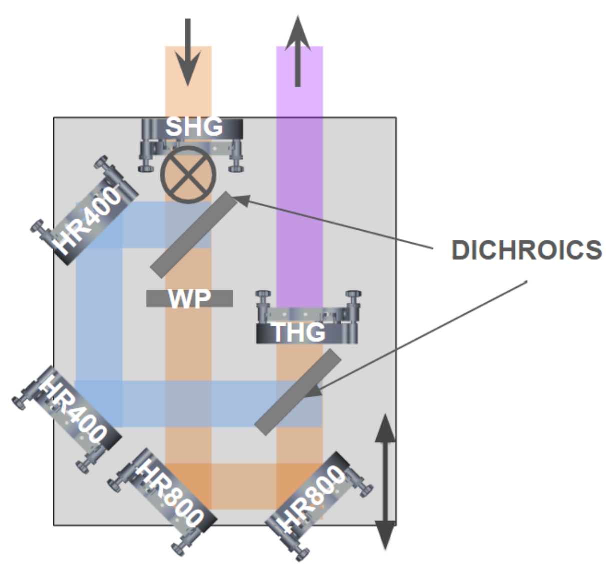

Figure 4.11: Schematic of third harmonic generation at the 100 TW scale. Reflective optics have 101 mm diameters and transmissive crystals, the SHG crystal, half-wave plate (WP) and THG crystal, have 75 mm diameters. The input beam diameter is 22 mm FWHM.

and wave plate leading to lower intensity for THG. A 33 fs pulse becomes 49 fs after 12 mm of fused silica, dropping 33% in intensity. In the same configuration, a 45 fs pulse becomes 52 fs long, reducing intensity by 14%. The third effect is that of limited supported bandwidth.

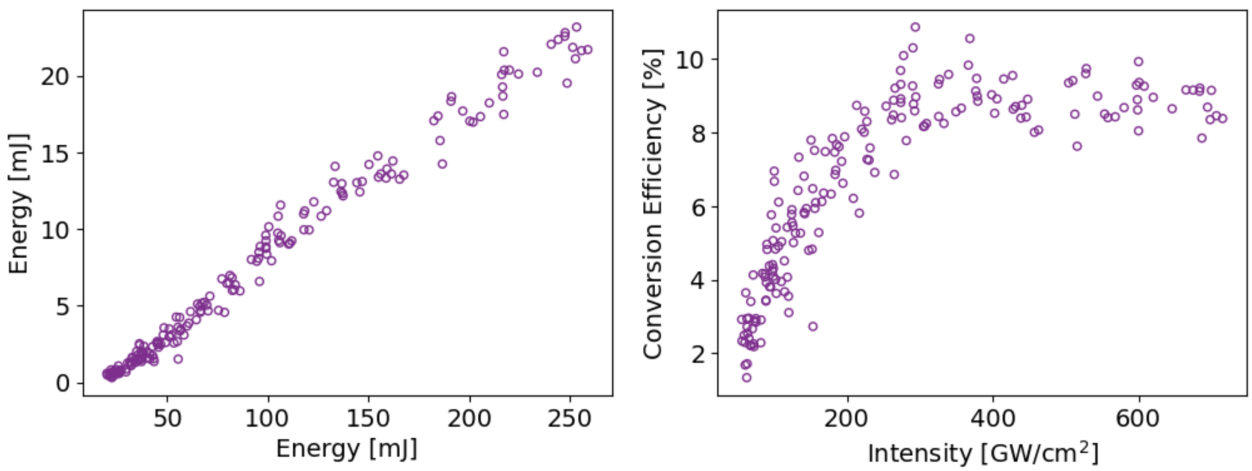

Figure 4.12: Energy conversion efficiency at high power using a 33 fs pulse length, 31 nm bandwidth, 22 mm FWHM diameter beam. Its energy and calculated intensity before SHG are shown on the x-axes.

Bandwidth Effects

For a dispersive material, we represent each frequency component separately, assuming series representations $E(r,t) = \sum_n E_n(r,t)$ and $P^{NL} = \sum_n P_n^{NL}$, where

$$E_n(r,t) = E(\omega_n)e^{-i\omega t} = A_n(\omega_n)e^{i(k_n \cdot r - \omega_n t)} \ ,$$

and A_n is a spatially slowly varying field amplitude. The wave equation for each frequency component becomes

$$\nabla^2 E_n - \frac{\epsilon^{(1)}(\omega_n)}{c^2}\frac{\partial^2}{\partial t^2}E_n = -\frac{1}{\epsilon_0 c^2}\frac{\partial^2 P_n^{NL}}{\partial t^2} \ .$$

In one dimension, solutions to each frequency component will be similar as those for a single wavelength,

$$I_3 = \frac{2\omega_3^2}{\epsilon_0 c^2}(\chi^{(2)})^2 \frac{I_1 I_2}{n_1 n_2 n_3} L^2 \mathrm{sinc}^2(\frac{\Delta k L}{2}) \propto \frac{L^2}{\lambda^2}\mathrm{sinc}^2(\frac{\Delta k L}{2}) \ .$$

However, perfect phase matching, $\Delta k(\lambda) = k_1 + k_2 - k_3$, only occurs for the design wavelength, λ_0 for which $\Delta k = 0$ and $\mathrm{sinc}^2(\frac{\Delta k L}{2}) = 1$. This condition sets the supported bandwidth that is frequency converted. For wavelength $\lambda = \lambda_0 + \delta\lambda$ in SHG,

$$\Delta k(\lambda) = 2k_1 - k_3 = 2\frac{2\pi n(\lambda)}{\lambda} - \frac{2\pi n(\lambda/2)}{\lambda/2} = \frac{4\pi}{\lambda}[n(\lambda) - n(\lambda/2)] \tag{4.1}$$

$$= \frac{4\pi}{\lambda_0}[1 - \frac{\delta\lambda}{\lambda_0}][n(\lambda_0) + \delta\lambda\frac{dn(\lambda_0)}{d\lambda} - n(\lambda_0/2) + \frac{\delta\lambda}{2}\frac{dn(\lambda_0/2)}{d\lambda}] \tag{4.2}$$

$$= \frac{4\pi\delta\lambda}{\lambda_0}\left[n'(\lambda_0) - \frac{1}{2}n'(\lambda_0/2)\right] \tag{4.3}$$

to first order in $\delta\lambda$. Here $n'(\lambda_0) = \frac{n(\lambda_0)}{d\lambda}$, and it was assumed that phase matching is satisfied at λ_0 such that $n(\lambda_0) = n(\lambda_0/2)$.

The sinc^2 function drops to half at $\Delta kL/2 = \pm 1.39$, or $|\Delta k| < 2.78L$, setting the bandwidth of the second harmonic to

$$\Delta\lambda_{FWHM-SHG} = \frac{0.44\lambda_0/L}{n'(\lambda_0) - \frac{1}{2}n'(\lambda_0/2)} \ .$$

For a KDP crystal length of $L = 1$ mm, SHG bandwidth is $\Delta\lambda$ =12 nm, corresponding to a transform limited pulse length $\Delta\tau_{FWHM} = 45$ fs. For crystal length $L = 0.6$ mm, the maximum supported SHG bandwidth is $\Delta\lambda = 19$ nm with transform limited pulse length $\Delta\tau_{FWHM} = 29$ fs.

Following the same process for SFG,

$$\Delta k(\lambda) = \frac{2\pi\delta\lambda}{\lambda_0}\left[n'(\lambda_0) + \frac{1}{2}n'(\lambda_0/2) - \frac{1}{3}n'(\lambda_0/3)\right] \ ,$$

and

$$\Delta\lambda_{FWHM-SFG} = \frac{0.88\lambda_0/L}{n'(\lambda_0) + \frac{1}{2}n'(\lambda_0/2) - \frac{1}{3}n'(\lambda_0/3)} \ .$$

In SHG the propagation length over which phase matching occurs is the entire crystal length $L = L_{crystal}$. In SFG however, since pulse overlap timing is adjustable, L is determined by the interaction length, maximized for L$\approx$ 0.34 mm, and results in a bandwidth of $\Delta\lambda = 5$ nm and $\Delta\tau_{FWHM} = 44$ fs. Previous theoretical and experimental studies using $\lambda = 1053$ nm lasers have shown that the bandwidth for highest harmonic conversion efficiency was 10 - 17 nm [130, 131].

Fig. 4.13 shows measurements of SHG and THG efficiency as a function of crystal thickness. The second harmonic conversion efficiency is greater for longer propagation distances, while for THG, conversion efficiencies are unchanged by crystal thickness because the overlap distance is controlled by group velocity dispersion compensation, which can be tuned such that third harmonic exits the crystal at its peak amplitude.

Fig. 4.14 shows simulations of SHG using alternately $\tau = 33$ fs and $\tau = 45$ fs bandwidth limited pulses through $L = 0.65$ mm and $L = 1$ mm thick KDP crystals. The greatest efficiency is gained for shorter bandwidth (longer pulse) and longer propagation length pulses.

However, it can also be seen from $\tau = 33$ fs pulses propagating through $L = 0.65$ mm and $L =$ 1 mm crystals, that conversion efficiencies nearly overlap because loss due to unsupported bandwidth outweigh the efficiency gained from greater propagation distance through the crystal.

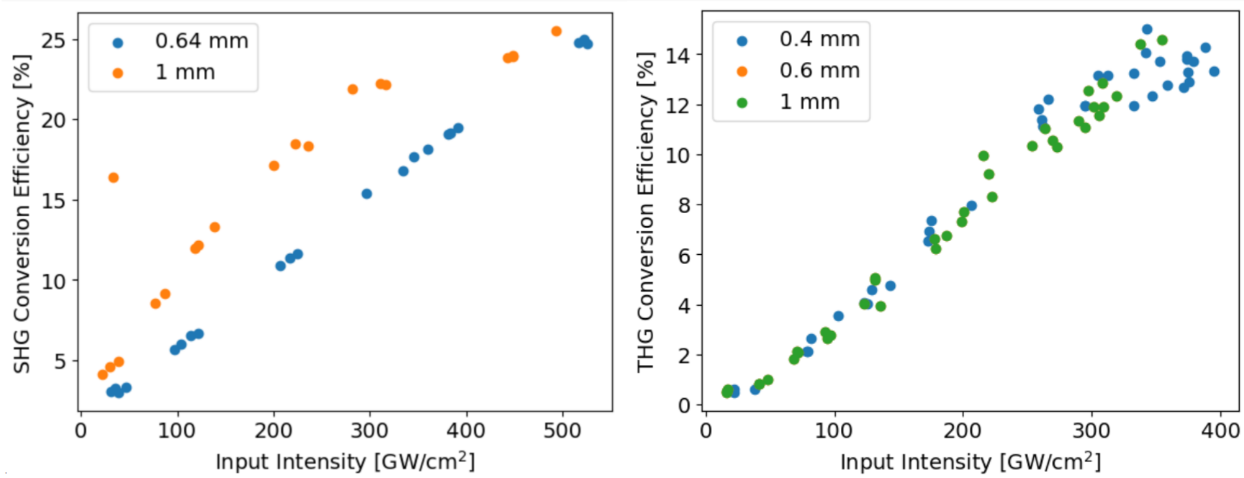

Figure 4.13: SHG (left) and THG (right) efficiency as a function of crystal thickness. THG measurements were made using 0.64 mm thick SHG crystals. For both, the initial pulse length of the fundamental is $\tau = 45$ fs.

4.2 Pulse Length Measurement

The electric field of femtosecond scale near infrared lasers are commonly measured with commercially available devices that use frequency resolved optical gating (FROG) [132][133] but no such device exists commercially to measure pulses in the ultraviolet. Therefore, in order to measure the third harmonic pulse length, a frequency resolved optical gated diagnostic that uses self-diffraction was built for this study.

Frequency Resolved Optical Gating

The increased use and thus creation of ultrashort laser pulses has necessitated precise methods of characterizing these pulses. Autocorrelators using second harmonic generation were one of the first pulse length measurement devices, but the pulse length could only be derived using an assumed pulse shape, usually Gaussian, top-hat or super-Gaussian. As higher intensity pulses, with their included nonlinearities, become less Gaussian distributed in both space and time, these assumptions become inaccurate. Ambiguities in pulse length and

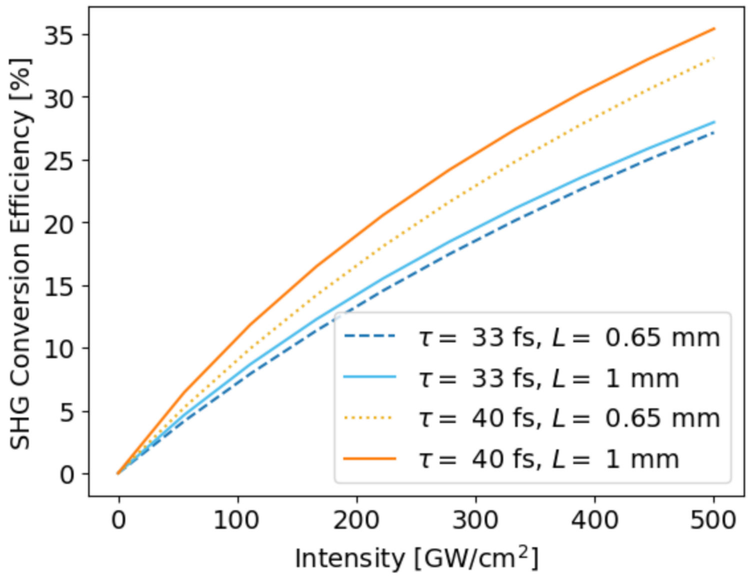

Figure 4.14: Simulation showing SHG conversion efficiency for two crystal thicknesses at two different input bandwidths.

pulse shape existed until the invention of the frequency resolved autocorrelator that today is known as frequency resolved optical gating.

Ultrafast pulses have pulse lengths on the order of 30 fs. This means that if one were to capture this pulse with a camera, the camera must film at over 100 trillion frames per second. No camera currently achieves that. In fact, often the shortest time length available in the laser lab is the pulse itself. The idea of using the pulse to measure itself is the concept of the autocorrelator. The autocorrelator works by splitting the pulse into two pulses of similar intensity and intersecting them in space and time at a small angle in a nonlinear crystal that is often cut for SHG. When the two pulses coincide in the crystal, a distinct signal pulse appears. If one pulse is swept in time, the measured intensity curve of the signal is a convolution of the pulse with itself, from which information about the pulse can be inferred. Effectively the pulse is used to optically gate itself. A basic layout of an autocorrelator using SHG can be seen in Fig. 4.15 and Fig. 4.16.

The signal given from an autocorrelator is

$$A(\tau) = \int_{-\infty}^{\infty} I(t)I(t-\tau)dt \ .$$

Kane and Trebino made a very important improvement to the autocorrelator [132]. The autocorrelator gives information about the pulse intensity, but not phase, within which the characteristics of pulse evolution, such as phase velocity, group velocity, second order dispersion etc., are encoded. By measuring not only the intensity but also the spectrum of

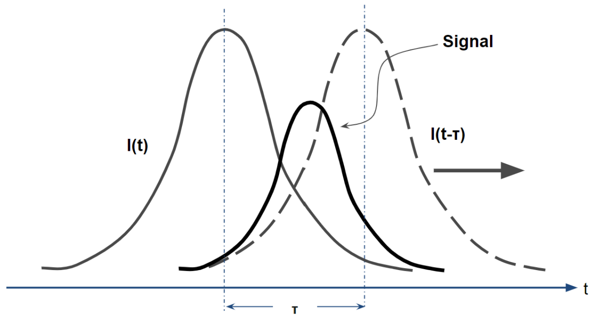

Figure 4.15: Diagram of autocorrelation. One copy of the pulse is swept in time past the other. The signal is the convolution of the two copies of the pulse.

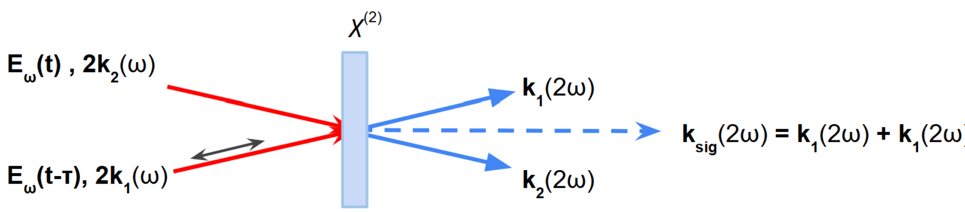

Figure 4.16: Schematic of autocorrelation using second harmonic generation. The original pulse is separated into two, one with fixed path length and another with adjustable path length. When the two are passed through a BBO crystal, they each generate the second harmonic. When temporally overlapped, a third signal pulse is generated. Measuring the spectrum of this signal pulse as a function of delay gives a delay vs. wavelength trace that can be used to retrieve the full electric field of the original pulse.

the generated signal as a function of relative delay, the entire electric field amplitude and phase could be deduced uniquely without prior assumptions.

The measured spectrum over time gives a two dimensional intensity plot called a spectrograph:

$$I(\omega, \tau) = \left| \int_{-\infty}^{\infty} E(t)g(t-\tau)exp(-i\omega t)dt \right|^2 ,$$

where the electric field is

$$E(t) = Re\{\sqrt{I(t)}\exp(i\omega_0 t - i\phi(t))\} .$$

Here, ω_0 is the carrier frequency and $I(t)$ and $\phi(t)$ are the time-dependent intensity and phase of the pulse.

In the case that the gate is the pulse itself then

$$I(\omega,\tau)^{SHG}_{FROG} = \left| \int_{-\infty}^{\infty} E(t)E(t-\tau)exp(-i\omega t)dt \right|^2 .$$

Pulse measurement by autocorrelation is dependent on a nonlinear process. Namely it depends on the creation of a signal that exists only when the two pulses overlap and interact, mediated by the crystal.

In an autocorrelator that uses SHG as its nonlinear process, each of the two input beams generate the second harmonic in the crystal. When the two beams coincide in time in the crystal, a new signal with wavevector $\vec{k}_{sig}$ appears that is the sum of the two exiting wavevectors

$$\vec{k}_{sig} = \vec{k_1} + \vec{k_2} .$$

Conveniently, the generated signal is separated in direction from those of the input pulses, as shown in Fig. 4.16.

FROG for ultraviolet pulses

For a UV pulse, SHG cannot be conveniently used since SHG would generate a deep UV pulse that is even more difficult to measure, and no harmonic generation crystal that is both able to phase match and transparent to that wavelength exists. However, the concept of frequency resolved optical gating can use any nonlinear process that produces a unique signal. Of the FROG configurations [133] appropriate for UV are the transient grating (TG FROG) and the self-diffraction FROG (SD FROG) devices that use a third order nonlinearity that generates the same frequency output as its input [134][135]. Centrosymmetric crystals such as fused silica can be used for this purpose. In a TG FROG, three copies of the pulse are made, two of which are made to interfere in the crystal. At high enough intensity, the interference pattern induces a periodic structure in the index of refraction that acts as a diffraction grating (breaking symmetry) off of which the third pulse is diffracted. In this case the grating is used as the optical gate. The self-diffraction FROG works in a similar way but uses only two copies of the pulse that are used to both create the diffraction grating and be diffracted by it. The output beams exit with wave vectors

$$\vec{k}_{sig1} = 2\vec{k_1} - \vec{k_2} \text{ and } \vec{k}_{sig2} = 2\vec{k_2} - \vec{k_1} ,$$

and intensity

$$I(\omega,\tau)^{SD}_{FROG} = \left| \int_{-\infty}^{\infty} E^2(t)E^*(t-\tau)exp(-i\omega t)dt \right|^2 .$$

Fig. 4.17 shows a schematic of the nonlinear interaction used in the self-diffraction FROG. The input beam is split into two, one arm has variable delay and the two are overlapped in fused silica. The front of the pulse generates a diffraction pattern that induces a nonlinear index of refraction grating. Subsequent portions of the beam continue to induce this grating

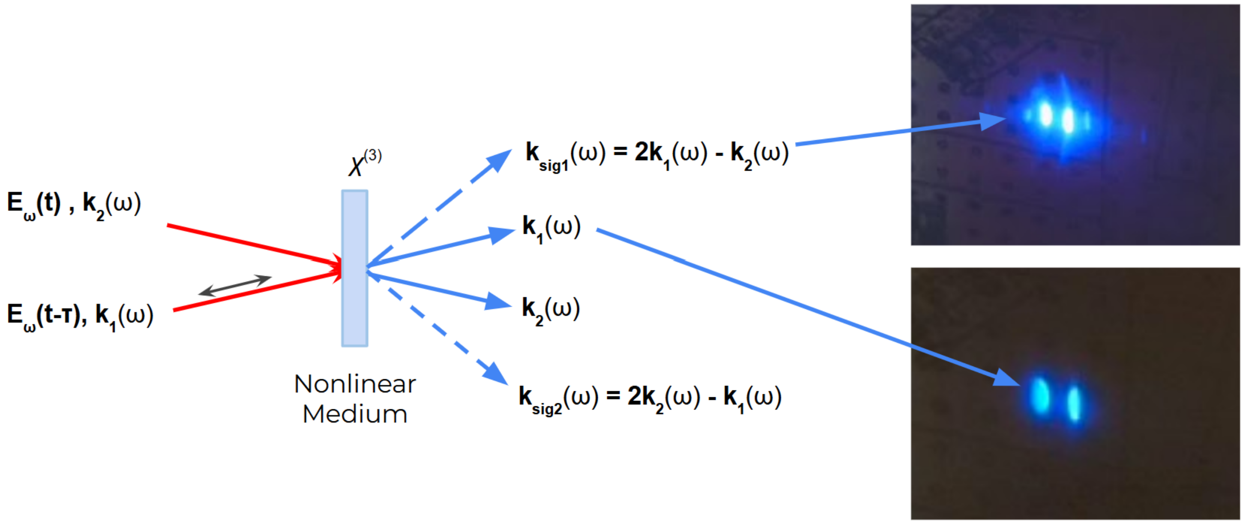

Figure 4.17: Schematic of a self-diffraction FROG (left). The pulse whose pulse length is to be measured is split into two, one of which has adjustable path length, and focused onto a 2 mm thick fused silica plate. When the two pulses are not temporally overlapped, two pulses are detected after the fused silica plate (bottom right). When they are overlapped, they form a index of refraction diffraction grating and two signal pulses appear on either side of the original two (top right). These are the two pulses diffracted by the induced diffraction grating. Measuring either pulse as a function of delay of the adjustable pulse gives an intensity vs. wavelength trace that can be used to retrieve pulse properties such as pulse length and second and third order phase properties.

as well as diffract off of it. The two images to the right of the schematic are images of the outputs scattered off of a paper card. The lower right image shows when the two beams are not temporally overlapped. The upper right shows that when the two beams are spatially and temporally overlapped in the crystal, two distinct signals appear. Spectrally resolving the signal as a function of gate delay, effectively the path length of one variable arm, gives a time vs. frequency (or wavelength) trace, as shown in Fig. 4.18, that can be used to derive the full electric field of the original pulse.

A self-diffraction FROG device to measure pulse length in the ultraviolet was built for this study. Pulse lengths of the fundamental were measured by frequency resolved optical gating (FROG) (Swamp Optics GRENOUILLE). A schematic layout of the device is presented in Fig. 4.19. The UV pulse generated by THG is separated into three collinear beams by means of a custom iris. One of these beams has adjustable path length before all three are focused by an OAP onto a thin fused silica plate. In this way the diagnostic could be used as either a TG FROG or SD FROG. The TG FROG has greater sensitivity but also greater complexity. Although aligning three beams spatio-temporally is more difficult, the

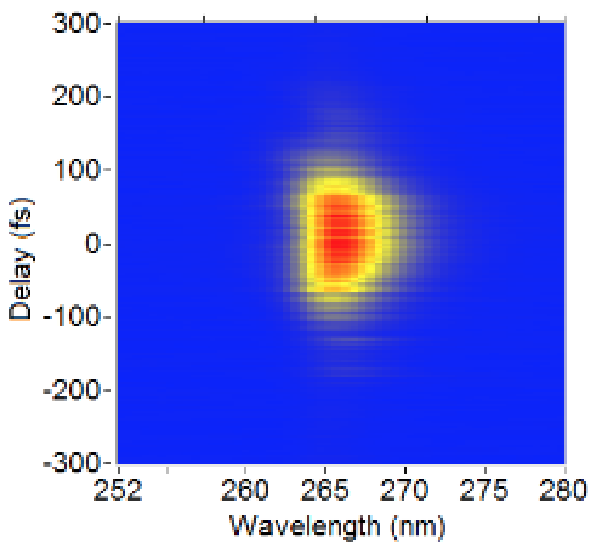

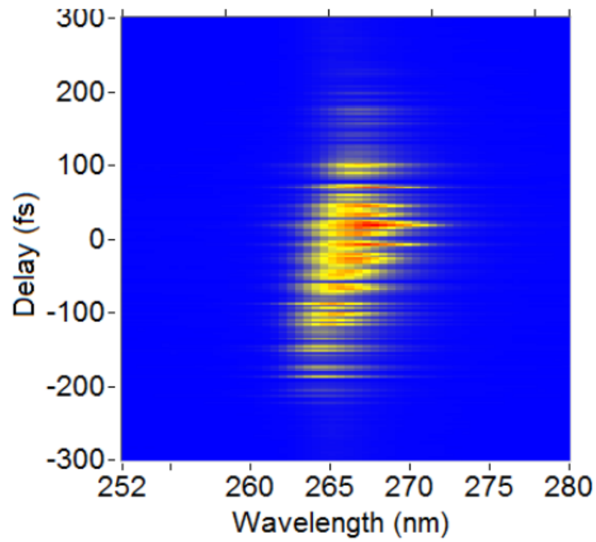

Figure 4.18: Time vs. wavelength traces of generated third harmonic pulses using an SD FROG. The fundamental was a τ =45 fs, λ = 800 nm, I = 400 GW/cm^2 pulse, and generated the third harmonic at 14% efficiency. The trace on the left is of a pulse generated from a fully compressed fundamental frequency pulse, while the trace on the right is of a pulse where positive chirp has intentionally been introduced. Larger pointing fluctuation due to air currents contribute to the discontinuous nature of the measurements in the case with linear chirp.

availability of three beams greatly aided in spatio-temporal alignment of two beams for a SD FROG configuration. The two fixed path beams immediately generate a SD FROG signal and their focus and signal intensity can be used to set the position of the fused silica plate before aligning the adjustable path beam to the same position. A compromise must be made between the shallow angle between the two beams required for phase matching, full angle $\theta < 2°$, and the necessity of separating input and signal beams. This is especially important since all beams have the same wavelength.

Fig. 4.18 are measurements using the SD FROG of a third harmonic pulse generated from a pulse with transform limited length τ =45 fs, λ = 800 nm, and I = 400 GW/cm^2. Delay is determined by path length difference between the two initial beams. At each delay, the spectrum of one of the signal pulses is recorded. Measuring the other signal pulse gives the same information but time is reversed. From this trace, the retrieval algorithm written by Trebino et al. [133] was used to recover the electric field. The trace shown corresponds to a τ = 60 fs third harmonic pulse.

Even before retrieval, traces recorded by the SD FROG are highly intuitive. On the right of Fig. 4.18 is a trace of the third harmonic when linear chirp was intentionally introduced

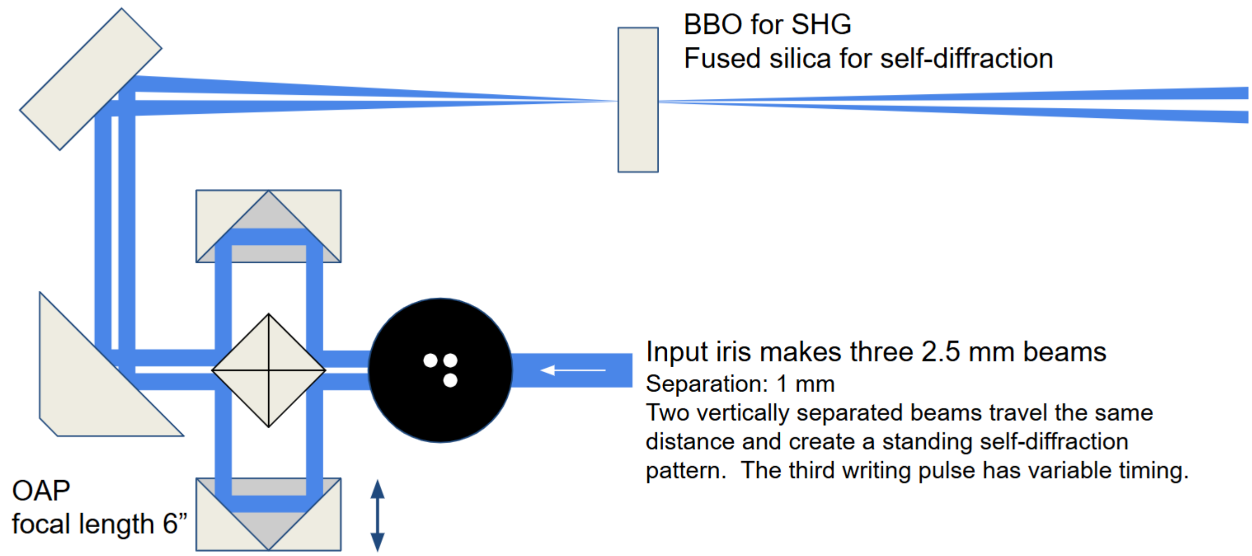

Figure 4.19: Layout of SD FROG device. The third harmonic beam enters in the bottom center of the schematic and is divided into three distinct copropagating pulses via a custom iris. Two pulses travel along a fixed path length line and the third propagates along a separate line with adjustable path length. The three are focused via an off-axis parabola onto a 2 mm thick fused silica plate. The fused silica plate was replaced with a BBO crystal for benchmarking the pulse measurement of the fundamental, using second harmonic generation, to GRENOUILLE results.

to the input. Unlike FROGs that use SHG, traces are not symmetrical and the direction of time is distinguishable. This trace reflects positive chirp. On the left in Fig. 4.18 is a trace of the third harmonic generated from an optimized, transform limited fundamental that shows no chirp, but the "D" shape shows the presence of a cubic nonlinearity.

Equipped with pulse profile, energy and spatial profile measurements, intensity profile could be obtained and used to determine compatibility of the third harmonic for ionization injection.

In summary, high intensity, short pulse third harmonic generation has been explored for the purpose of assessing suitability of use of the third harmonic of a Ti:Sapphire system for ionization injection into a laser driven plasma accelerator. Second and third harmonic conversion efficiencies as a function of optic thickness, crystal type, pulse width, bandwidth and input intensity were measured. In addition to brief interaction times of ultra-short pulses within a crystal, imperfect phase matching across the broad bandwidth required to generate short pulses impacts overall harmonic conversion efficiency. It was shown that at these high intensities, SPM led to asymptotic growth in conversion efficiency, limiting THG conversion efficiency to $< 10\%$ unless mitigated. Harmonic conversion efficiency, paired with pulse profiles measured with an SD FROG built for this study, were in agreement with results from a split-step code that aided design for high power operation. Exploration of meeting laser requirements for a demonstration experiment of two-color ionization injection have been detailed. Next the method of selection and characterization of the gas target appropriate for a two-color ionization injection demonstration experiment, including the use of a gas density diagnostic used for the first time on LPA targets, will be shown.

Chapter 5

Gas Density Profile Characterization

The plasma used for LPAs are generated from neutral gases and therefore controlling the gas profile is the first step in shaping the plasma profile. Several studies have explored tuning resulting beam properties by manipulating the density profile of gas jet targets, for example by modifying compressible flow properties to generate distinct profiles such as thin shocks [52, 54, 55, 56, 57, 136, 137, 138, 139]. As LPA targetry evolves, verification of these tailored jets calls for more detailed gas density diagnostics than those traditionally used.

This study explored the utility of planar laser-induced fluorescence (PLIF) for aiding in-depth studies of LPA gas jet profiles. Density profiles for these targets are commonly obtained by interferometry, which is simple and accurate, but yields line-of-sight, one-dimensionally integrated density values. Integration poses challenges to attempts to resolve small features, such as shocks, or to characterize highly asymmetric gas jets. Three dimensional profiles can be obtained but often require the jet to be cylindrically symmetric, where an Abel inversion can be applied, or to undergo tomographic reconstruction, where the resolution is determined by the number of images taken at different angles. PLIF was able provide intuitive 2D images of the inner structure of gas plumes with minimal post-processing and can be used to meet both resolution and asymmetry requirements of tailored gas jets. Using a laser sheet to fluoresce a thin slice of the jet, PLIF results in high resolution images that have been proven to resolve features relevant for tailored gas jets, and only a small translation of the nozzle or laser was required to obtain multiple slices that can be stacked to create a three-dimensional image of the plume.

Initial gas target designs for a proof-of-principle two-color ionization injection experiment were informed by fluid simulations using OpenFOAM. Supersonic nozzles were selected with millimeter gas profiles and designed to deliver gas densities that would ionize to $n_e \sim 10^{18}$ cm^{-3} plasma densities with sharp boundaries. Manufactured nozzles were subsequently characterized using PLIF, and measurements used to modify designs as necessary. Finally, PLIF was used to qualify nozzles appropriate for application.

5.1 Experimental Methods

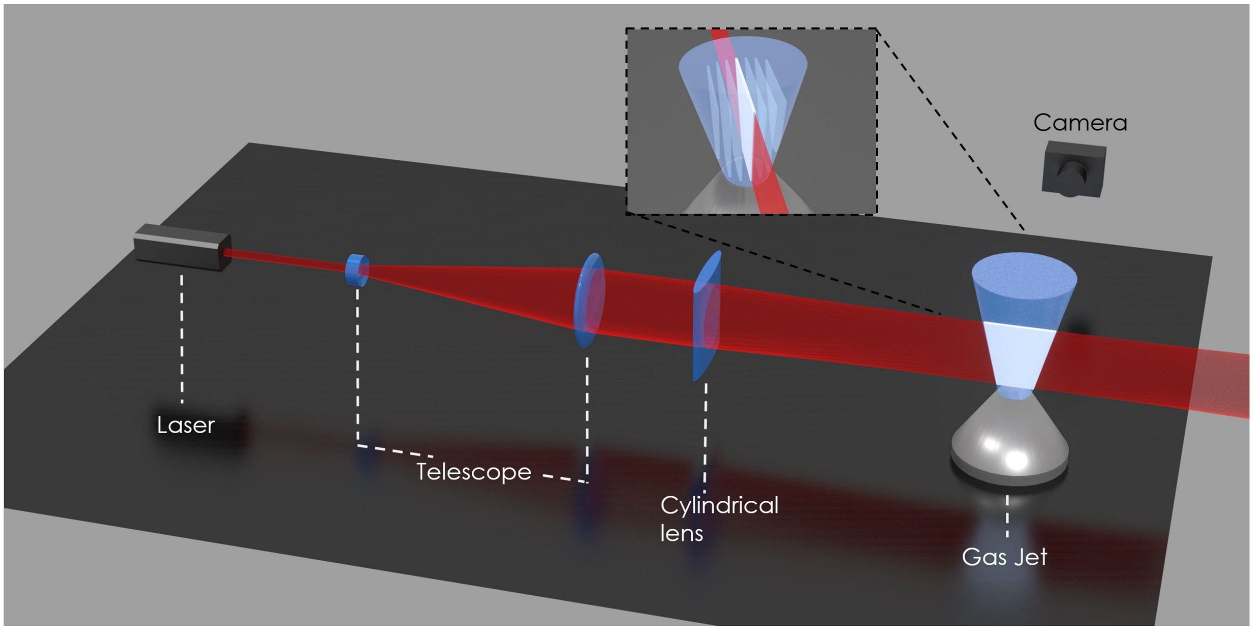

Figure 5.1: Schematic of a planar laser-induced fluorescence experimental configuration. A line focus is formed by means of a cylindrical lens and fluoresces a sheet of gas in the nozzle. Fluorescence is captured by a camera transverse to the laser propagation direction. The nozzle is on a stage so that successive slices can be imaged that can be stacked to form a 3D profile of the plume.

Planar laser-induced fluorescence is a well known technique but until now has not been used to study laser plasma accelerator targets [140]. In this experiment, acetone was used as a fluorescing seeding gas because it is a convenient fluorophore commonly used for PLIF due to its high yield, ease of accessibility, and low toxicity [141]. Fig. 5.1 shows the schematic of the experimental setup. Argon was bubbled through an acetone tank before being fed through a gas jet nozzle. The laser sheet was formed by spatially shaping a beam from a frequency quadrupled Nd:YAG laser. A prism was used to spatially separate out all other harmonics, leaving only the 266 nm wavelength beam, which was then sent through a 500 mm focal length cylindrical lens that focused the beam along one axis, forming a 5 mm high, 60 μm wide laser sheet. The resulting laser sheet was sent through the gas jet that was enclosed in a small vacuum chamber continuously pumped by a roughing pump. Background chamber pressure was measured by a capacitance manometer. The fluorescence signal was recorded by an electron-multiplying charge-coupled device (CCD) camera through a window perpendicular to the laser sheet. In this way, a fluorescent slice of the jet was obtained.

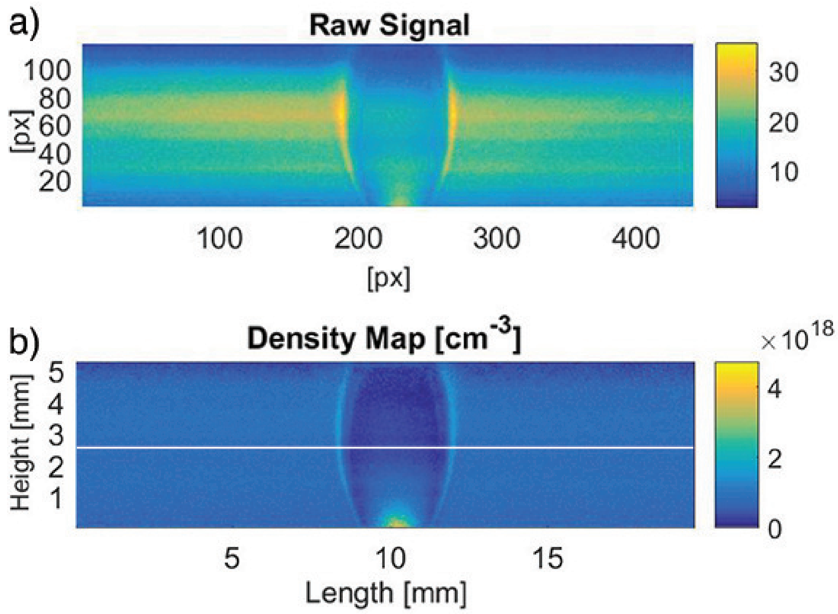

Figure 5.2: a) Raw image of laser induced fluorescence signal, and b) image after flattening with a reference beam and scaled according to pressure to signal relations (bottom). The colorbar in a) shows counts while the colorbar in b) shows plasma density in cm^{-3} were the gas to be fully ionized.

Under vacuum, plumes experienced low turbulence and several images could be averaged to increase the signal-to-noise ratio. Shown in Fig. 5.2 are raw measurements and background subtracted calibrated images of a gas plume of a Mach 2.5, 1 mm exit diameter nozzle. Calibration was obtained by measurements of fluorescence signal as a function of uniform gas density. Image resolution was limited only by camera-objective resolution while slice thickness is determined by the thickness of the laser sheet. A more tightly focused beam will give a thinner, sharper slice of the gas jet. In the example shown, the beam width at focus was 60 μm with a Rayleigh length of 1 cm. Variations in intensity of the laser sheet resulted in variations in signal. These variations were accounted for by dividing out a reference scan where the sheet illuminates a homogeneously filled chamber of gas of known pressure.

By placing the focusing lens on an adjustable stage, the laser sheet could be translated and thereby successive neighboring slices of the jet could be captured. These slices could then be stacked to form a three dimensional reconstruction of the gas jet. As a demonstration, PLIF was used to image a plume generated by a nozzle whose plume was intercepted by a razor blade 600 μm above the exit of the gas jet nozzle, creating highly asymmetric features. As shown in Fig. 5.3, a 3D reconstruction of the plume showed features that were in qualitative agreement with simulation. Simulations were performed with OpenFOAM's compressible Navier-Stokes flow solver, *rhoCentralFoam* [142]. In order to model the flow that is expanding

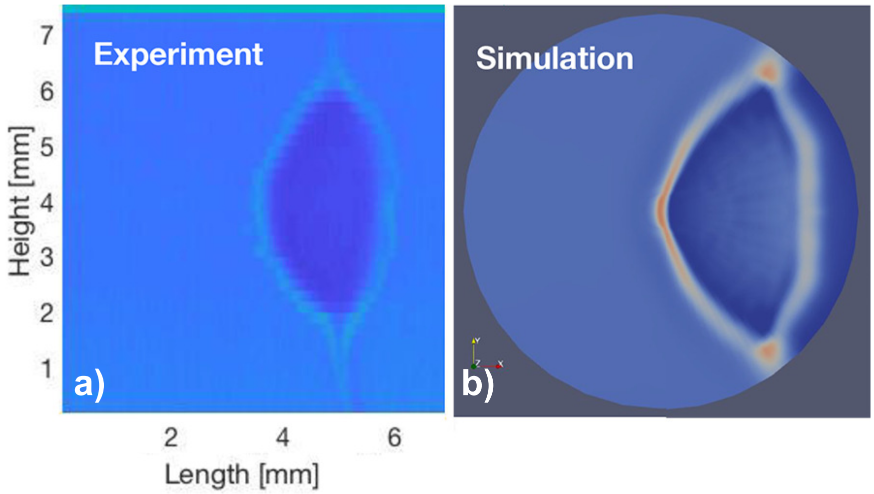

Figure 5.3: Top view (horizontal slice) of blade-in gas jet taken from 3D reconstruction of gas jet compiled from successive PLIF images a) showing similar features as had been been seen in simulations b).

from a reservoir through the nozzle into medium vacuum, and therefore is choked, sonic conditions were specified at the nozzle throat with a stagnation pressure of 25-100 psi. The back pressure was varied and the outbound flow was prescribed as homogeneous Neumann boundary conditions. Simulations were performed using the laminar flow approximation and flow was modeled as an ideal gas. Although the flow, with Reynolds number on the order of 1×10^5, is turbulent, the laminar approximation showed agreement with the computationally more expensive simulations that included turbulence to within a plasma wavelength and below experimental resolution. Further details on the study of shocks and flow parameters generated from blade-impinged plumes used for LPA targets can be found in Fan-Chiang et al. 2020 [143].

PLIF images captured illuminated slices of the gas jet showing density variations at high resolution. According to the Mott-Smith theory, and to simulations, shock features were expected to have a density gradient thickness of 3 - 4 mean free paths (mfp)[144]. A line-out of the the plume shown in Fig. 5.2 is seen in Fig. 5.4, and shows that measured density gradient thickness, defined as $\bar{x} = \Delta n_e / \left(\nabla n_e\right)_{max}$, was 130 μm, which is approximately 4 mfp at a density of 2×10^{17} cm^{-3}.

PLIF was used to customize and qualify manufactured nozzles for two-color ionization injection. The portion that a drive laser would sample was designed to match the acceleration length, which is near the Rayleigh range $2z_R = 3$ mm for a 20 μm focus that is not self-focused or guided with a preformed channel. Supersonic nozzles were chosen and are commonly used for LPA targets because they provide sharp vacuum to plasma boundaries. Mach number of

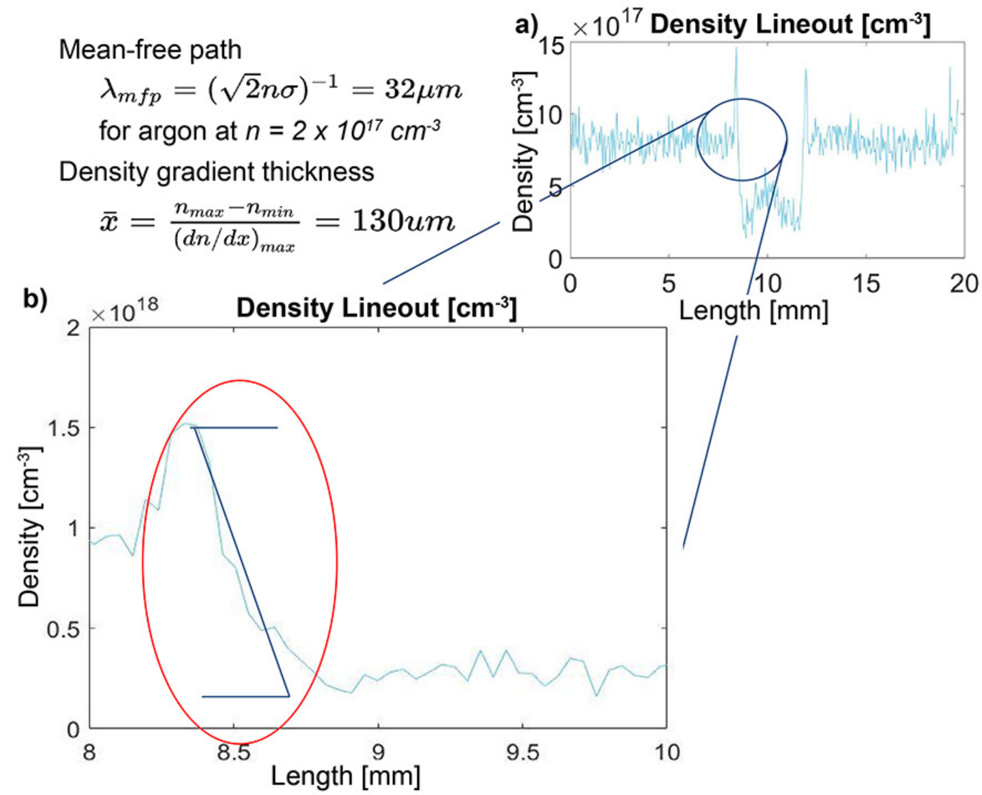

Figure 5.4: a) Horizontal lineout and b) close up of lineout of PLIF image of gas jet at the widest part of the plume (Fig. 5.2) show that the shock features have widths $\sim$ 4 mfp.

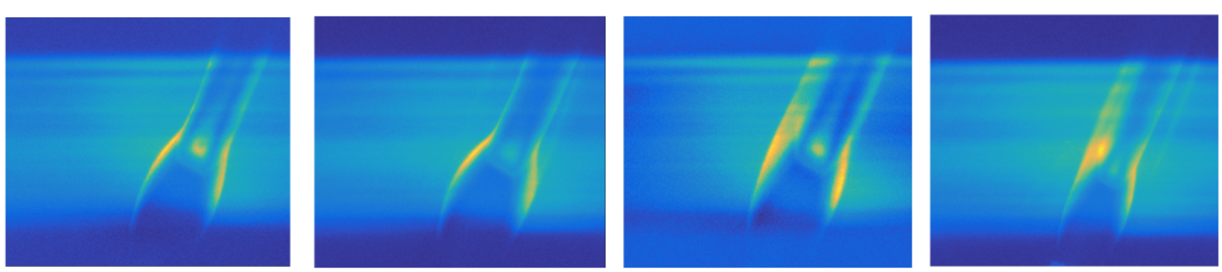

Figure 5.5: Raw PLIF measurements of various nozzles under the same conditions (10 psi backing pressure and 10^{-3} psi vacuum pressure) from the same manufacturer given identical specifications.

the nozzle was designed for allowing access to $n_e \sim 10^{18}$ cm^{-3} plasma densities with 100-400 psi backing pressure.

Manufactured nozzles for the experiment were individually characterized visually using a microscope, and using PLIF imaging of gas plumes at various pressures. Fig. 5.5 shows PLIF measurements of various nozzles from the same manufacturer given the same specifications. Although experimental conditions were identical, nozzle performance varied with small imperfections introducing asymmetric features. Fig. 5.6 shows a PLIF measurement of the nozzle that was used for two-color ionization injection tests.

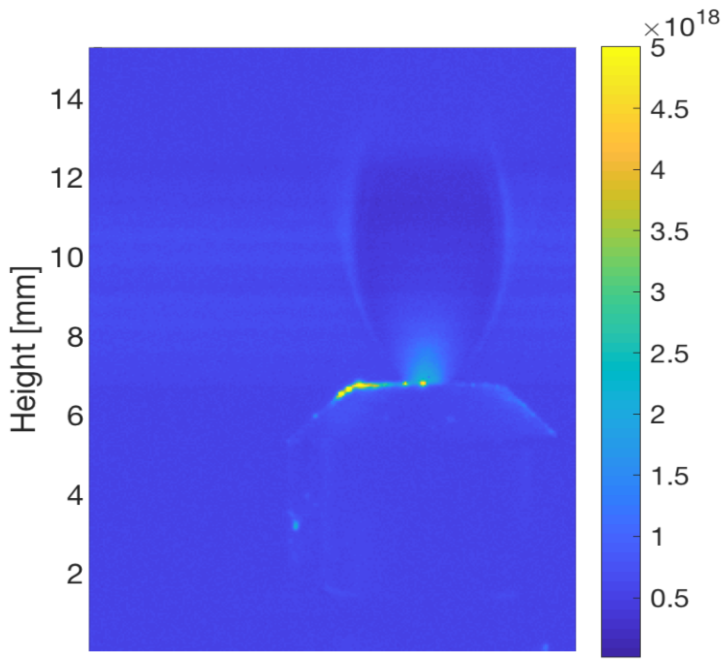

Figure 5.6: Fluorescence image of nozzle plume processed with background reference. The nozzle has a design Mach number of M = 2.5 and a 1 mm exit diameter. The colorbar shows plasma density in cm^{-3} were the gas to be fully ionized.

In summary, planar laser-induced fluorescence was used for the first time to customize and characterize gas jet plumes used for laser wakefield acceleration. Asymmetric plumes, generated by intersecting the plume with a thin blade, were measured to demonstrate the power of the diagnostic and results agreed qualitatively with 3D fluid simulations. The diagnostic was then used to customize and select nozzles suitable for a demonstration experiment of two-color ionization injection. In the next chapter, design considerations, methods and results of implementation of a trailing third harmonic ionization injector into a preformed wake, formed from sampling the plume shown in Fig. 5.6, will be described.

Chapter 6

Wakefield and Injector Coupling

A proof-of-concept demonstration experiment of two-color ionization injection was designed for, and component tested on, the 100 TW Ti:Sapphire (HTT) laser system at BELLA Center, which is divided into two main beam lines - a drive laser delivered 1 J on target in a 75 mm diameter beam focused to $w_0 = 20$ μm, and an injector laser delivered up to 250 mJ in a 22 mm diameter beam with adjustable focus. Both have a minimum, bandwidth limited, pulse length of $\tau_{FWHM} = 33$ fs. In addition, a collimated 10 mm transverse probe line delivered 1 mJ on target.

Fig. 6.1 shows a schematic of the layout of the target chamber where drive laser focus, injector laser focus, transverse probe, and gas target meet. The three beams emerge from the left of the schematic. After dividing from the shared front-end laser system, the three undergo independent amplification, compression, over 10 m of path length, and focusing before meeting the gas target in the target chamber with micron-level spatial and femtosecond-level temporal control.

The injector line is converted into a beam containing the first, second, and third harmonics of $\lambda = 800$ nm. The three harmonics are separated by mirrors coated to reflect ultraviolet and pass the first and second harmonic. Isolated UV is then focused by an off-axis parabola (OAP) into a wakefield left by the 20 μm drive focus. The drive line (red) passes through a hole in the injector OAP, ionizes the outer electronic levels of the gas and drives a plasma wakefield. The 1 mJ probe begins near the top of the schematic and passes through the target transverse to the drive propagation direction and images the target onto a wavefront sensor outside of the chamber.

Methods for precise spatio-temporal alignment of drive, injector pulse, probe laser, and gas nozzle, as well as experimental results from implementation of these methods, are the subjects of this chapter. We begin with drive laser focus and its optimal orientation relative to the gas target. Design considerations and results of focusing the third harmonic injector laser, and finally methods of spatio-temporal coupling of the injector focus with the pre-formed wake, follow.

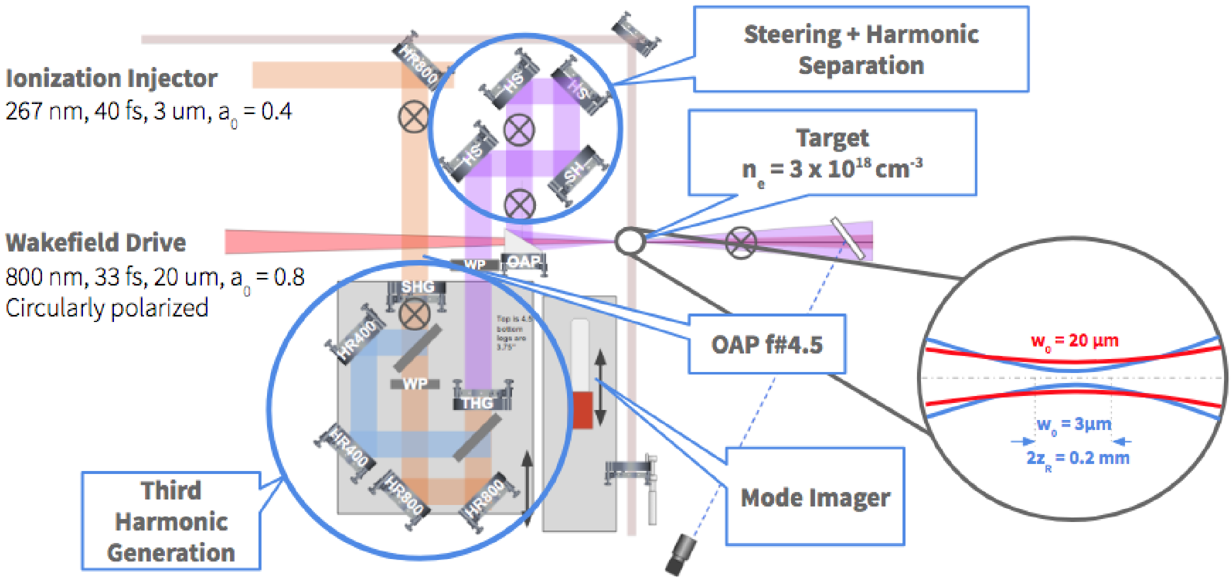

Figure 6.1: Schematic of two-color ionization injection tests at high power on the hundred terawatt Thomson (HTT) system at BELLA Center. The drive laser delivers 1 J at $\lambda = 800$ nm on target in a 75 mm beam focused to $w_0 = 20$ μm using a $f = 1.5$ m OAP. The injector laser delivers up to 500 mJ in a 22 mm diameter beam before conversion to its third harmonic and focused by a $f = 230$ mm OAP with a hole that allows the drive focus to pass through. A 1 mJ probe passes the target transversely and images the target onto a wavefront sensor.

6.1 Wake Driver and Gas Jet Positioning

The wake driver was focused by means of a 1.5 m focal length OAP to a FWHM spot size of $w_{FWHM} = 20$ μm and imaged post-focus by spherical mirrors, designed for 2.7 times magnification, to two cameras outside of the chamber. Outside of the chamber the image was sent to a CCD camera as well as a wavefront sensor. The CCD camera was mounted on a translating stage such that propagation around focus could be assessed and exact longitudinal positioning of focus could be determined. The wavefront sensor was used to feedback to a deformable mirror that precedes the drive laser OAP and can be used to correct higher order astigmatisms. A deformable mirror is an adaptive reflective optic that is connected to an array of small motors that can be used to precisely shape the phase distribution of the collimated beam. The Shack-Hartmann wavefront sensor consists of an array of lenslets that sample the beam, forming an array of beam tilts onto a CCD, which can be used to retrieve the wavefront of the beam. The wavefront sensor records phase images of the beam with respect to motor positions of the deformable mirror and the deformable mirror uses this knowledge to match an ideal phase front, in this case, the output of a single mode fiber laser placed at the focus of the drive laser.

The plasma is formed by ionization of neutral gas by the front of the laser pulse. The gas target was chosen to host $L = 3$ mm of acceleration length, spanning the Rayleigh range of the drive focus $2z_R = 3.2$ mm for a 20 μm waist at $\lambda = 800$ nm, and provide a source of a $n_0 \sim 10^{18}$ cm^{-3} background density plasma. The nozzle was cylindrically symmetric with a design Mach number of M = 2.5 with a 1 mm opening and was mounted on stages that allowed three axes of translation with 0.1 μm accuracy.

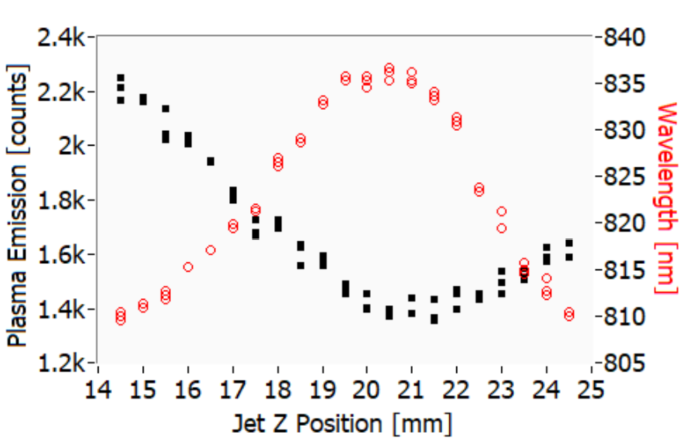

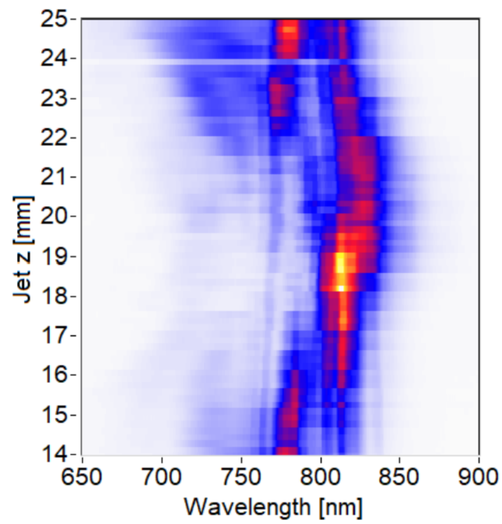

Figure 6.2: Redshift of post-interaction drive laser spectrum (right axis) and plasma recombination emission intensity as seen from above the interaction point (left axis) as a function of longitudinal position of the gas nozzle relative to the drive laser focus as well as corresponding spectra (right image).

Relative positioning of drive laser and gas plume was optimized by recording post-interaction drive laser spectra as well as looking at plasma recombination emission via a camera positioned on top of the chamber. As an example, the left plot in Fig. 6.2 shows results from post-interaction spectra as well as plasma emission as a function of nozzle longitudinal position. The right axis shows the center wavelength of the post interaction drive laser spectrum. The left axis shows the intensity of recombination emission. Both redshift and blueshift of the spectra occur. Redshift of the spectrum from wake formation was discussed in Chapter 3. In addition, blueshift occurs when the laser pulse samples a plasma density gradient such that the laser phase velocity nearer to the peak of the pulse is greater than that of the front. The effect is prominent when ionization occurs over long distances relative to the pulse length. In the case shown here, when the focus is before or after the edge of the gas plume, the intensity at the foot of the pulse of the defocusing is insufficient to instantaneously ionize the outer shell of the gas and therefore ionization occurs up through the peak of the pulse intensity envelope, resulting in the peak of the pulse experiencing higher plasma density than the foot.

Of significance, blueshift from an ionization gradient is often accompanied with ionization defocusing. Since the pulse is most intense on-axis, a spatial density gradient will cause the plasma to act like a lens and lead to divergence of the beam. Defocusing could cause the beam to never reach the intensities intended to drive the wake. For this reason, LPA targets are engineered to be highly localized, either by confining the gas to a gas cell with a small hole for the laser to enter, or by using supersonic nozzles that create gas density profiles with sharp boundaries. Optimal position of laser focus is at or near this boundary where the minimal amount of blueshift and the maximal amount of redshift, indicating long acceleration lengths, occurs. Ionization defocusing, which leads to larger ionization volumes, can be detected as increased recombination emission compared to the case of no defocusing, as seen in 6.2.

Nozzle height relative to the drive laser is selected to achieve the desired neutral gas density. While neutral gas density can be changed by pressure control of the gas before it enters the chamber, accessible density range, as well as gas length, can be adjusted by varying the nozzle height relative to the drive laser focus. A lower limit is set by damage to the nozzle by the wings of the laser focus.

6.2 Injector Focus

The third harmonic injector was focused into the the preformed wakefield by a 228 mm focal length, 90 degree, off-axis parabola coated with UV enhanced aluminum. The OAP mount was equipped with three axes of translation and three axes of rotation with μm precision for focal optimization and focal positioning. A 16 mm hole was drilled through along its focal axis in order to pass the drive laser focus that is 12 mm in diameter at the rear of the injector OAP. This configuration has the disadvantage of loss of energy near the center of the beam where the intensity is the highest, and difficulty of alignment. In this case, 16% of third harmonic energy was lost in the hole. However, the configuration prevailed over many common methods of laser coupling, as will be explained below.

Focusing by means of a transmissive lens is common, however, 1) high intensity input risks nonlinear focusing, filamentation, and self phase modulation in the material, 2) broad bandwidth leads to chromatic aberration for a singlet lens resulting in pulse lengthening at focus, and 3) ultraviolet is more easily absorbed in materials and an equivalent lens would absorb 12% of the energy.

Due to dispersion, the phase and pulse fronts experience a relative delay and, therefore, the pulse length increases by

$$\Delta\tau(r) = \frac{\lambda}{c}\frac{d^2n}{d\lambda^2}\Delta\lambda l(r) \ ,$$

where $l(r)$ is the path length of a ray in the lens material [145]. On-axis, where radius $r = 0$, for focal length f = 230 mm and beam radius $r_0 = 11$ mm, the difference between flat pulse front and focal plane is 80 ps. Although, theoretically, an achromat could compensate chromatic aberration, achromats are composed of two materials with similar but differing indices of refraction and vendors found it difficult to meet the specifications for UV wavelengths. In addition, typical adhesives used to join the two materials could not be used due to the high power and vacuum application. In principle this achromat could be made air spaced and with magnesium fluoride or another UV transparent material at higher cost but the problem of introducing extra transmissive material at high power remains.

Energy loss could be reduced if the injector was focused at a shallow angle relative to that of the drive laser, negating the requirement for a hole in the focusing optic. However, since emittance $\epsilon_x \propto w_0^2$, the angle must be small. Fig. 6.3 shows a schematic of the possible configuration. The effective focus increases as $w = w_0 + \theta z_R$ and is double the diffraction limited focus for $\theta = 1°$. Physically, in order to avoid obstructing either beam, the angle must be $> 4°$. Therefore, this option was assessed to be inappropriate for the application.

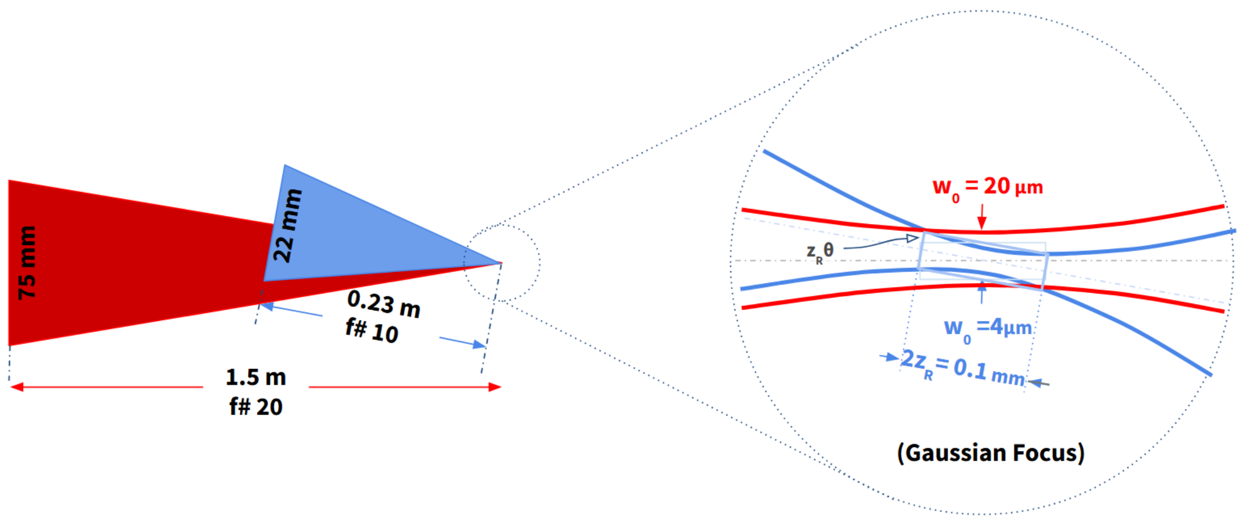

Figure 6.3: Schematic of effect on the injection focal size if injecting off-axis.

Finally, alignment could be simplified if focal quality and positioning were decoupled by inserting a flat mirror with a hole in it that reflects a focusing beam from an OAP just upstream of it. However, high fluence on the final optic places a lower limit on its distance from focus. Using the OAP as the final optic allowed the shortest focal length, and thus smallest w_0, while avoiding damage to optics.

Fig. 6.4 shows the third harmonic profile after focusing by the 230 mm focal length OAP with 16 mm hole. The focus contains 26% of the energy in a 3 μm FWHM spot. Focal profile, combined with energy measurements summarized in Fig. 4.12, and simulated pulse lengths, give maximum intensities corresponding to $a_0 = 0.43$, which is sufficient for ionization injection into a preformed laser generated wakefield using a nitrogen dopant, and more than sufficient if using a higher atomic number dopant, such as argon.

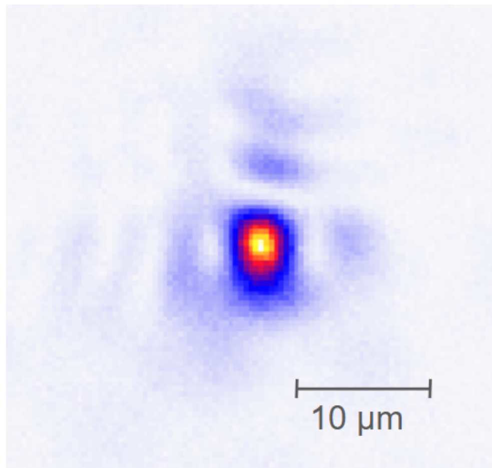

Figure 6.4: Profile of third harmonic focus containing 26% of 25 mJ within the 3 μm central spot.

6.3 Spatial Overlap

Injector focus must aim to ionize on the axis of a wakefield produced by a $w_0 = 20$ μm drive focus. Focal positioning was controlled by the three degrees of translation afforded to the injector OAP, each with 0.1 μm steps and 1 μm accuracy. Overlap was achieved via a sequence of diagnostics with increasing resolution. These methods for achieving spatial overlap are described here.

The Y (perpendicular to the optical table) and Z (along the laser propagation direction) axes were first approximated by aid of the transverse optical probe. Depicted in Fig. 6.1, the 1 mJ probe passes through the target transverse to the drive and injector propagation direction and images the target plane onto a wave-front sensor outside of the chamber. An example plasma profile can be seen in Fig. 6.5. This diagnostic gave $\sim$10 μm resolution.

Initial X position, transverse to the propagation direction and horizontal to the optic table, was approximated by looking at plasma emission from a window above the target chamber. The diagnostic, which had been previously implemented on the HTT target chamber, gave millimeter level precision.

Sub-millimeter precision was accomplished by imaging both drive and injector foci onto the same camera. Imaging both foci simultaneously could not be performed at high power due to the differing f-numbers. At low power, the foci could be redirected before the target

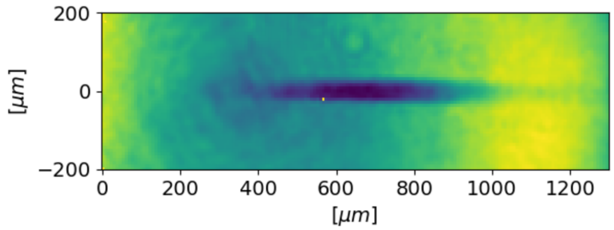

Figure 6.5: Image recorded by the wavefront sensor of a plasma produced by the drive line. Phase difference experienced by the transverse probe, which images the interaction point onto the wavefront sensor, relative to a reference taken with no gas, can be used to retrieve plasma density.

and simultaneously imaged onto a camera. A fused silica singlet lens and quartz crystal microscope objective were used to image the focal plane onto a camera. Although easier to align than the using reflective focusing optics, lenses resulted in chromatic aberration. Ensuring that the beams were collinear was accomplished by recording relative positions of the beams on the camera as the camera was translated longitudinally through focus. Longitudinal overlap was complicated by both chromatic aberration and incongruent self-focusing of each beam after amplification. The drive line focus moved upstream by 4 mm while the injector line focus moved upstream 3 mm after amplification to high power. Approximate longitudinal overlap was accomplished at low power using the residual fundamental frequency found in the injector line after replacing harmonic separators with aluminum mirrors. In order to accomplish longitudinal overlap at high power, the focal shifts were separately assessed using the drive line high power mode imager and the injector mode imager and subsequently compensated.

Positioning was further refined by recording the effect of a pre-pulse on single pulse ionization injected electrons. The injector was timed 3 ns ahead of the drive laser, pre-ionizing and perturbing the plasma before the arrival of the drive. Severe steering and charge fluctuations of the resulting electron beam could be attributed to this perturbation. Fig. 6.6 shows electron beam profiles recorded by camera images of a phosphor screen on which the beams terminated. The third harmonic focus was scanned in X position. Gas density was increased to the point that the drive laser self-focused and beams were produced by single pulse ionization injection. It can be seen that away from overlap, the electron beam was undisturbed. Symmetrical about one position, however, beams are heavily impacted by the third harmonic pre-pulse and are visibly steered in the direction that the pre-pulse was misaligned. This method has μm level resolution. It can be seen from Fig. 6.6 that the Y position had not yet been adjusted since the beam was visibly steered down. This was followed by an equivalent pre-pulse scan along the Y direction and gave results agreeing with that given by the transverse probe.

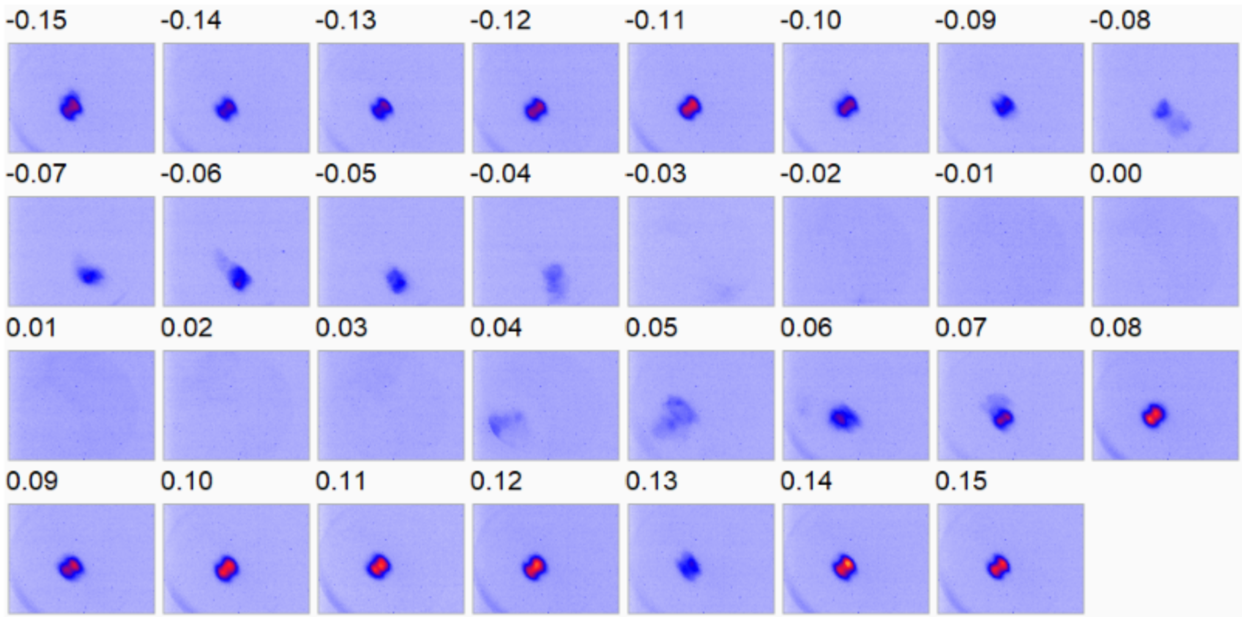

Figure 6.6: Electron beam profiles as captured by a phosphor screen 1.5 m from the target and imaged onto a camera. Figure tiles capture 33 x 33 mm. The gas density was increased so that single pulse ionization injection occurs, and the third harmonic was timed 3 ns ahead of the drive laser to act as a pre-pulse. The X position of the third harmonic focus was scanned and the effect on the resulting electron beam recorded. Displayed values are in millimeters.

6.4 Temporal Overlap

Timing between drive and injector pulses determines injection phase within the wake. Delay between the two pulses needs to be controlled to within a fraction of the pulse length. For plasma wavelengths on the order of 10 μm, path length resolution between the pulses should be $\leq$1 μm. Temporal overlap to nanosecond accuracy was achieved by shining both drive and injector beams on a photodiode. Once overlapped to within a nanosecond, the transverse probe could be used. By scanning probe timing until it sampled the initial formation of plasma by the drive laser, the probe could be used to time the injector until the ionization front of the injector could be seen. This method gave 100 μm (300 fs) level precision.

Timing overlap was further improved by use of a spectrometer. Harmonic separators were temporarily replaced with aluminum mirrors to allow residual fundamental frequency in the injector beamline to be used for spectral interference with the drive line. Fig. 6.7 shows a series of spectra of both drive and injector gathered as a function of relative timing between them (left), and a sample of the resulting spectrum when fringes are apparent (right). Fringes can be clearly seen $\pm$400 fs from perfect overlap. A scan of relative delay gives a symmetric

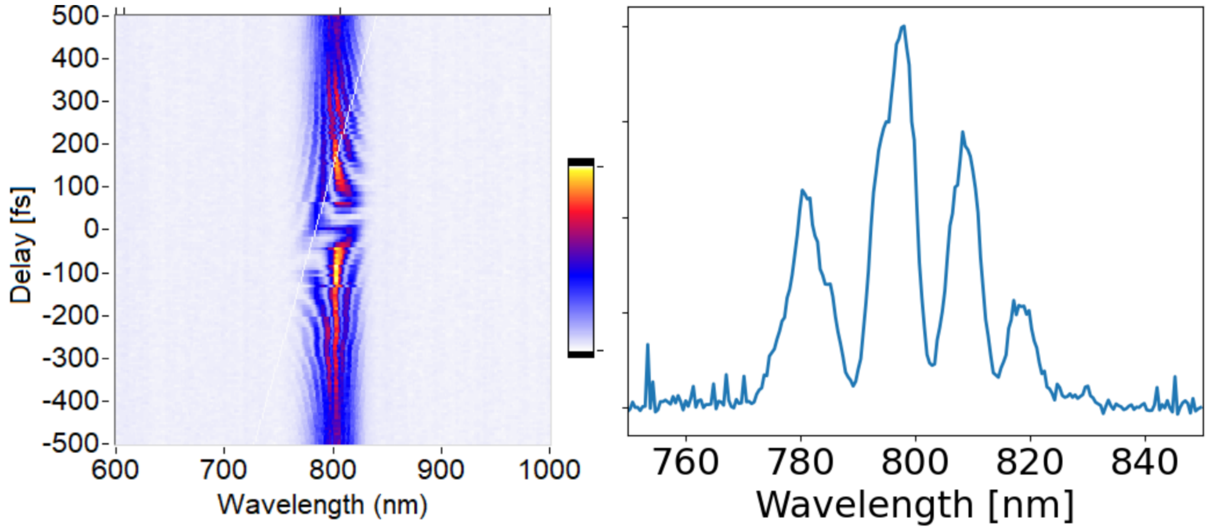

Figure 6.7: Post-interaction spectra of the drive laser and the residual fundamental frequency of the injector line. Left: Several spectra are plotted as a function of delay between two beams. Right: Sample spectrum at 26 fs from perfect overlap where large fringes are clearly distinguishable.

set of spectral fringes and, as can be seen in Fig. 6.8, a linear fit to retrieved group velocity delay (GVD) results in an intersection at zero GVD that pinpoints timing overlap to < 0.1 μm (< 0.3 fs).

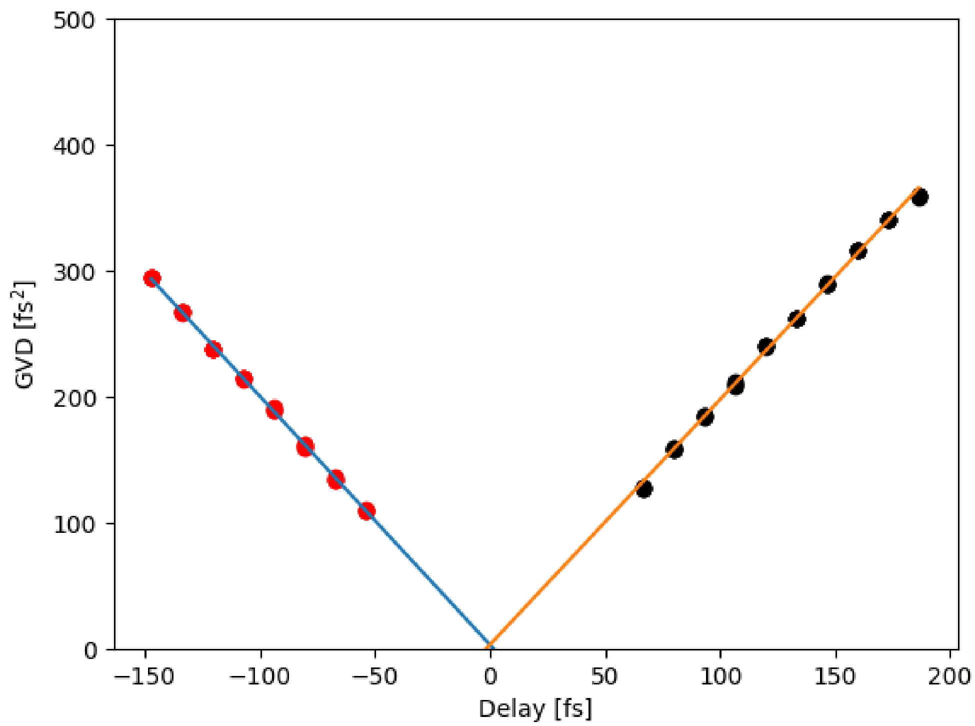

Figure 6.8: Group velocity delay retrieved from spectral fringe spacing in Fig 6.7. Near temporal overlap between two pulses, fringes are less distinct but a linear fit symmetrically about overlap gives sub-fs temporal overlap.

Chapter 7

Conclusion

High amplitude wake formation, injector preparation, gas characterization, and methods of spatial and temporal alignment on the micron and femtosecond scale have been tested in preparation for demonstration of the generation of ultra-low emittance beams using two-color ionization injection and reported in this thesis. It was found that in order to prepare high amplitude wakes with no self-injection, the simplest configuration, using a circularly-polarized wake driver, was sufficient for suppressing ionization of inner-shell electrons while generating a wake with high enough field amplitude to trap and accelerate injected electrons. Measurements of redshift of post-interaction drive laser spectra showed that using a circularly polarized drive laser pulse suppressed injection between $n_e = 4 \times 10^{18}$ cm^{-3} and $n_e = 6 \times 10^{18}$ cm^{-3} while generating equivalent wake amplitudes to that when using a linearly polarized drive laser pulse that led to injection in the same regime. This regime can therefore be used for further ionization injection. Combining circular polarization with multi-pulse configurations can extend this regime to lower densities.

Generation of UV pulses for use as an ionization injector showed that despite limits to harmonic conversion efficiencies of intense, short-pulse, and therefore broadband, pulses, generated intensities, corresponding to $a_0 = 0.43$, were sufficient for use of the third harmonic of $\lambda = 800$ nm for ionization injection of the fifth level of nitrogen. A neutral gas density diagnostic, PLIF, was used for the first time in designing and characterizing gas targets for LPAs, and enabled characterization of gas plumes and ultimately selection of nozzles with the desired features. Supersonic nozzles were chosen in order to provide a sharp vacuum-plasma boundary. Nozzles were designed to allow 3 mm of acceleration, matching the Rayleigh range of the drive laser focus, and to provide $n_e \sim 10^{18}$ cm^{-3} plasma densities. Finally, methods of spatial and temporal coupling of the injector with the wake on the micron and femtosecond scale were tested and it was shown that using a series of increasingly precise diagnostics, coupling at the scale required for injection can be achieved.

Fig. 7.1 shows a case study for generating $\epsilon_x = 0.35$ mm mrad and $\epsilon_y = 0.05$ mm mrad normalized emittance beams with two-color ionization injection using $\lambda = 800$ nm and $\lambda = 267$ nm laser pulses in a nitrogen doped helium plasma. Simulations were performed with INF&RNO [146], a 2D cylindrical, ponderomotive particle-in-cell (PIC) code, to simulate the

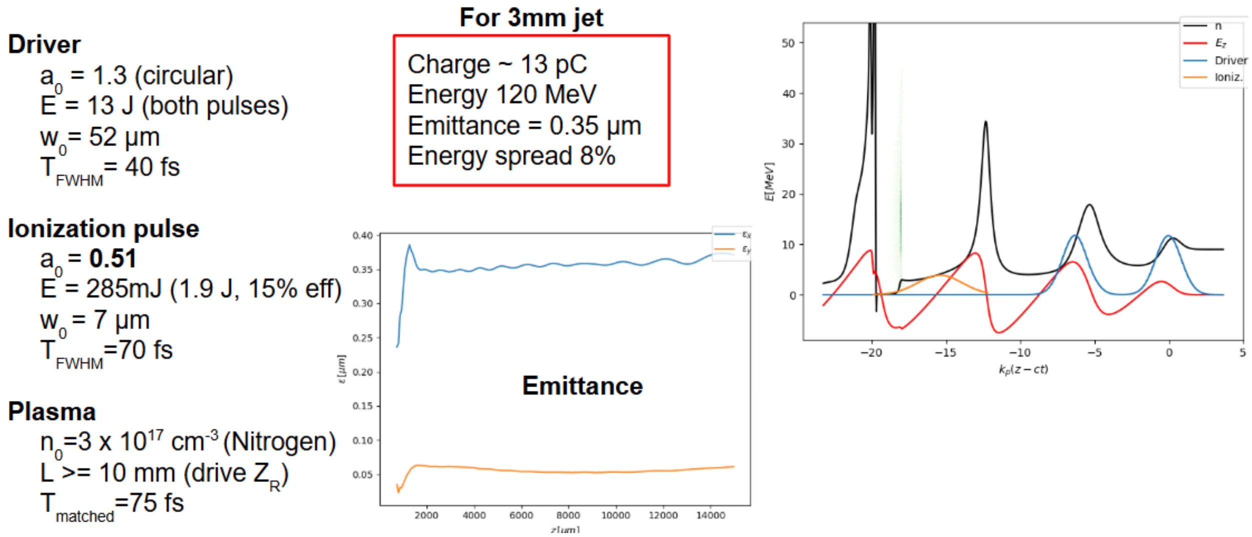

Figure 7.1: Case study for a demonstration experiment of two-color ionization injection on a Ti:sapphire laser system. Simulations were performed with INF&RNO, a 2D cylindrical PIC code, using a fluid description of the plasma and the quasi-static approximation for propagation.

laser-plasma interaction, including atomic ionization and the injection and acceleration of the electron beam. For laser parameters relevant to resonant multi-pulse ionization injection, the wakefield remains below the wave-breaking limit, and the plasma density is assumed to be uniform throughout the gas jet.

The drive laser consists of two trailing circularly polarized pulses timed one plasma wavelength apart from each other with $a_0 = 1.3$. The $\lambda = 267$ nm linearly polarized injector laser pulse, with $a_0 = 0.5$, ionizes the sixth and seventh levels of nitrogen inside of the wake to produce a 13 pC electron beam. Nitrogen was selected for several reasons. 1) Nitrogen is inert and easily accessible. 2) The large ionization potential gap ensures bound electrons remain after wake formation. 3) Outer shell electrons have low ionization injection thresholds that can be completely ionized at the foot of the first pulse, leading to reduced ionization defocusing of the drive laser. However, using nitrogen as the injector gas imposes a lower limit on thermal emittance since, for $\lambda = 267$ nm, a_i must be greater than 0.4 to ionize and inject inner shell electrons.

The use of gases with higher atomic numbers could lower ionization injection intensity requirements and result in lower emittance beams. Krypton, argon or xenon are all good candidates. Fig. 7.2 shows the tunneling ionization probability of argon for $\lambda = 800$ nm and $\lambda = 267$ nm. Argon could be used in the case presented above by doubling the number of drive pulses to lower the maximum electric field of the drive pulses while driving equivalently high amplitude wakes. Were the ionization injector to reach peak intensities corresponding

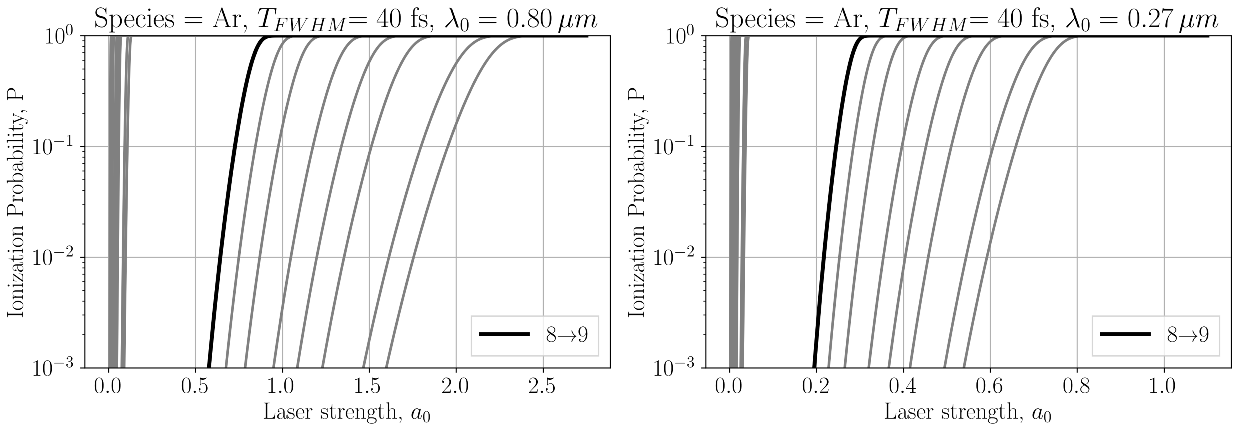

Figure 7.2: Tunneling ionization probability as a function of a_0 for argon for $\lambda = 800$ nm (left) and $\lambda = 267$ nm (right).

to $a_i = 0.3$, three electrons from each argon atom could contribute to injected charge. Rapidly progressing research in generating pulse trains and precise control of wake amplitudes with pulse trains will open many possibilities, including the potential for low intensity, high repetition rate, lasers to drive high field amplitude wakefields [102, 103, 104].

The use of krypton was studied via simulations in the first experimental design of a two-color ionization injection experiment, which proposed using CO_2 lasers for driving the wake [36], followed by a Ti:Sapphire laser for ionizing the ninth electronic level for injection. Wakes generated with these $\lambda = 10$ μm lasers can be very low density and provide large wakes for injection. In addition, a Ti:Sapphire laser at its fundamental or second harmonic can be used as an injector. A second harmonic injector can be produced at much higher harmonic conversion efficiency than that of the third harmonic. This configuration would give freedom for pulse and wake tailoring that is more difficult in small wakes. Short pulse CO_2 lasers are currently under development and may soon be applicable to producing low emittance beams [147].

Many elements of this study will already be useful to the broad community. Several injection techniques require preparation of dark-current-free wakes that can trap. The addition of a quarter-wave plate to create a circularly polarized wake driver is a low cost, low footprint, solution and can be used in conjunction with multi-pulse schemes for generating high amplitude wakes. The study of generation of intense short-pulse UV lasers has impact far outside of the laser wakefield community. Due to its ability to reduce thermal effects, and react strongly with material molecules, high intensity, ultra-short UV pulses have a number of scientific, medical and industrial applications [148, 149]. In addition, a FROG was built for this study to measure the temporal profile of the UV pulse that is compact, and, since it uses only reflective optics, wavelength agnostic. This will benefit other laser communities who use wavelengths that are not yet served by commercial products.

The PLIF gas density diagnostic is a powerful tool that has not yet been widely used in the LPA community that is now highly invested in gas density tailoring for a variety of effects [47, 150, 138, 57, 55]. This tool can be used to aid high resolution customization of gas plumes, especially asymmetric ones, which conventional techniques cannot sufficiently, or easily, capture. Finally, the combined use of commonly available diagnostics in laser labs to achieve micron and femtosecond level precision can be beneficial to communities that require similar precision.

Moving forward, the experiment studied here can benefit from a number of improvements. Multiple diagnostics would enhance the physics that can be gathered from this unique experiment. An improved wake diagnostic would give insight into emittance growth dynamics and help with customization of wake, injector, and gas profiles. In the quasilinear regime a good option is frequency domain holography using chirped probe and reference pulses [151, 152]. X-ray imaging of recombination light would improve understanding of ionization states, which is increasingly important when using high atomic number gases that have smaller ionization potential gaps than nitrogen. High emittance beams are intentionally generated to produce coherent betatron radiation. The HTT chamber previously was equipped with detectors for betatron radiation. This diagnostic could perhaps be used as a single-shot online proxy for low emittance beams. It does not, however, replace the requirement for an emittance measurement. An energy resolved source size measurement applicable to LPA beams can be made by using a quadrupole triplet to image the electron beam into an energy-dispersed magnetic spectrometer and recording the output fluorescence on a Ce:YAG screen [153, 32, 154]. PLIF was used in this study as a off-line gas density diagnostic, but could be modified to be used as an on-line diagnostic by using lasers with wavelengths that fluoresce either the working gas, such as helium, or the dopant [155]. A single-shot spatially resolved diagnostic such as PLIF would increase the data and understanding of the relation between neutral gas profiles and resulting plasma dynamics multi-fold.

Advances in laser technology will greatly benefit the success of generating ultra-low emittance beams. Laser repetition rate and stability are improving daily [156, 16, 157]. A significant difficulty faced in the component tests described in this thesis was energy, pulse length and pointing stability, and, therefore, beam reproducibility. Micron level accuracy is moot if beam jitter is multi-microns. Reproducibility is one of the key hurdles that must be surmounted if LPAs are to become ubiquitous tools for science, health, defense, and industrial applications, and laser stability plays a dominant part. Finally, lasers, which are the bulk of LPA facilities, continue to become more compact, for example delivering nearly 10 TW, which once required a room many meters in length, in a suitcase sized commercial system [158].

The study described in this thesis is only an injection technique and can be combined with developments that address all other aspects of wakefield acceleration such as increasing acceleration length with preformed plasma channels [30, 47], and adding a second LPA stage for further acceleration to increase final energy, and therefore decrease relative energy spread [159].

The beam properties of the beams generated by LPAs, compared to those generated by conventional accelerators, e.g., the short bunch durations and relatively large energy spread, are challenging to measure by conventional accelerator diagnostics, and thus the advancement of the field forced the creation and blossoming of a unique field of short-pulse, both lasers and particle beams, high resolution diagnostics [160]. But, as LPAs begin to generate ultra-low emittance beams they will also be able to leverage continuing advances in accelerator technology and to contribute to them. Independently, LPAs driving ultra-low emittance beams will provide compact sources of beams and coherent and incoherent light across the x-ray to infrared spectrum. They will be sources of XFEL radiation as well as potentially sources for plasma based colliders. But, as a low emittance source, LPAs can be inserted as a compact injection stage of RF driven linear accelerators [161], as well as serve as a diagnostic through ultrafast electron radiography [162, 163], ultimately combining research efforts to provide accelerated particles and derived light as irreplaceable tools for science and technology.

Bibliography

[1] T. Tajima and J. M. Dawson. "Laser Electron Accelerator". In: *Physical Review Letters* 43.4 (July 1979), p. 267. ISSN: 00319007. DOI: https://doi.org/10.1103/PhysRevLett.43.267.

[2] E. Esarey, C. B. Schroeder, and W. P. Leemans. "Physics of laser-driven plasma-based electron accelerators". In: *Reviews of Modern Physics* 81.3 (Aug. 2009), pp. 1229–1285. ISSN: 0034-6861. DOI: https://doi.org/10.1103/RevModPhys.81.1229.

[3] A. J. Gonsalves et al. "Petawatt Laser Guiding and Electron Beam Acceleration to 8 GeV in a Laser-Heated Capillary Discharge Waveguide". In: *Physical Review Letters* 122.8 (Feb. 2019), p. 084801. ISSN: 0031-9007. DOI: https://doi.org/10.1103/PhysRevLett.122.084801.

[4] T Tajima and V Malka. "Laser plasma accelerators". In: *Plasma Physics and Controlled Fusion* 62.3 (Feb. 2020), p. 034004. ISSN: 0741-3335. DOI: https://doi.org/10.1088/1361-6587/AB6DA4.

[5] D. A. Jaroszynski et al. "Radiation sources based on laser-plasma interactions". In: *Philosophical Transactions of the Royal Society A: Mathematical, Physical and Engineering Sciences* 364.1840 (Mar. 2006), pp. 689–710. ISSN: 1364503X. DOI: https://doi.org/10.1098/rsta.2005.1732.

[6] S. Corde et al. "Femtosecond x rays from laser-plasma accelerators". In: *Reviews of Modern Physics* 85.1 (Jan. 2013), pp. 1–48. ISSN: 15390756. DOI: https://doi.org/10.1103/REVMODPHYS.85.1.

[7] N. Huang et al. "Features and futures of X-ray free-electron lasers". In: *The Innovation* 2.2 (May 2021), p. 100097. ISSN: 2666-6758. DOI: https://doi.org/10.1016/J.XINN.2021.100097.

[8] I. Gadjev et al. "An inverse free electron laser acceleration-driven Compton scattering X-ray source". In: *Scientific Reports* 9.1 (Dec. 2019), pp. 1–10. ISSN: 20452322. DOI: https://doi.org/10.1038/s41598-018-36423-y.

[9] K. Khrennikov et al. "Tunable all-optical quasimonochromatic Thomson X-ray source in the nonlinear regime". In: *Physical Review Letters* 114.19 (May 2015), p. 195003. ISSN: 10797114. DOI: https://doi.org/10.1103/PhysRevLett.114.195003.

[10] S. Schindler et al. "Tunable X-ray source by Thomson scattering during laser-wakefield acceleration". In: *Laser Acceleration of Electrons, Protons, and Ions V*. Ed. by Eric Esarey, Carl B. Schroeder, and Jörg Schreiber. Vol. 11037. SPIE, Apr. 2019, p. 22. ISBN: 9781510627406. DOI: `https://doi.org/10.1117/12.2520354`.

[11] K. Behm et al. "Demonstration of femtosecond broadband X-rays from laser wakefield acceleration as a source for pump-probe X-ray absorption studies". In: *High Energy Density Physics* 35 (June 2020), p. 100729. ISSN: 1574-1818. DOI: `https://doi.org/10.1016/J.HEDP.2019.100729`.

[12] A. Doherty et al. "Femtosecond multimodal imaging with a laser-driven X-ray source". In: *Communications Physics* 6.1 (Dec. 2023), pp. 1–8. ISSN: 23993650. DOI: `https://doi.org/10.1038/S42005-023-01412-9`.

[13] V. Senthilkumaran et al. "Laser-driven betatron x rays for high-throughput imaging of additively manufactured materials". In: *Review of Scientific Instruments* 95.12 (Dec. 2024). ISSN: 0034-6748. DOI: `https://doi.org/10.1063/5.0221606`.

[14] J. Strehlow et al. "MeV x-ray production from a petawatt laser in the regime of a relativistically transparent preplasma, with applications to radiography". In: *Physics of Plasmas* 31.12 (Dec. 2024). ISSN: 1070-664X. DOI: `https://doi.org/10.1063/5.0237193`.

[15] J. Bin et al. "A new platform for ultra-high dose rate radiobiological research using the BELLA PW laser proton beamline". In: *Scientific Reports* 12.1 (Dec. 2022), pp. 1–15. ISSN: 20452322. DOI: `https://doi.org/10.1038/S41598-022-05181-3`.

[16] S. K. Barber et al. "Greater than 1000-fold Gain in a Free-Electron Laser Driven by a Laser-Plasma Accelerator with High Reliability". In: *Phys. Rev. Lett.* 135.5 (July 2025), pp. 055001–055009. DOI: `https://doi.org/10.1103/vh62-gz1p`.

[17] M. Balcazar et al. "Multi-messenger dynamic imaging of laser-driven shocks in water using a plasma wakefield accelerator". In: (Feb. 2025). DOI: `https://doi.org/10.21203/RS.3.RS-5811311/V1`.

[18] D. Oulianov et al. "Ultrafast pulse radiolysis using a terawatt laser wakefield accelerator". In: *Journal of Applied Physics* 101.5 (Mar. 2007). ISSN: 0021-8979. DOI: `https://doi.org/10.1063/1.2696204`.

[19] S. P.D. Mangles et al. "Monoenergetic beams of relativistic electrons from intense laser-plasma interactions". In: *Nature* 431.7008 (Sept. 2004), pp. 535–538. ISSN: 00280836. DOI: `https://doi.org/10.1038/NATURE02939`.

[20] C. G.R. Geddes et al. "High-quality electron beams from a laser wakefield accelarator using plasma-channel guiding". In: *Nature* 431.7008 (Sept. 2004), pp. 538–541. ISSN: 00280836. DOI: `https://doi.org/10.1038/NATURE02900`.

[21] J. Faure et al. "A laser-plasma accelerator producing monoenergetic electron beams". In: *Nature* 431.7008 (Sept. 2004), pp. 541–544. ISSN: 00280836. DOI: `https://doi.org/10.1038/NATURE02963`.

[22] R. Neutzo et al. “Potential for biomolecular imaging with femtosecond X-ray pulses”. In: *Nature* 406.6797 (Aug. 2000), pp. 752–757. ISSN: 00280836. DOI: `https://doi.org/10.1038/35021099`.

[23] F. Grüner et al. “Design considerations for table-top, laser-based VUV and X-ray free electron lasers”. In: *Applied Physics B: Lasers and Optics* 86.3 (Jan. 2007), pp. 431–435. ISSN: 09462171. DOI: `https://doi.org/10.1007/S00340-006-2565-7`.

[24] K. Nakajima. “Compact X-ray sources: Towards a table-top free-electron laser”. In: *Nature Physics* 4 (Feb. 2008), pp. 92–93. ISSN: 17452481. DOI: `https://doi.org/10.1038/nphys846`.

[25] C. Bostedt et al. “Linac Coherent Light Source: The first five years”. In: *Reviews of Modern Physics* 88.1 (Mar. 2016). ISSN: 15390756. DOI: `https://doi.org/10.1103/RevModPhys.88.015007`.

[26] S. Mous et al. “Macromolecular crystallography and biology at the Linac Coherent Light Source”. In: *urn:issn:1600-5775* 32.3 (Apr. 2025), pp. 548–566. ISSN: 1600-5775. DOI: `https://doi.org/10.1107/S1600577525002735`.

[27] H. Liu and W. Lee. “The XFEL Protein Crystallography: Developments and Perspectives”. In: *International Journal of Molecular Sciences 2019, Vol. 20, Page 3421* 20.14 (July 2019), p. 3421. ISSN: 1422-0067. DOI: `https://doi.org/10.3390/IJMS20143421`.

[28] J. P. Couperus et al. “Demonstration of a beam loaded nanocoulomb-class laser wakefield accelerator”. In: *Nature Communications* 8 (Dec. 2017). ISSN: 20411723. DOI: `https://doi.org/10.1038/s41467-017-00592-7`.

[29] C. Aniculaesei et al. “The acceleration of a high-charge electron bunch to 10 GeV in a 10-cm nanoparticle-assisted wakefield accelerator”. In: *Matter and Radiation at Extremes* 9.1 (Jan. 2024). ISSN: 2468080X. DOI: `https://doi.org/10.1063/5.0161687`.

[30] A. Picksley et al. “Matched Guiding and Controlled Injection in Dark-Current-Free, 10-GeV-Class, Channel-Guided Laser-Plasma Accelerators”. In: *Physical Review Letters* 133.25 (Dec. 2024), p. 255001. ISSN: 0031-9007. DOI: `https://doi.org/10.1103/PhysRevLett.133.255001`.

[31] L. T. Ke et al. “Near-GeV Electron Beams at a Few Per-Mille Level from a Laser Wakefield Accelerator via Density-Tailored Plasma”. In: *Physical Review Letters* 126 (May 2021). ISSN: 10797114. DOI: `DOI:https://doi.org/10.1103/PhysRevLett.126.214801`.

[32] R. Weingartner et al. “Ultralow emittance electron beams from a laser-wakefield accelerator”. In: *Physical Review Special Topics - Accelerators and Beams* 15.11 (Nov. 2012), p. 111302. ISSN: 10984402. DOI: `https://doi.org/10.1103/PHYSREVSTAB.15.111302`.

[33] W. Wang et al. "Free-electron lasing at 27 nanometres based on a laser wakefield accelerator". In: *Nature 2021 595:7868* 595.7868 (July 2021), pp. 516–520. ISSN: 1476-4687. DOI: https://doi.org/10.1038/s41586-021-03678-x.

[34] M. Labat et al. "Seeded free-electron laser driven by a compact laser plasma accelerator". In: *Nature Photonics* 17.2 (Feb. 2023), pp. 150–156. ISSN: 17494893. DOI: https://doi.org/10.1038/S41566-022-01104-W.

[35] C. Pellegrini, A. Marinelli, and S. Reiche. "The physics of x-ray free-electron lasers". In: *Reviews of Modern Physics* 88.1 (Mar. 2016). ISSN: 15390756. DOI: https://doi.org/10.1103/RevModPhys.88.015006.

[36] L.-L. Yu et al. "Two-Color Laser-Ionization Injection". In: *Physical Review Letters* 112.12 (Mar. 2014), p. 125001. ISSN: 0031-9007. DOI: https://doi.org/10.1103/PhysRevLett.112.125001.

[37] X. L. Xu et al. "Low emittance electron beam generation from a laser wakefield accelerator using two laser pulses with different wavelengths". In: *Physical Review Special Topics - Accelerators and Beams* 17.6 (June 2014), p. 061301. ISSN: 10984402. DOI: https://doi.org/10.1103/PHYSREVSTAB.17.061301.

[38] C. B. Schroeder et al. "Thermal emittance from ionization-induced trapping in plasma accelerators". In: *Physical Review Special Topics - Accelerators and Beams* 17.10 (Oct. 2014), p. 101301. ISSN: 10984402. DOI: https://doi.org/10.1103/PHYSREVSTAB.17.101301.

[39] P. Sprangle, Cha Mei Tang, and E. Esarey. "Relativistic self-focusing of short-pulse radiation beams in plasmas". In: *IEEE Transactions on Plasma Science* 15.2 (1987), pp. 145–153. ISSN: 19399375. DOI: https://doi.org/10.1109/TPS.1987.4316677.

[40] G.-Z. Sun et al. "Self-focusing of short intense pulses in plasmas". In: *The Physics of Fluids* 30.2 (Feb. 1987), pp. 526–532. ISSN: 0031-9171. DOI: https://doi.org/10.1063/1.866349.

[41] P. Sprangle and E. Esarey. "Interaction of ultrahigh laser fields with beams and plasmas". In: *Physics of Fluids B: Plasma Physics* 4.7 (July 1992), pp. 2241–2248. ISSN: 0899-8221. DOI: 10.1063/1.860192.

[42] C. G. Durfee and H. M. Milchberg. "Light pipe for high intensity laser pulses". In: *Physical Review Letters* 71.15 (Oct. 1993), p. 2409. ISSN: 00319007. DOI: 10.1103/PhysRevLett.71.2409.

[43] E. Esarey et al. "Nonlinear Pump Depletion and Electron Dephasing in Laser Wakefield Accelerators". In: *AIP Conference Proceedings* 737.1 (Dec. 2004), pp. 578–584. ISSN: 0094-243X. DOI: https://doi.org/10.1063/1.1842594.

[44] T. Katsouleas. "Physical mechanisms in the plasma wake-field accelerator". In: *Physical Review A* 33.3 (Mar. 1986), p. 2056. ISSN: 10502947. DOI: https://doi.org/10.1103/PhysRevA.33.2056.

[45] A. Pukhov and I. Kostyukov. "Control of laser-wakefield acceleration by the plasma-density profile". In: *Physical Review E* 77.2 (Feb. 2008), p. 025401. ISSN: 15393755. DOI: `https://doi.org/10.1103/PhysRevE.77.025401`.

[46] W. Rittershofer et al. "Tapered plasma channels to phase-lock accelerating and focusing forces in laser-plasma accelerators". In: *Physics of Plasmas* 17.6 (June 2010), p. 37. ISSN: 1070-664X. DOI: `https://doi.org/10.1063/1.3430638`.

[47] R. Li et al. "Longitudinal tapering in gas jets for increased efficiency of 10-GeV class laser plasma accelerators". In: *Review of Scientific Instruments* 96.4 (Apr. 2025). ISSN: 0034-6748. DOI: `https://doi.org/10.1063/5.0250698`.

[48] A. Modena et al. "Electron acceleration from the breaking of relativistic plasma waves". In: *Nature* 377.6550 (Oct. 1995), pp. 606–608. ISSN: 00280836. DOI: `https://doi.org/10.1038/377606A0`.

[49] W. P. Leemans et al. "GeV electron beams from a centimetre-scale accelerator". In: *Nature Physics* 2.10 (Oct. 2006), pp. 696–699. ISSN: 17452481. DOI: `https://doi.org/10.1038/NPHYS418`.

[50] G. R. Plateau et al. "Low-emittance electron bunches from a laser-plasma accelerator measured using single-shot X-ray spectroscopy". In: *Physical Review Letters* 109.6 (Aug. 2012), p. 064802. ISSN: 10797114. DOI: `https://doi.org/10.1103/PHYSREVLETT.109.064802`.

[51] C. Benedetti et al. "Numerical investigation of electron self-injection in the nonlinear bubble regime". In: *Physics of Plasmas* 20.10 (Oct. 2013). ISSN: 1070664X. DOI: `https://doi.org/10.1063/1.4824811/318480`.

[52] S. Bulanov et al. "Particle injection into the wave acceleration phase due to nonlinear wake wave breaking". In: *Physical Review E* 58.5 (Nov. 1998), R5257–R5260. ISSN: 1063-651X. DOI: `https://doi.org/10.1103/PhysRevE.58.R5257`.

[53] H. Suk et al. "Plasma Electron Trapping and Acceleration in a Plasma Wake Field Using a Density Transition". In: *Physical Review Letters* 86.6 (Feb. 2001), p. 1011. ISSN: 00319007. DOI: `https://doi.org/10.1103/PhysRevLett.86.1011`.

[54] K. Schmid et al. "Density-transition based electron injector for laser driven wakefield accelerators". In: *Physical Review Special Topics - Accelerators and Beams* 13.9 (Sept. 2010), p. 091301. ISSN: 1098-4402. DOI: `https://doi.org/10.1103/PhysRevSTAB.13.091301`.

[55] J. Faure et al. "Injection and acceleration of quasimonoenergetic relativistic electron beams using density gradients at the edges of a plasma channel". In: *Physics of Plasmas* 17.8 (Aug. 2010), p. 083107. ISSN: 1070-664X. DOI: `https://doi.org/10.1063/1.3469581`.

[56] A. J. Gonsalves et al. "Tunable laser plasma accelerator based on longitudinal density tailoring". In: *Nature Physics* 7.11 (Nov. 2011), pp. 862–866. ISSN: 1745-2473. DOI: `https://doi.org/10.1038/nphys2071`.

[57] A. Buck et al. "Shock-Front Injector for High-Quality Laser-Plasma Acceleration". In: *Physical Review Letters* 110.18 (May 2013), p. 185006. ISSN: 0031-9007. DOI: `https://doi.org/10.1103/PhysRevLett.110.185006`.

[58] D. Umstadter, J. K. Kim, and E. Dodd. "Laser Injection of Ultrashort Electron Pulses into Wakefield Plasma Waves". In: *Physical Review Letters* 76.12 (Mar. 1996), p. 2073. ISSN: 10797114. DOI: `https://doi.org/10.1103/PhysRevLett.76.2073`.

[59] E. Esarey et al. "Electron Injection into Plasma Wakefields by Colliding Laser Pulses". In: *Physical Review Letters* 79.14 (Oct. 1997), p. 2682. ISSN: 10797114. DOI: `https://doi.org/10.1103/PhysRevLett.79.2682`.

[60] M. Chen et al. "Electron injection and emittance control by transverse colliding pulses in a laser-plasma accelerator". In: *Physical Review Special Topics - Accelerators and Beams* 17.5 (May 2014), p. 051303. ISSN: 10984402. DOI: `https://doi.org/10.1103/PHYSREVSTAB.17.051303`.

[61] J. Faure et al. "Controlled injection and acceleration of electrons in plasma wakefields by colliding laser pulses". In: *Nature* 444.7120 (Dec. 2006), pp. 737–739. ISSN: 14764687. DOI: `https://doi.org/10.1038/NATURE05393`.

[62] G. Fubiani et al. "Beat wave injection of electrons into plasma waves using two interfering laser pulses". In: *Physical Review E - Statistical Physics, Plasmas, Fluids, and Related Interdisciplinary Topics* 70.1 (July 2004), p. 12. ISSN: 1063651X. DOI: `https://doi.org/10.1103/PHYSREVE.70.016402`.

[63] C. Rechatin et al. "Controlling the phase-space volume of injected electrons in a laser-plasma accelerator". In: *Physical Review Letters* 102.16 (Apr. 2009), p. 164801. ISSN: 10797114. DOI: `https://doi.org/10.1103/PHYSREVLETT.102.164801`.

[64] M. Chen et al. "Electron injection and trapping in a laser wakefield by field ionization to high-charge states of gases". In: *Journal of Applied Physics* 99.5 (Mar. 2006). ISSN: 00218979. DOI: `https://doi.org/10.1063/1.2179194/566734`.

[65] A. Pak et al. "Injection and trapping of tunnel-ionized electrons into laser-produced wakes". In: *Physical Review Letters* 104.2 (Jan. 2010), p. 025003. ISSN: 00319007. DOI: `https://doi.org/10.1103/PHYSREVLETT.104.025003`.

[66] C. McGuffey et al. "Ionization induced trapping in a laser wakefield accelerator". In: *Physical Review Letters* 104.2 (Jan. 2010), p. 025004. ISSN: 00319007. DOI: `https://doi.org/10.1103/PHYSREVLETT.104.025004`.

[67] J. S. Liu et al. "All-optical cascaded laser wakefield accelerator using ionization-induced injection". In: *Physical Review Letters* 107.3 (July 2011), p. 035001. ISSN: 00319007. DOI: `https://doi.org/10.1103/PHYSREVLETT.107.035001`.

[68] C. E. Clayton et al. "Self-guided laser wakefield acceleration beyond 1 GeV using ionization-induced injection". In: *Physical Review Letters* 105.10 (Sept. 2010), p. 105003. ISSN: 00319007. DOI: `https://doi.org/10.1103/PHYSREVLETT.105.105003`.

[69] B. B. Pollock et al. "Demonstration of a narrow energy spread, 0.5GeV electron beam from a two-stage laser wakefield accelerator". In: *Physical Review Letters* 107.4 (July 2011), p. 045001. ISSN: 00319007. DOI: https://doi.org/10.1103/PHYSREVLETT.107.045001.

[70] B. Hidding et al. "Ultracold electron bunch generation via plasma photocathode emission and acceleration in a beam-driven plasma blowout". In: *Physical Review Letters* 108.3 (Jan. 2012), p. 035001. ISSN: 00319007. DOI: https://doi.org/10.1103/PHYSREVLETT.108.035001.

[71] M. Chen et al. "Theory of ionization-induced trapping in laser-plasma accelerators". In: *Physics of Plasmas* 19.3 (Mar. 2012). ISSN: 1070664X. DOI: https://doi.org/10.1063/1.3689922/919511.

[72] E. Esarey and M. Pilloff. "Trapping and acceleration in nonlinear plasma waves". In: *Physics of Plasmas* 2.5 (May 1995), pp. 1432–1436. ISSN: 1070-664X. DOI: https://doi.org/10.1063/1.871358.

[73] C. B. Schroeder et al. "Ultra-low emittance beam generation using two-color ionization injection in a CO2 laser-driven plasma accelerator". In: (May 2015).

[74] X. L. Xu et al. "Phase-space dynamics of ionization injection in plasma-based accelerators". In: *Physical Review Letters* 112.3 (Jan. 2014), p. 035003. ISSN: 00319007. DOI: https://doi.org/10.1103/PHYSREVLETT.112.035003.

[75] E. Oz et al. "Ionization-induced electron trapping in ultrarelativistic plasma wakes". In: *Physical Review Letters* 98.8 (Feb. 2007), p. 084801. ISSN: 00319007. DOI: https://doi.org/10.1103/PHYSREVLETT.98.084801.

[76] T. P. Rowlands-Rees et al. "Laser-driven acceleration of electrons in a partially ionized plasma channel". In: *Physical Review Letters* 100.10 (Mar. 2008), p. 105005. ISSN: 00319007. DOI: https://doi.org/10.1103/PHYSREVLETT.100.105005.

[77] M Chen et al. "Using transverse colliding-pulse injection to obtain electron beams with small emittance in a laser-plasma accelerator". In: *AIP Conference Proceedings* 1507.1 (Dec. 2012), pp. 262–266. ISSN: 0094-243X. DOI: https://doi.org/10.1063/1.4773704.

[78] S. Kalmykov et al. "Electron self-injection and trapping into an evolving plasma bubble". In: *Physical Review Letters* 103.13 (Sept. 2009), p. 135004. ISSN: 00319007. DOI: https://doi.org/10.1103/PHYSREVLETT.103.135004.

[79] M. Zeng et al. "Self-truncated ionization injection and consequent monoenergetic electron bunches in laser wakefield acceleration". In: *Physics of Plasmas* 21.3 (Mar. 2014). ISSN: 10897674. DOI: https://doi.org/10.1063/1.4868404/1032146.

[80] S. Li et al. "Enhanced single-stage laser-driven electron acceleration by self-controlled ionization injection". In: *Optics Express, Vol. 22, Issue 24, pp. 29578-29586* 22.24 (Dec. 2014), pp. 29578–29586. ISSN: 1094-4087. DOI: https://doi.org/10.1364/OE.22.029578.

[81] M. Tzoufras et al. "Beam loading in the nonlinear regime of plasma-based acceleration". In: *Physical Review Letters* 101.14 (Sept. 2008), p. 145002. ISSN: 00319007. DOI: https://doi.org/10.1103/PHYSREVLETT.101.145002.

[82] M. Mirzaie et al. "Demonstration of self-truncated ionization injection for GeV electron beams". In: *Scientific Reports* 5.1 (Oct. 2015), pp. 1–9. ISSN: 20452322. DOI: https://doi.org/10.1038/SREP14659.

[83] E. S. Dodd, J. K. Kim, and D. Umstadter. "Simulation of ultrashort electron pulse generation from optical injection into wake-field plasma waves". In: *Physical Review E - Statistical Physics, Plasmas, Fluids, and Related Interdisciplinary Topics* 70.5 (Nov. 2004), p. 13. ISSN: 1063651X. DOI: https://doi.org/10.1103/PHYSREVE.70.056410.

[84] N. Bourgeois, J. Cowley, and S. M. Hooker. "Two-pulse ionization injection into quasilinear laser wakefields". In: *Physical Review Letters* 111.15 (2013), pp. 1–5. ISSN: 00319007. DOI: https://doi.org/10.1103/PhysRevLett.111.155004.

[85] R. Hu et al. "Brilliant GeV electron beam with narrow energy spread generated by a laser plasma accelerator". In: *Physical Review Accelerators and Beams* 19.9 (Sept. 2016), p. 091301. ISSN: 24699888. DOI: https://doi.org/10.1103/PHYSREVACCELBEAMS.19.091301.

[86] M. W. Von Der Leyen et al. "Observation of Monoenergetic Electrons from Two-Pulse Ionization Injection in Quasilinear Laser Wakefields". In: *Physical Review Letters* 130.10 (Mar. 2023), p. 105002. ISSN: 10797114. DOI: https://doi.org/10.1103/PhysRevLett.130.105002.

[87] Y. Wan et al. "Colliding ionization injection in a plasma wakefield accelerator". In: *Plasma Physics and Controlled Fusion* 58.3 (Feb. 2016), p. 034015. ISSN: 0741-3335. DOI: https://doi.org/10.1088/0741-3335/58/3/034015.

[88] F. Li et al. "Generating high-brightness electron beams via ionization injection by transverse colliding lasers in a plasma-Wakefield accelerator". In: *Physical Review Letters* 111.1 (July 2013), p. 015003. ISSN: 00319007. DOI: https://doi.org/10.1103/PHYSREVLETT.111.015003.

[89] M. N. Rosenbluth and C. S. Liu. "Excitation of Plasma Waves by Two Laser Beams". In: *Physical Review Letters* 29.11 (Sept. 1972), p. 701. ISSN: 00319007. DOI: https://doi.org/10.1103/PhysRevLett.29.701.

[90] M. Zeng et al. "Multichromatic narrow-energy-spread electron bunches from laser-Wakefield acceleration with dual-color lasers". In: *Physical Review Letters* 114.8 (Feb. 2015), p. 084801. ISSN: 10797114. DOI: https://doi.org/10.1103/PHYSREVLETT.114.084801.

[91] C. B. Schroeder et al. “Two-color ionization injection using a plasma beatwave accelerator”. In: *Nuclear Instruments and Methods in Physics Research Section A: Accelerators, Spectrometers, Detectors and Associated Equipment* 909 (Nov. 2018), pp. 149–152. ISSN: 0168-9002. DOI: `https://doi.org/10.1016/J.NIMA.2018.01.008`.

[92] M. Zeng et al. “High quality electron beam acceleration by ionization injection in laser wakefields with mid-infrared dual-color lasers”. In: *Physics of Plasmas* 23.6 (June 2016). ISSN: 10897674. DOI: `https://doi.org/10.1063/1.4953895/320035`.

[93] Y. Xi et al. “Hybrid modeling of relativistic underdense plasma photocathode injectors”. In: *Physical Review Special Topics - Accelerators and Beams* 16.3 (Mar. 2013), p. 031303. ISSN: 10984402. DOI: `https://doi.org/10.1103/PHYSREVSTAB.16.031303`.

[94] B. Hidding. *First Measurements of Trojan Horse Injection in a Plasma Wakefield Accelerator (invited) - University of Strathclyde*. English. May 2017.

[95] B. Hidding et al. “Progress in Hybrid Plasma Wakefield Acceleration”. In: *Photonics 2023, Vol. 10, Page 99* 10.2 (Jan. 2023), p. 99. ISSN: 2304-6732. DOI: `https://doi.org/10.3390/PHOTONICS10020099`.

[96] Lu-Le Yu et al. “Low transverse emittance electron bunches from two-color laser-ionization injection”. In: *https://doi.org/10.1117/12.2021089* 8779 (May 2013), pp. 54–62. ISSN: 0277786X. DOI: `https://doi.org/10.1117/12.2021089`.

[97] P. Tomassini et al. “The resonant multi-pulse ionization injection”. In: *Physics of Plasmas* 24.10 (Oct. 2017). ISSN: 10897674. DOI: `https://doi.org/10.1063/1.5000696/798748`.

[98] P. Tomassini et al. “Accurate electron beam phase-space theory for ionization-injection schemes driven by laser pulses”. In: *High Power Laser Science and Engineering* 10 (Dec. 2022), e15. ISSN: 2095-4719. DOI: `https://doi.org/10.1017/HPL.2021.56`.

[99] S. Li et al. “A laser-plasma accelerator driven by two-color relativistic femtosecond laser pulses”. In: *Science Advances* 5.11 (Nov. 2019). ISSN: 23752548. DOI: `https://doi.org/10.1126/SCIADV.AAV7940`.

[100] J. Sharifzadeh Tabrizi et al. “Numerical study of electron acceleration driven by two-color laser pulses”. In: *AIP Advances* 13.4 (Apr. 2023). ISSN: 21583226. DOI: `https://doi.org/10.1063/5.0140834/2883450`.

[101] D. Umstadter, E. Esarey, and J. Kim. “Nonlinear Plasma Waves Resonantly Driven by Optimized Laser Pulse Trains”. In: *Physical Review Letters* 72.8 (Feb. 1994), p. 1224. ISSN: 00319007. DOI: `https://doi.org/10.1103/PhysRevLett.72.1224`.

[102] S. M. Hooker et al. “Multi-pulse laser wakefield acceleration: a new route to efficient, high-repetition-rate plasma accelerators and high flux radiation sources”. In: *Journal of Physics B: Atomic, Molecular and Optical Physics* 47.23 (Nov. 2014), p. 234003. ISSN: 0953-4075. DOI: `10.1088/0953-4075/47/23/234003`.

[103] J. Cowley et al. “Excitation and Control of Plasma Wakefields by Multiple Laser Pulses”. In: *Physical Review Letters* 119.4 (July 2017), p. 044802. ISSN: 10797114. DOI: `10.1103/PhysRevLett.119.044802`.

[104] R. J. Shalloo et al. “Generation of laser pulse trains for tests of multi-pulse laser wakefield acceleration”. In: *Nuclear Instruments and Methods in Physics Research Section A: Accelerators, Spectrometers, Detectors and Associated Equipment* 829 (Sept. 2016), pp. 383–385. ISSN: 0168-9002. DOI: `10.1016/J.NIMA.2016.02.044`.

[105] M. Z. Mo et al. “Quasimonoenergetic electron beams from laser wakefield acceleration in pure nitrogen”. In: *Applied Physics Letters* 100.7 (Feb. 2012). ISSN: 00036951. DOI: `https://doi.org/10.1063/1.3685464/24206`.

[106] E. Esarey, A. Ting, and P. Sprangle. “Frequency shifts induced in laser pulses by plasma waves”. In: *Physical Review A* 42.6 (Sept. 1990), p. 3526. ISSN: 10502947. DOI: `https://doi.org/10.1103/PhysRevA.42.3526`.

[107] *BLAST-WarpX/warpx: WarpX is an advanced Particle-In-Cell code.*

[108] Y. Ma et al. “Polarization-Dependent Self-Injection by Above Threshold Ionization Heating in a Laser Wakefield Accelerator”. In: *Physical Review Letters* 124.11 (Mar. 2020), p. 114801. ISSN: 10797114. DOI: `https://doi.org/10.1103/PHYSREVLETT.124.114801`.

[109] M. Rezaei-Pandari et al. “Laser Wakefield Electron Acceleration with Polarization-Dependent Ionization Injection”. In: *Physical Review Applied* 20.3 (Sept. 2023), p. 034026. ISSN: 23317019. DOI: `https://doi.org/10.1103/PHYSREVAPPLIED.20.034026`.

[110] A. Jain and D. N. Gupta. “Improvement of electron beam quality in laser wakefield acceleration by a circularly-polarized laser pulse”. In: *Plasma Physics and Controlled Fusion* 63.7 (May 2021), p. 075007. ISSN: 0741-3335. DOI: `https://doi.org/10.1088/1361-6587/abfd7d`.

[111] P. S. Banks, M. D. Feit, and M. D. Perry. “High-intensity third-harmonic generation in beta barium borate through second-order and third-order susceptibilities”. In: *Optics Letters, Vol. 24, Issue 1, pp. 4-6* 24.1 (Jan. 1999), pp. 4–6. ISSN: 1539-4794. DOI: `https://doi.org/10.1364/OL.24.000004`.

[112] Paul S. Banks, Michael D. Feit, and Michael D. Perry. “High-intensity third-harmonic generation”. In: *JOSA B, Vol. 19, Issue 1, pp. 102-118* 19.1 (Jan. 2002), pp. 102–118. ISSN: 1520-8540. DOI: `https://doi.org/10.1364/JOSAB.19.000102`.

[113] Aizitiaili Abulikemu, Aizitiaili Abulikemu, and Muneaki Hase. “Highly-efficient third-harmonic generation from ultrapure diamond crystals”. In: *Optical Materials Express, Vol. 13, Issue 4, pp. 916-924* 13.4 (Apr. 2023), pp. 916–924. ISSN: 2159-3930. DOI: `https://doi.org/10.1364/OME.485601`.

[114] Kentaro Miyata, Frank Noack, and Valentin Petrov. “High-efficiency single-crystal third-harmonic generation in BiB¡sub¿3¡/sub¿O¡sub¿6¡/sub¿”. In: *Optics Letters, Vol. 36, Issue 18, pp. 3627-3629* 36.18 (Sept. 2011), pp. 3627–3629. ISSN: 1539-4794. DOI: `https://doi.org/10.1364/OL.36.003627`.

[115] David Zuber et al. “Improved Performance of Frequency Tripling Mirrors: A Promising Approach for Simple and Efficient Third Harmonic Generation”. In: (2024). DOI: `https://doi.org/10.1051/epjconf/202430704076`.

[116] Paul J. Wegner et al. “NIF final optics system: frequency conversion and beam conditioning”. In: *https://doi.org/10.1117/12.538481* 5341 (May 2004), pp. 180–189. ISSN: 0277786X. DOI: `https://doi.org/10.1117/12.538481`.

[117] D. Eimerl et al. “Optical, mechanical, and thermal properties of barium borate”. In: *Journal of Applied Physics* 62.5 (Sept. 1987), pp. 1968–1983. ISSN: 0021-8979. DOI: `https://doi.org/10.1063/1.339536`.

[118] D. Eimerl. “Electro-Optic, Linear, and Nonlinear Optical Properties of Kdp and Its 1Somorphs”. In: *Ferroelectrics* 72 (1987), pp. 95–139. ISSN: 15635112. DOI: `https://doi.org/10.1080/00150198708017942`.

[119] Takashi Nakajima and Kenzo Miyazaki. “Spectrally compensated third harmonic generation using angular dispersers”. In: *Optics Communications* 163.4-6 (May 1999), pp. 217–222. ISSN: 0030-4018. DOI: `https://doi.org/10.1016/S0030-4018(99)00149-2`.

[120] Li Yang et al. “Optimization of 1.03μm femtosecond pulse laser tripling efficiency based on temporal walk-off compensation”. In: *Optics Communications* 537 (June 2023), p. 129413. ISSN: 0030-4018. DOI: `https://doi.org/10.1016/J.OPTCOM.2023.129413`.

[121] Heng Tu et al. “Growth of large aperture LBO crystal applied in high power OPCPA schemes”. In: *Journal of Crystal Growth* 546 (Sept. 2020), p. 125728. ISSN: 0022-0248. DOI: `https://doi.org/10.1016/J.JCRYSGRO.2020.125728`.

[122] Shoujun Wang et al. “0.85 PW laser operation at 3.3 Hz and high-contrast ultrahigh-intensity 400 nm second-harmonic beamline”. In: *Optics Letters, Vol. 42, Issue 19, pp. 3828-3831* 42.19 (Oct. 2017), pp. 3828–3831. ISSN: 1539-4794. DOI: `https://doi.org/10.1364/OL.42.003828`.

[123] Gorachand Ghosh. “Dispersion-equation coefficients for the refractive index and birefringence of calcite and quartz crystals”. In: *Optics Communications* 163.1-3 (May 1999), pp. 95–102. ISSN: 0030-4018. DOI: `https://doi.org/10.1016/S0030-4018(99)00091-7`.

[124] G. Imeshev et al. “Ultrashort-pulse second-harmonic generation with longitudinally nonuniform quasi-phase-matching gratings: pulse compression and shaping”. In: *JOSA B, Vol. 17, Issue 2, pp. 304-318* 17.2 (Feb. 2000), pp. 304–318. ISSN: 1520-8540. DOI: `https://doi.org/10.1364/JOSAB.17.000304`.

[125] T. Ditmire et al. "Effects of cubic nonlinearity on frequency doubling of high-power laser pulses". In: *JOSA B, Vol. 13, Issue 4, pp. 649-655* 13.4 (Apr. 1996), pp. 649–655. ISSN: 1520-8540. DOI: https://doi.org/10.1364/JOSAB.13.000649.

[126] J.J. Huang et al. "Proposal of high quality walk-off compensated sum frequency generation of ultra-short pulses". In: *Optics Communications* 281.20 (Oct. 2008), pp. 5244–5248. ISSN: 0030-4018. DOI: https://doi.org/10.1016/J.OPTCOM.2008.07.002.

[127] Robert A. Fisher and William K. Bischel. "Numerical studies of the interplay between self-phase modulation and dispersion for intense plane-wave laser pulses". In: *Journal of Applied Physics* 46.11 (Nov. 1975), pp. 4921–4934. ISSN: 0021-8979. DOI: https://doi.org/10.1063/1.321476.

[128] Kun Li and Bin Zhang. "Inverse problem of cascaded third-harmonic generation". In: *Optik* 119.1 (Jan. 2008), pp. 13–18. ISSN: 0030-4026. DOI: https://doi.org/10.1016/J.IJLEO.2006.05.023.

[129] C. Pieronek. "Laser Wakefield Acceleration of Multi-GeV Electron Bunches with Petawatt-Scale Laser Pulses Guided in a Laser-Heated Capillary Discharge". PhD thesis. University of California, Berkeley, 2021, pp. 1–194. ISBN: 2021PhDT33P.

[130] Kai Jia et al. "Study on broadband third harmonic conversion efficiency with angular spectral dispersion". In: *Optik* 124.12 (June 2013), pp. 1211–1214. ISSN: 0030-4026. DOI: https://doi.org/10.1016/J.IJLEO.2012.03.006.

[131] D M Pennington et al. *Efficient broadband third harmonic frequency conversion via angular dispersion.* July 1995. DOI: https://doi.org/10.1117/12.228272.

[132] D. J. Kane and R. Trebino. "Single-shot measurement of the intensity and phase of a femtosecond pulse". In: *Springer Series in Chemical Physics* 18.55 (1993), pp. 138–139. ISSN: 01726218. DOI: https://doi.org/10.1007/978-3-642-84910-7{_}36.

[133] Rick Trebino. "Frequency-Resolved Optical Gating: The Measurement of Ultrashort Laser Pulses". In: *Frequency-Resolved Optical Gating: The Measurement of Ultrashort Laser Pulses* (2000). DOI: https://doi.org/10.1007/978-1-4615-1181-6.

[134] W. L. Nighan et al. "Self-diffraction: A new method for characterization of ultrashort laser pulses". In: *Optics Communications* 69.3-4 (1989), pp. 339–344. ISSN: 00304018. DOI: https://doi.org/10.1016/0030-4018(89)90129-6.

[135] John N Sweetser, David N Fittinghoff, and Rick Trebino. "Transient-grating frequency-resolved optical gating". In: 22.8 (1997), pp. 519–521. DOI: https://doi.org/10.1364/OL.22.000519.

[136] C. G. R. Geddes et al. "Plasma-Density-Gradient Injection of Low Absolute-Momentum-Spread Electron Bunches". In: *Physical Review Letters* 100.21 (May 2008), p. 215004. ISSN: 0031-9007. DOI: https://doi.org/10.1103/PhysRevLett.100.215004.

[137] E. Guillaume et al. "Electron Rephasing in a Laser-Wakefield Accelerator". In: *Physical Review Letters* 115.15 (Oct. 2015), p. 155002. ISSN: 10797114. DOI: `https://doi.org/10.1103/PhysRevLett.115.155002`.

[138] C. Thaury et al. "Shock assisted ionization injection in laser-plasma accelerators". In: *Scientific Reports* 5.1 (Dec. 2015), p. 16310. ISSN: 2045-2322. DOI: `https://doi.org/10.1038/srep16310`.

[139] Hai-En Tsai et al. "Control of quasi-monoenergetic electron beams from laser-plasma accelerators with adjustable shock density profile". In: *Physics of Plasmas* 25.4 (Apr. 2018), p. 043107. ISSN: 1070-664X. DOI: `https://doi.org/10.1063/1.5023694`.

[140] A. H Epstein. "Fluorescent gaseous tracers for three dimensional flow visualization". In: *MIT Gas Turbine Lab Rep* (1974), p. 117.

[141] A. Lozano. *Laser-excited luminescent tracers for planar concentration measurements in gaseous jets*. Tech. rep. Stanford University, 1992, pp. 437–446.

[142] Christopher J Greenshields et al. "Implementation of semi-discrete, non-staggered central schemes in a colocated, polyhedral, finite volume framework, for high-speed viscous flows". In: *Int. J. Numer. Meth. Fl.* 63.1-21 (2010), pp. 1–21. DOI: `https://doi.org/10.1002/fld`.

[143] L. Fan-Chiang et al. "Gas density structure of supersonic flows impinged on by thin blades for laser-plasma accelerator targets". In: *Physics of Fluids* 32 (June 2020). ISSN: 10897666. DOI: `https://doi.org/10.1063/5.0005888`.

[144] H. M. Mott-Smith. "The Solution of the Boltzmann Equation for a Shock Wave". In: *Physical Review* 82.6 (June 1951), pp. 885–892. ISSN: 0031-899X. DOI: `10.1103/PhysRev.82.885`.

[145] Z. Bor. "Distortion of femtosecond laser pulses in lenses and lens systems". In: *Journal of Modern Optics* 35.12 (1988), pp. 1907–1918. ISSN: 13623044. DOI: `https://doi.org/10.1080/713822325`.

[146] C. Benedetti et al. "Efficient Modeling of Laser-Plasma Accelerators with INF&RNO". In: *AIP Conference Proceedings* 1299.1 (Nov. 2010), pp. 250–255. ISSN: 0094-243X. DOI: `10.1063/1.3520323`.

[147] Igor V. Pogorelsky et al. "Terawatt-class femtosecond long-wave infrared laser". In: *Frontiers in Physics* 12 (Apr. 2024), p. 1390225. ISSN: 2296424X. DOI: `https://doi.org/10.3389/FPHY.2024.1390225`.

[148] Gediminas Raciukaitis. "Ultra-Short Pulse Lasers for Microfabrication: A Review". In: *IEEE Journal of Selected Topics in Quantum Electronics* 27.6 (Nov. 2021). ISSN: 15584542. DOI: `10.1109/JSTQE.2021.3097009`.

[149] Kinga Filipek et al. "Ultrashort pulse lasers in medicine, current applications and prospects for future advances". In: *REVIEW — OPEN ACCESS Medical Science* 28 (2024), pp. 130–3422. DOI: `10.54905/disssi.v28i152.e130ms3422`.

[150] Ocean Zhou et al. "Effect of nozzle curvature on supersonic gas jets used in laser-plasma acceleration". In: *Physics of Plasmas* 28 (Sept. 2021). ISSN: 10897674. DOI: https://doi.org/10.1063/5.0058963.

[151] N. H. Matlis et al. "Snapshots of laser wakefields". In: *Nature Physics* 2.11 (Oct. 2006), pp. 749–753. ISSN: 17452481. DOI: https://doi.org/10.1038/NPHYS442;KWRD.

[152] P. Dong et al. "Holographic visualization of laser wakefields". In: *New Journal of Physics* 12.4 (Apr. 2010), p. 045016. ISSN: 1367-2630. DOI: https://doi.org/10.1088/1367-2630/12/4/045016.

[153] S. Becker et al. "Characterization and tuning of ultrahigh gradient permanent magnet quadrupoles". In: *Physical Review Special Topics - Accelerators and Beams* 12.10 (Oct. 2009), p. 102801. DOI: https://doi.org/10.1103/PhysRevSTAB.12.102801.

[154] S. K. Barber et al. "Measured Emittance Dependence on the Injection Method in Laser Plasma Accelerators". In: *Physical Review Letters* 119.10 (Sept. 2017), p. 104801. ISSN: 10797114. DOI: https://doi.org/10.1103/PhysRevLett.119.104801.

[155] Stephen W. Grib et al. "100kHz krypton planar laser-induced fluorescence imaging". In: *Optics Letters, Vol. 45, Issue 14, pp. 3832-3835* 45.14 (July 2020), pp. 3832–3835. ISSN: 1539-4794. DOI: https://doi.org/10.1364/OL.395389.

[156] Andreas R. Maier et al. "Decoding Sources of Energy Variability in a Laser-Plasma Accelerator". In: *Physical Review X* 10.3 (Aug. 2020), p. 031039. ISSN: 21603308. DOI: https://doi.org/10.1103/PhysRevX.10.031039.

[157] Matthias F. Kling et al. "Roadmap on basic research needs for laser technology". In: *Journal of Optics* 27.1 (Dec. 2024), p. 013002. ISSN: 2040-8986. DOI: 10.1088/2040-8986/AD8458.

[158] Coherent. *Astrella*. 2025.

[159] Vishwa Bandhu Pathak et al. "All optical dual stage laser wakefield acceleration driven by two-color laser pulses". In: *Scientific Reports* 8.1 (Dec. 2018), pp. 1–7. ISSN: 20452322. DOI: https://doi.org/10.1038/S41598-018-30095-4.

[160] M. C. Downer et al. "Diagnostics for plasma-based electron accelerators". In: *Reviews of Modern Physics* 90.3 (Aug. 2018), p. 035002. ISSN: 15390756. DOI: 10.1103/RevModPhys.90.035002.

[161] Ilya Agapov et al. *The Plasma Injector for PETRA IV: Enabling Plasma Accelerators for Next-generation Light Sources. Conceptual Design Report*. eng. Hamburg: Deutsches Elektronen-Synchrotron DESY, 2025, 66 pages. ISBN: 9783945931523.

[162] C. J. Zhang et al. "Femtosecond Probing of Plasma Wakefields and Observation of the Plasma Wake Reversal Using a Relativistic Electron Bunch". In: *Physical Review Letters* 119.6 (Aug. 2017), p. 064801. ISSN: 10797114. DOI: 10.1103/PhysRevLett.119.064801.

[163] Yang Wan et al. "Real-time visualization of the laser-plasma wakefield dynamics". In: *Science Advances* 10.5 (Feb. 2024), p. 3595. ISSN: 23752548. DOI: 10.1126/SCIADV.ADJ3595.